THE UNIVERSITY OF CHICAGO

DYNAMICS AND REGULATION OF MYOSIN CLUSTERS ON CONTRACTILE CYTOSKELETAL STRUCTURES

A DISSERTATION SUBMITTED TO
THE FACULTY OF THE DIVISION OF THE PHYSICAL SCIENCES
AND
THE FACULTY OF THE DIVISION OF THE BIOLOGICAL SCIENCES
AND THE PRITZKER SCHOOL OF MEDICINE
IN CANDIDACY FOR THE DEGREE OF
DOCTOR OF PHILOSOPHY

GRADUATE PROGRAM IN BIOPHYSICAL SCIENCES

BY
WEN-HUNG CHOU

CHICAGO, ILLINOIS
AUGUST 2023

To my family, mentors, and friends

TABLE OF CONTENTS

LIST OF FIGURES

ACKNOWLEDGMENTS

My Ph.D. journey wouldn't have been possible without the help and support from my mentors, family, and friends. First, I'd like to thank my mentors and colleagues throughout my scientific journey. In particular, my advisors Margaret and David were of tremendous help in guiding me through different stages of my Ph.D. research. Margaret in particular was instrumental in helping me shape the direction of my project. Additionally, my thesis committee members, Ed and Ron, offered invaluable feedback on my thesis work. I also want to thank my collaborators: Jordan, Patrick, and Melissa at Loyola University Chicago. They were very generous to provide crucial reagents for my project and their expertise were tremendously helpful.

I also want to thank my colleagues that I have worked with. When I first started my PhD research, I have the privilege to learn from many great senior colleagues in the lab, especially from Jon, Cristian, Yvonne, Bob. Without them I couldn't have made my experiments work. They also provided great insight into planning my project and interpreting experimental results. I'm also lucky to have Steven and Tracy as labmates who were in similar stages of my Ph.D. We had to overcome similar obstacles around the same time to get through our Ph.D. journey, which would have been much more difficult to go through by myself. Steven in particular also helped immensely in the modeling portion of my project, and it has been a pleasure bouncing various ideas off of each other. In addition, Mehdi and Shailaja provided much needed advice and feedback in the later stages of my Ph.D. I want to thank Mehdi in particular for his expertise in helping with my image analysis and Matlab scripts.

The Biophysical Sciences graduate program is also instrumental for my success during my Ph.D. Michele and Julie played phenomenal roles in taking care of the administrative hurdles so that I can focus on my research. Michele in particular is also very caring for the students not only for our graduate school experience but also for our general well being. Adam, who ran the BRI during my first year in graduate school, provided excellent knowledge and

insight into the different aspects of what my graduate school journey might entail. This helped me prepare for the long Ph.D. journey. Finally, I thank Greg and Tobin for running a great program that is supportive of their students.

Finally, my graduate school journey wouldn't have been possible without the support from my family. I'd like to thank my parents for the support, especially for being on board with my plans to be abroad for an extended amount of time. Last but not least, I want to thank my partner Pin-Yi for the support throughout the years. Without her I couldn't have survived grad school.

ABSTRACT

The actomyosin cytoskeleton generates mechanical forces that power a range of crucial cellular processes, such as cell migration, cell division, and mechanosensing. Actomyosin self-assembles into contractile bundles that underlie force generation in cells, such as stress fibers. The central element in the assembly of contractile bundles is the molecular motor non-muscle myosin II (NMII), which forms myosin filaments to slide actin filament bundles to generate contractile stress. While it is well-understood how myosin filament assembly is regulated, myosin filaments rarely exist as a single entity in cells. Instead, multiple myosin filaments self-assemble into clusters with their head domains in close contact with each other. While recent studies have characterized the dynamics of myosin clusters at the leading edge of the cell, how cells control the growth of myosin clusters on stress fibers has yet to be carefully characterized. In this thesis work, I studied the dynamics of myosin clusters to understand how they are regulated on stress fibers. First, we visualized and quantitatively analyzed the growth of myosin clusters on stress fibers. Myosin cluster growth is driven by both Rho-kinase (ROCK) activity and myosin motor activity, either through the net association of myosin monomers or filaments to existing clusters or through the coalescence of neighboring clusters. A toy model of myosin cluster growth with myosin self-affinity allows us to recapitulate experimentally-determined myosin cluster sizes. Critically, myosin cluster sizes are determined by the limiting pool of available myosin and the underlying F-actin architecture. Lastly, we extracted the material response functions of stress fibers to myosin-induced strain directly from myosin cluster dynamics, revealing different contractile modalities in different subcellular actomyosin networks. Collectively, our findings provide new insights into the cellular regulation of contractile actomyosin structures.

CHAPTER 1

INTRODUCTION

1.1 Mechanical forces in cell biology

In an era where biology is dominated by genetics, molecular biology, and protein biochemistry, mechanobiology has surfaced as an important field in biology. Not only does cell physiology depend on mechanical forces, but cells also sense and respond to mechanical forces. While much of cell biology in the 21st century focuses on understanding molecular pathways and protein functions, mechanobiology promises new avenues for understanding cell physiology, disease progression, and novel therapeutic modalities. Research in the past two decades has shown that mechanical forces play a myriad of roles in cell biology. Mechanical forces generated within the cell underlie dynamic processes in cells, such as cell migration, adhesion, and division. Cells also sense external mechanical cues and respond to mechanical perturbations to change their physiology. As mechanical forces are deeply embedded in cell biology, they can regulate multiple facets of cellular function in various systems, such as tissue development, stem cell differentiation, and immunology.

As a fundamental aspect of biology, cells are intrinsically dynamic: cells can change shape, crawl, and divide. This wouldn't be possible without mechanical forces. For example, cell migration requires the coordination of molecular motors at different parts of the cell to sustain a directional movement efficiently [1]. Moreover, cells need to adhere to the extracellular matrix via adhesion sites in order to move. These adhesions, termed focal adhesions, form and mature under mechanical forces [2, 3]. Another example is the cytokinesis process during cell division, where a parent cell divides into two daughter cells. In order to divide one cell into two, a contractile ring forms at the mid-plane of the parent cell to provide the forces required to constrict the cell membrane [4]. If mechanical forces are not properly regulated in any of these processes, cell physiology can be altered, which leads to a diseased state like

cancer metastasis [5, 6].

Aside from cell dynamics, cells sense and respond to their mechanical microenvironments, such as mechanical perturbations or physical properties of the extracellular matrix. Mechanical perturbations can arise internally, such as from the pushing and pulling forces from neighboring cells, or externally from substrate stretching or fluid flow. As an example, cells alter their morphology and physiology when they are stretched. Cells realign their shape and cytoskeletal structures within the cell based on the stretch direction, as a result changing cellular contractility and the cell division axis [7, 8]. Recent studies also indicate that there are genomic-level consequences. When cells are stretched, the nuclear heterochromatin changes its mechanical properties to protect the genomic content from mechanical damage [9]. On the other hand, cells can also sense and respond to the mechanical microenvironment, such as the stiffness of the extracellular matrix [10]. This is achieved by sensing forces transmitted to and from the extracellular matrix. Aside from changes in cell morphology and dynamics, it also changes the differentiation of stem cells. Stem cells differentiate into neural cells when cultured on soft substrates, while they differentiate into bone cells on stiff substrates [11]. The inability to sense or respond to mechanical forces can lead to various consequences, such as DNA damage or tumor progression.

Since mechanical forces affect many aspects of cell biology, they have to be tightly regulated both spatially and temporally for cells to function properly. This motivates my Ph.D. work to study mechanical forces generated by the cell. While there have been decades of research on the molecular force-generating machinery of the cell, there has yet to be a complete theory that fully predicts force generation in cells. In this introduction, I will discuss what is known so far about the molecular components that generate mechanical forces, and how this machinery builds structures that underlie force production. I will also discuss the different layers of regulation of these molecules and structures, highlighting less-understood pieces that provide the opportunity to gain more insight into building contractile subcellular

structures.

1.2 Molecular basis for mechanical forces in cells

1.2.1 The molecular force-generating machinery in cells

Through years of research, much has been known about the molecules involved in cellular force generation. The core of force production lies in two molecules: the cytoskeletal protein actin and the molecular motor myosin (fig. 1.1). Actin is a globular protein (G-actin) that polymerizes to form the actin cytoskeleton, which are semi-flexible actin filaments (F-actin) up to several micrometers in length. On the other hand, myosin is an actin-associated molecular motor that converts ATP to mechanical energy. When myosin binds to F-actin, ATP is hydrolyzed, and myosin motors can generate a power stroke. Molecular-level forces are generated by myosin motors sliding anti-parallel pairs of F-actin across each other. These molecular-level forces are transmitted to the cellular microenvironment. Integrins and the focal adhesion complex couple molecular forces to the extracellular matrix. The cadherin-catenin complex transmits forces from one cell to another (fig. 1.1). While all components of this machinery are essential for cellular forces, my thesis focuses on where forces originate: the molecular motor myosin.

1.2.2 Myosin II molecular motors

Myosin molecular motors are defined by their motor domains that interacts with F-actin and hydrolyzes ATP to produce motion. To date, phylogenic analysis categorizes all myosin motors into at least 15 classes [12]. While they all share a common motor domain that generates a power stroke on F-actin, each class of myosin all boast distinct domain structures, motor properties, and physiological functions. The class of myosin responsible for cellular force production belongs to the myosin II class, which are considered conventional myosins

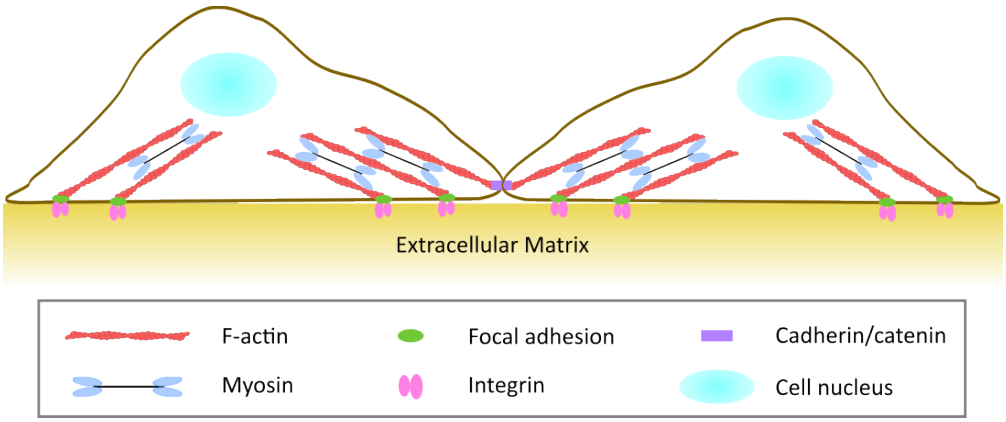

Figure 1.1: **Molecular machinery of cellular force production.** Mechanical forces at the molecular level are generated by the myosin molecular motor sliding F-actin filaments past each other. Molecular-level forces are transmitted to the extracellular matrix through the focal adhesion complex and integrin, or transmitted to neighboring cells through the cadherin-catenin complex.

because they are the most abundant in cells and have been extensively characterized [12]. All myosin II motors are hexamers, consisting of two heavy chains, two regulatory light chains (RLC) that regulate myosin activity, and two essential light chains (ELC) that stabilize myosin structure (fig. 1.2A) [13]. Myosin II heavy chains contain an N-terminal motor domain that interacts with F-actin to hydrolyze ATP and generate power stroke, and a C-terminal coiled-coil tail domain. For simplicity, we will refer to a single myosin motor as a myosin molecule or a myosin monomer.

In mammalian cells, there are three types of myosin II: skeletal muscle myosin II, smooth muscle myosin II, and non-muscle myosin II. Skeletal muscle myosin II is expressed in skeletal muscles and is responsible for the contraction of skeletal muscles. Smooth muscle myosin II is predominantly expressed in smooth muscle cells and is responsible for the contraction of smooth muscles. Non-muscle myosin II (NMII), on the other hand, is expressed in most cell types. Not only do they facilitate cell dynamics and mechanosensing in non-muscle cells, they also play a role in other muscles, such as aiding with sarcomere formation [14] or aid with smooth muscle contraction [15]. Despite its broad range of roles, NMIIs remain not as well-studied as muscle myosins. Therefore, my thesis work focuses on NMII since I mainly

focus on non-muscle cells and also because of its broad applicability to most cell types.

While non-muscle myosins are often discussed as a whole, NMIIs have three isoforms, IIA, IIB, and IIC, each with slightly different motor properties and plays different roles in cells. NMIIA is shown to walk faster on F-actin [16] but with a smaller duty ratio [17], therefore credited to be the main force generator in cells [18]. NMIIB has a higher duty ratio [17], but walks slower on F-actin [16]. NMIIB is therefore implicated in crosslinking F-actin structures and sustaining forces [18]. NMIIC is much less characterized, as the loss of NMIIC in cells doesn't give rise to any apparent phenotype. A recent study has suggested that it plays a role in maintaining mechanical homeostasis, or the ability to return to a mechanical set point once perturbed [18].

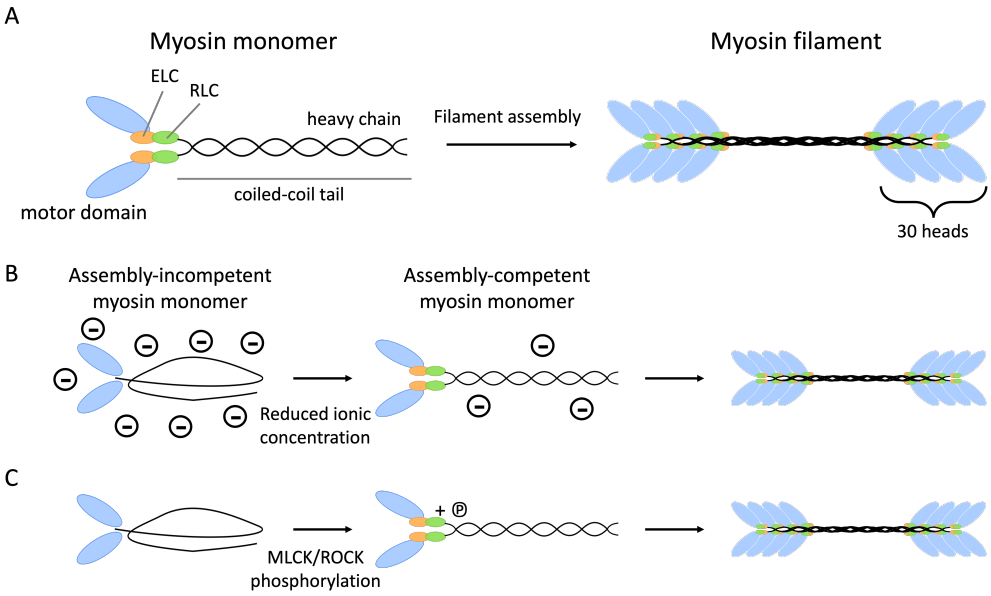

Figure 1.2: **Molecular regulation of non-muscle myosin II motors.** (A) Domain structure of non-muscle myosin II (NMII) monomer. 30 NMII monomers self-assemble into a bipolar filament with the motor domains on both ends of the filament. (B) Ionic regulation of NMII filament assembly. (C) RLC phosphorylation regulates NMII filament assembly.

1.2.3 Non-muscle myosin II self-assembles into filaments

Individual NMII motors cannot produce mechanical forces efficiently due to their low duty ratios. Even for NMIIB, which has the highest duty ratio (0.2) among all NMIIs, only binds to F-actin for a short fraction of its duty cycle. As a result, individual NMII motors are unable to processively generate forces. As a result, 30 NMII molecules self-assemble into a tightly packed filamentous structure with their N-terminal heads on both ends of the filament and C-terminal tails in the center (fig. 1.2A) [19]. With the NMII filament as a single structural unit, this ensures that at least one NMII motor is engaged with F-actin at all times [20]. By packing multiple motor heads into one unit, this also allows for higher force production. Skeletal muscle myosins and smooth muscle myosins also assembles into filaments that differs in size and filament morphology.

NMII assembles into filaments through the C-terminal tails of the NMII heavy chain. Studies have shown that there are a few critical domains at the end of the C-terminal tail that are essential for filament assembly[21]. Further research have identified that these critical domains allow for electrostatic interactions between pairs of NMII tails [22, 23], allowing them to tightly pack into a three-dimensional filamentous structure [24].

1.2.4 Molecular regulation of NMII filament assembly

Since NMII forms filaments via electrostatic interactions of the C-terminal coiled-coil tail, this interaction is perturbed when NMII enters an auto-inhibited state, where NMII folds such that the head domain is in contact with the tail domain, thereby inhibiting filament assembly [13]. The transition between the assembly-competent state and the assembly-incompetent state is largely dependent on ionic concentration of the surrounding buffer and RLC phosphorylation. At high ionic concentration, the electrostatic interaction will be screened so NMII filament assembly is inhibited (fig. 1.1B). RLC phosphorylation also changes NMII conformation into the assembly-competent state (fig. 1.1C). Several kinases,

such as the myosin light chain kinase (MLCK) or the Rho-associated kinase (ROCK), can phosphorylate the Ser19 or Thr18 residues of the RLC to facilitate this change [13, 25]. Similarly, when the RLC is dephosphorylated by phosphatases like the myosin phosphatase, NMII filaments can be disassembled. Phosphorylation on the myosin heavy chain has also been shown to disassemble NMII filaments [26]. Non-biochemical regulation of NMII assembly and disassembly have also been proposed, such as mechanical tension [24, 27]. While different NMII isoforms have been shown to co-polymerize into the same filament [28], we don't expect the regulation to be different.

1.3 Higher-order actomyosin structures underlie cellular forces

Understanding the molecular regulation of NMII has given us great insight into how cellular force generation is regulated. Unfortunately, summing up all the molecular motors present in the cell is not sufficient to predict cellular force production. One study observed only a loose correlation between the total amount of assembled NMII in cells and the mechanical forces produced by a cell [29]. The main reason is that forces are not solely generated by individual molecular pairs. Instead, molecular forces are generated by self-assembled actomyosin structures. Recent studies pointed out that the self-organization of actomyosin arrays can give rise to another layer of regulation of contractility [30, 31].

1.3.1 Contractile actomyosin structures in muscle cells

The most notable example of this self-organization is the myofibril within muscle cells. Myofibrils are long fibrous structures that span across muscle cells and are responsible for muscle contraction. Myofibrils comprise repeated subunits called sarcomeres, which serve as the minimal contractile unit of muscle cells (fig. 1.3A). Sarcomeres consist of a regular array of thin actin filament bundles and thick myosin filaments. Thin actin filament bundles consist of actin filaments crosslinked by crosslinkers, such as α-actinin. α-actinin crosslinks

and anchors the barbed ends of the F-actin bundles at the regularly-spaced Z-disc, which defines the ends of a sarcomere. Thick myosin filaments, which consist of multiple skeletal myosin II filaments, localize in between the Z-discs and interact with the pointed ends of the F-actin bundle. To initiate muscle contraction, thick myosin filaments hydrolyze ATP to slide anti-parallel F-actin bundles past each other to shorten the sarcomere. Multiple other actin-binding proteins associate with the sarcomere, such as tropomyosin, troponin, and titin, to either assist with the mechanical stability of the sarcomere or initiate the signaling pathway for sarcomere contraction. The intricate organization of the sarcomere has to be maintained properly, as defects in the basic structure of the sarcomere lead to muscle dysfunction [32, 33, 34].

1.3.2 Contractile actomyosin structures in non-muscle cells

In non-muscle cells, mechanical forces are generated similarly by a network of fibrous actomyosin structures called stress fibers. As opposed to the linear myofibrils that are well-aligned with each other, stress fibers form a complex interwoven network across the whole cell (fig. 1.3B). Stress fibers are not only responsible for cellular force generation that underlies cell dynamics but also supports cell shape and mechanosensing [35, 36]. Stress fibers have been characterized based on their morphology and their relation with focal adhesions [35, 37]. Dorsal stress fibers form with only one end attached to adhesions and grow radially inward from the cell edge. Transverse arcs are arch-like fibers that are not attached to adhesions and run parallel to the cell edge in the lamellar region. Ventral stress fibers are attached to adhesions at both ends and form more frequently at the trailing edge and cell center. Since myosin is largely absent on dorsal stress fibers, transverse arcs and ventral stress fibers are thought to be the main force producers.

The force production from stress fibers can be similarly attributed to a repeating subunit that is very similar to a sarcomere. This subunit also consists of actin filament bundles

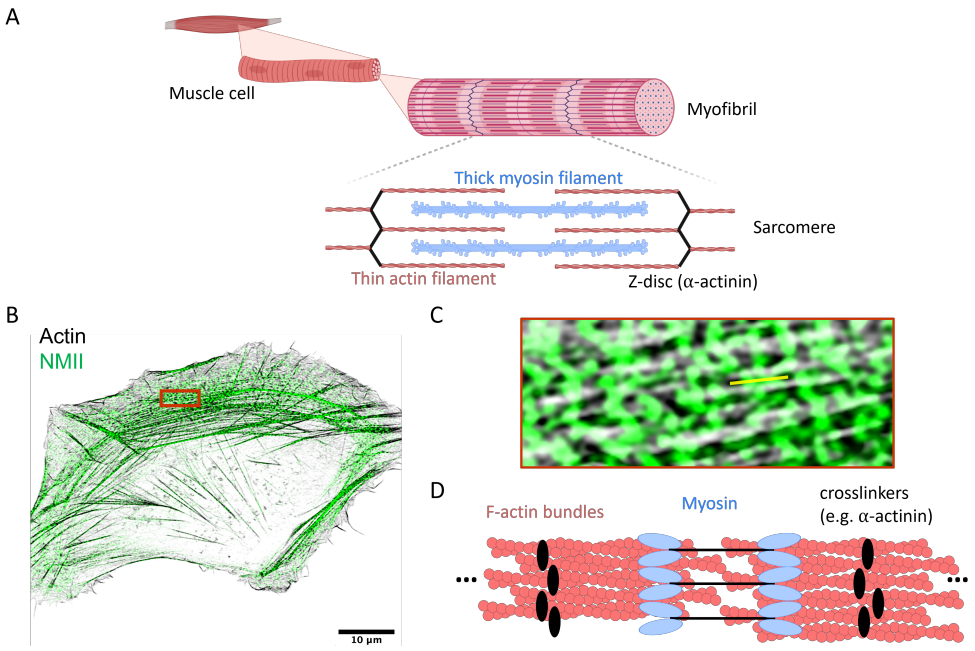

Figure 1.3: **Contractile actomyosin structures in cells.** (A) Schematics of myofibril and sarcomere structure. Sarcomeres consist of thin F-actin filament bundles crosslinked by α-actinin at the Z-disc, and thick myosin filaments. Created with BioRender.com. (B) Representative image of the stress fiber network in non-muscle cells. NMIIA is endogenously labelled in U2OS cells and F-actin is stained with fluorescent phalloidin. F-actin is inverted and colored in black. NMII is colored in green. Scale bar 10 µm. (C) Zoom-in view of the stress fiber network in the red box in (B). (D) Minimal mechanical subunit of stress fibers. The minimal mechanical subunit of stress fibers consists of F-actin filament bundles crosslinked by α-actinin and NMII clusters.

that are crosslinked by α-actinin at the barbed ends. NMII filament clusters localize in between the α-actinin bands and interact with the pointed ends of the F-actin bundle to slide F-actin bundles past each other (fig. 1.3C, D) [38]. In contrast with sarcomeres, the organization of the stress fiber subunits is much less ordered. While the overall patterns and spacing of protein localization seem to exhibit a similar order as sarcomeres, the spacing and respective localization of proteins fluctuate around an established baseline of order. This semi-ordered actomyosin organization suggests that stress fibers generate mechanical forces with a different modality from myofibrils, which has been the focus of several research (for example reviewed in [30]). Recently, the quasi-sarcomeric ordering of stress fibers has been

proposed to allow for efficient force production [39].

Stress fiber assembly and regulation depends on both F-actin and NMII. When F-actin bundles is perturbed, for example by knocking down the formin mDia1 or the crosslinker α-actinin, both stress fiber morphology and cellular contractility is impacted [2]. This has been the subject of extensive investigation. On the other hand, stress fiber assembly also depends on NMII function. Stress fibers and cellular contractility are severely disrupted when myosin motor activity or RLC phosphorylation is inhibited [40, 41, 42]. This points to the fact that NMII regulation is critical for stress fiber formation and cellular force production.

1.4 NMII filaments form clusters in cells

While the molecular regulation of NMII has been well-documented (see section 1.2), one factor that is often overlooked is that NMII filaments rarely appear as single entities in cells. Instead, they are often observed to form clusters in cells. This is best evidenced by platinum-replica electron microscopy, which allows for the ultra-structural imaging of the cytoskeleton in cells [43]. Single NMII filaments are rarely observed, and mostly appear close to the edge of the cell. Most NMII filaments form clusters with the head domains in close contact with each other. These clusters have been identified in multiple cell types [44, 45], so it is likely conserved across cells. At the leading edge of the cell, the clusters are smaller and contain a few easily identifiable NMII filaments. As actomyosin structures become more dense in the lamella of the cell, myosin clusters become bigger and contain multiple myosin filaments and clusters can overlap. On stress fibers, multiple myosin clusters align with each other spanning multiple stress fibers to form super-structures called stacks. The physiological function NMII clusters and stacks are still unclear, but some studies implied that they can play a role in moderating stress fiber architecture or regulating cellular contractility [38].

While NMII filament assembly has been studied extensively, the assembly and regulation of myosin clusters remain poorly-understood. While electron microscopy allows for the

ultrastructural imaging that allows the discovery of clusters, the static images produced by electron microscopy misses out on the dynamics of myosin clusters, making the inference about their assembly pathway difficult. With the advances in molecular biology and fluorescence microscopy, recent studies are able to capture the dynamics of myosin clusters in cells. Using super-resolution microscopy, Fenix et al. and Beach et al. observed the nucleation of NMII filaments at the leading edge of the cell. After nucleation, NMII filaments expand and amplify in size, with more NMII filaments recruited to the nucleated filament to form clusters. The amplified NMII cluster can either split into two clusters to increase the number of clusters available to accumulate NMII, or concatenate with another NMII cluster. With rounds of amplification, splitting, and concatenation, NMII clusters incorporate into the stress fiber network. The assembly and growth of myosin clusters in cells have been shown to depend on myosin monomer availability, myosin motor activity, and actin dynamics [46, 47]. These regulatory factors are in line with studies that identified factors that perturb the formation of myosin stacks [38]. Therefore, we argue that the growth of myosin clusters and their regulation is not limited to the leading edge but a general mechanism across the cell. However, to the best of our knowledge, a careful characterization of myosin clusters on stress fibers is lacking. Moreover, it is not clear what extra information one could extract from characterizing myosin clusters.

1.5 Scope of this work

As such, my research during my Ph.D. aims to characterize myosin clusters, understand the regulation of myosin clusters, and extract information from myosin clusters on stress fibers in non-muscle cells. This is enabled by the pioneering work studying myosin dynamics in cells using advanced microscopy and molecular biology tools. The main body of my Ph.D. work is documented in Chapter 2, where I quantitatively characterize the size of NMII clusters and find that their sizes are set by a limiting pool of myosin. Chapter 4 describes preliminary

research on how myosin dynamics can be controlled by more unconventional factors, such as mechanical forces and F-actin. In Chapter 3, I present collaborative work to extract material properties of the stress fibers from myosin cluster dynamics.

CHAPTER 2

MYOSIN CLUSTER SIZES ARE SET BY A LIMITING POOL OF AVAILABLE MYOSIN

2.0 Preamble

This section documents the primary thesis project. In this work, we aim to understand the growth and regulation of myosin clusters on stress fibers. This manuscript, titled *Limiting Pool and Actin Architecture Controls Myosin Cluster Sizes in Adherent Cells*, is submitted to *Biophysical Journal* and available on bioRxiv [48]. Wen-hung Chou, Medhi Molaei, Patrick Oakes, Jordan Beach and Margaret Gardel designed research; Wen-hung Chou and Medhi Molaei performed research and analyzed data; Wen-hung Chou, Medhi Molaei and Huini Wu provided reagents; Wen-hung Chou, Medhi Molaei, Patrick Oakes, Jordan Beach and Margaret Gardel interpreted results and wrote the paper.

2.1 Introduction

Various cellular processes and dynamics in cells depend on mechanical forces generated by the actomyosin cytoskeleton, such as cell motility [13], adhesion [2, 3], and mechanosensing [49]. The central contractile molecular element of the actomyosin cytoskeleton is non-muscle myosin II (NMII, hereafter referred to as myosin), which self-assembles into myosin filaments that contract actin filaments (F-actin) to generate contractile forces. In combination with crosslinkers and other actin binding proteins, actin and myosin build contractile actomyosin structures that underlie force production in cells. For example, in non-muscle cells, F-actin bundles and myosin filaments form contractile bundles that span the cell, called stress fibers. While both F-actin and myosin must be regulated to build stress fibers, F-actin regulation has been well-studied (for example, reviewed in [50, 51]) and myosin regulation is relatively

less understood.

Most studies on myosin regulation have focused on the assembly of myosin filaments from myosin molecules. At the molecular scale, the ability of myosin to assemble into myosin filaments is determined by the transition between its assembly-incompetent autoinhibited state and its assembly-competent active state [52]. This transition largely depends on phosphorylation on the regulatory light chain (RLC) of myosin. Several kinases, including the myosin light chain kinase (MLCK) and Rho-associated coiled-coil containing kinase (ROCK), can phosphorylate the Thr18 or Ser19 residues of the RLC to promote myosin filament assembly [13, 25, 53]. Phosphorylation sites on the myosin heavy chain has also been shown to play a role [13, 26]. Aside from biochemical regulation, mechanical tension has also been proposed to impact the assembly of myosin filaments [24, 27, 54].

Despite the importance of myosin filament regulation, single myosin filaments are rarely observed in cells. While some individual myosin filaments may be observed near the cell periphery at the leading edge, most myosin filaments in cells form clusters, where multiple myosin filaments come into close contact with each other with their myosin head domains. Described as ribbons or stacks, myosin clusters were best visualized using electron microscopy [44, 45, 54, 55]. Myosin clusters at the leading edge of the cell usually contain fewer myosin filaments, while more myosin filaments cluster together towards the cell body as they associate with stress fibers. Myosin clusters can further register with each other to form super-structures on stress fibers [38]. However, it remains largely unknown how myosin filaments self-associate to form clusters and how the process is regulated.

Recent studies have characterized the dynamics of myosin clusters to understand their formation at the leading cell edge. Using super-resolution microscopy, myosin filaments were observed nucleating at the leading edge of the cell [46, 47]. After nucleation, more myosin filaments were recruited to the nucleated filament to form myosin clusters. Through rounds of amplification and splitting, myosin clusters amplify both in size and number before

incorporating into stress fibers. The amplification and splitting dynamics have been shown to depend on myosin monomer availability, myosin motor activity, actin dynamics, and actin density [46, 47]. While myosin cluster dynamics at the leading edge and their regulation is thought to be general for all myosin clusters in cells, myosin cluster sizes on stress fibers have not been properly characterized.

In this work, we explore the regulation of myosin cluster sizes distribution in the lamella of adherent cells. To this end, we quantitatively characterized endogenously tagged non-muscle myosin IIA (NMIIA) in adherent U2OS osteosarcoma cells. The size distribution of myosin clusters found within actin networks and bundles within the lamella is quite broad. ROCK activity is sufficient to grow myosin clusters without myosin motor activity by increasing the pool of assembled myosin that can associate with existing ROCK-independent myosin clusters. Myosin motor activity further enhances myosin cluster growth by myosin association that is dependent on F-actin architecture. A toy model of myosin cluster growth with myosin self-affinity is sufficient to recapitulate the broad distribution of cluster sizes. Our results suggest that myosin cluster sizes within the lamella of adherent cells are set by a limiting pool of myosin available for cluster growth.

2.2 Myosin filaments form clusters of a broad range of sizes within lamellar actin networks and bundles

To study the regulation of myosin clusters, we chose the human osteosarcoma U2OS cell line because their lamellar actin architectures, including stress fibers, have been well-characterized [35, 37]. Using a CRISPR knock-in approach, we endogenously labeled non-muscle myosin IIA by inserting an mScarlet gene at the C-terminal locus of MYH9 (see methods). We chose to focus on non-muscle myosin IIA because of its role in generating contractile forces in cells [18, 56], and it is the dominant myosin isoform in U2OS cells. Since myosin assembles into a filament with their C-terminal tail overlapping at the bare zone, the fluorescence signal

represents the central location of a myosin filament (fig. 2.1A). Using spinning disk confocal imaging, we see that most myosin appears as diffraction-limited puncta of similar physical dimensions but with varying intensities (fig. 2.1B). These myosin puncta often colocalize with F-actin bundles (fig. 2.1B). Since our imaging conditions are likely insufficient to confidently detect single myosin filaments, each punctum likely contains multiple myosin filaments. We therefore refer to these punctate structures as myosin clusters, which may represent single or multiple closely associated myosin stacks.

To characterize myosin cluster dynamics, we conducted time-lapse live-cell imaging. While myosin clusters undergo retrograde motion and contract inward towards the cell center, they remain stable over time, persisting for at least 8 minutes (Supp. Fig. 1A & Supp. Movie 1). This suggests that myosin clusters are not multiple randomly overlapping structures but rather stable structures that move together as one unit. Despite their structural stability, the constituents of myosin clusters exchange rapidly. When we perform fluorescence recovery after photobleaching (FRAP) analysis on myosin clusters, we see that myosin fluorescence recovers with a half-time of $\sim$2 minutes and a mobile fraction of 80% (Supp. Fig. 1B, D, E), consistent with previous reports [37, 56, 57, 58]. We also observed FRAP recovery at the level of individual myosin clusters. Instead of assembling new myosin clusters or transporting clusters into the photobleached region, nearby myosin clusters undergo FRAP recovery at a similar rate (Supp. Fig. 1C). This suggests that myosin is continually exchanging within myosin clusters, with constant association and dissociation of myosin. Since myosin clusters contain multiple myosin filaments (see characterization below), FRAP recovery may indicate the exchange of single myosin monomers, oligomers, or whole filaments.

Since myosin is endogenously labeled, myosin punctum intensity reflects the number of myosin filaments within each cluster. To quantify the intensities of myosin clusters bound to the lamellar actin network or bundles, we fixed and permeabilized the cells before imaging to remove unbound or weakly-bound myosin. We noticed diffuse myosin intensity within the cell

that is higher than background intensities even after fixation and permeabilization (Supp. Fig. 2); this may indicate myosin bound to the cellular cortex. To focus on quantifying the intensities of myosin puncta, we exclude the diffuse background by performing local background subtraction. Then, the centroid location of each myosin punctum are determined using previously developed methods [59]. Briefly, each image is passed through a bandpass filter to preserve circular features with a diameter of ∼700 nm, about the typical size of a myosin punctum. Local maxima with intensity higher than background noise are accepted as a puncta candidate (fig. 2.1C). We further filter out puncta that are irregularly shaped or puncta whose intensity are too spread out (see methods). The remaining puncta candidates are accepted as valid myosin clusters. Each myosin cluster's intensity is then calculated as the integrated intensity of each punctum within a diameter of ∼700 nm.

While the absolute number of myosin molecules within each cluster requires careful calibration between fluorescence intensity and the number of fluorescent proteins [60], their relative sizes can be assessed without this calibration. To compare the sizes of myosin clusters across different cells and experimental conditions, we normalize all myosin cluster intensities within the same set of experiment against the minimum myosin intensity identified in each experiment. We posit that this minimum intensity (I_{min}) reflects the minimal number of myosin molecules in a cluster (N_{min}) we can detect above the noise floor. N_{min} likely represents more than one myosin filament (see [60], which suggests that the vast majority of identifiable myosin structures at the leading edge of the cell contains more than one myosin filaments). Since we keep the imaging conditions and analysis parameters constant in each experiment, we reasoned that N_{min} will be the same but I_{min} can vary slightly across different experiments. Therefore, we normalize myosin cluster intensities in each experiment to I_{min} and present myosin cluster sizes as multiples of N_{min}.

With this approach, we find a broad distribution of myosin cluster sizes across the cell, ranging up to 30-fold. Most myosin clusters contain 3 times more myosin than N_{min}, but

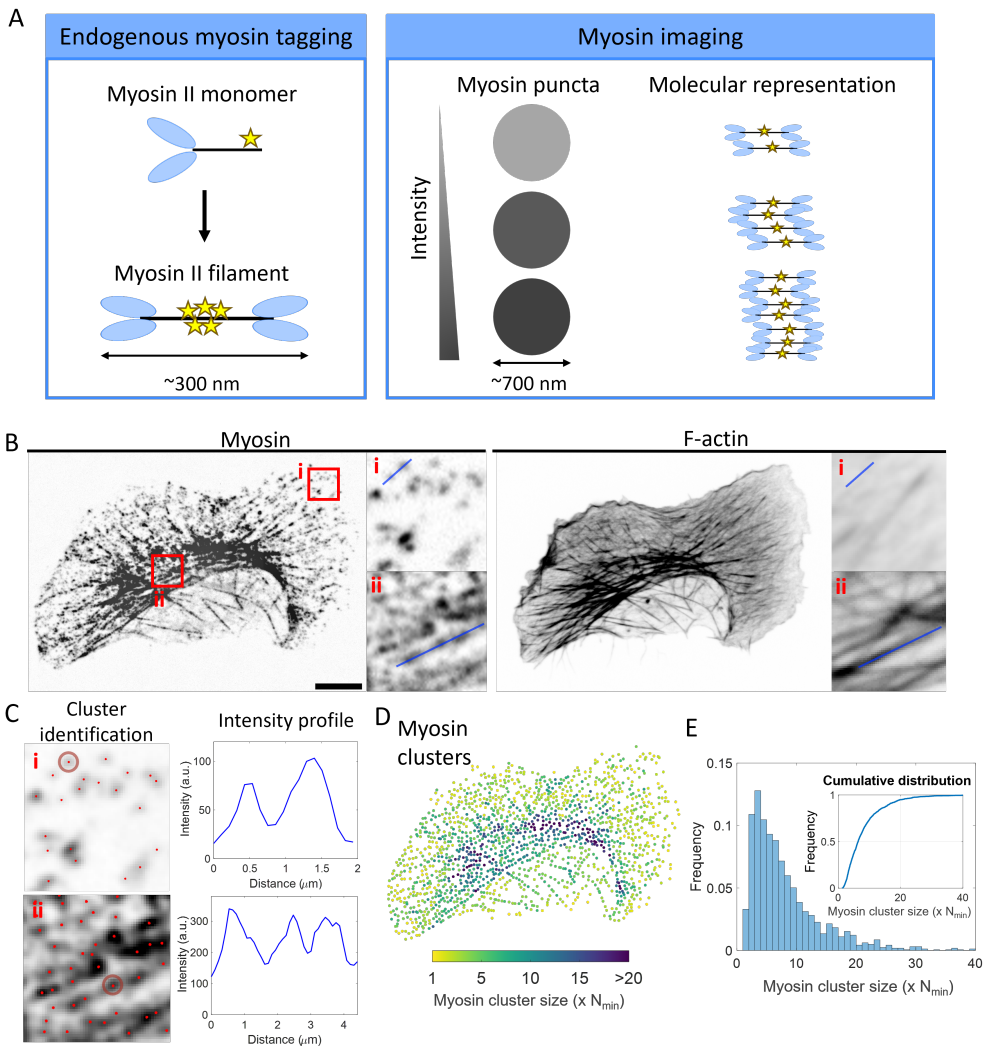

Figure 2.1: **Myosin filaments form clusters of a broad range of sizes on stress fibers.** (A) Schematics of the experiment setup. Non-muscle myosin IIA is endogenously tagged on the C-terminal tail so that myosin filaments will appear as diffraction-limited puncta. The intensity of each punctum is directly proportional with the amount of myosin filaments in each cluster. The number of myosin heads on a filament have been reduced for simplicity. (B) Representative images of non-muscle myosin IIA (myosin) and F-actin in a U2OS cell. The right panels show zoom-in of myosin clusters from the two red boxes. Images are inverted. Scale bar 10 μm. (C) Examples of myosin cluster localization. In the cluster identification column, each myosin intensity maxima is shown as a red dot. The brown circles indicate a typical area where the integrated intensity of a myosin punctum is calculated. The intensity profile column shows the intensity profile along the blue line in (B)i and (B)ii. (D) Myosin clusters in cells color-coded by their sizes. N_{min} represents the minimal myosin cluster size that can be detected, as discussed in the text. (E) Histogram of myosin cluster sizes. Inset shows the cumulative distribution of myosin cluster sizes.

there is a sizeable fraction of larger myosin clusters containing 20-fold more myosin than N_{min} (fig. 2.1D, E). This is also evidenced by the histogram of myosin cluster intensities, which shows a long-tailed distribution (fig. 2.1E). Myosin intensity is also spatially heterogeneous (fig. 2.1D). Myosin clusters tend to be smaller at the lamellar region or newly formed transverse arcs, containing only 2-4 times more myosin than N_{min} (fig. 2.1C, i). On the other hand, myosin clusters tend to be larger on mature transverse arcs in the cell body or on ventral stress fibers, with more than 15 times more myosin than N_{min} (fig. 2.1C, ii).

2.3 Rho-kinase activity drives growth through net myosin association to existing clusters

Recent literature showed that myosin clusters at the leading edge is regulated by myosin monomer availability and motor activity [46, 47]. We designed an experiment to test their respective contributions to the growth of myosin clusters within the lamellar actin. To promote myosin cluster disassembly, cells were treated with 40 µM ROCK inhibitor Y-27632 (Y-27, inhibits ROCK-dependent myosin light chain phosphorylation) and 50 µM blebbistatin (myosin II motor inhibitor and locks myosin in a weak actin-binding state [61]) for 30 minutes. Even after treatment, residual myosin clusters with low fluorescence intensity remained (fig. 2.2A, Y+B+). Compared with the cluster size distribution of control cells, the peak was shifted towards smaller cluster sizes, and the upper tail of the distribution was reduced (fig. 2.2B). This indicates that the sizes of the remaining myosin clusters are smaller with less variation, averaging around 2-3 times the size of N_{min} (fig. 2.2B, Y+B+). These myosin clusters are presumably formed by myosin filaments that are phosphorylated by other kinases, such as MLCK, MRCK, or CDC42, or formed by increasing the total monomer pool above a critical threshold to enable spontaneous filament assembly [60].

To decouple the role of ROCK and myosin motor activity on myosin cluster growth, we selectively retain one inhibitor during washout of the other. When we selectively washed

out blebbistatin but retained Y-27, we see no apparent increase in myosin cluster intensity (fig. 2.2A, Y+B-). The total amount of myosin contained within clusters did not shift significantly compared to the cells treated with both inhibitors (fig. 2.2C). To quantify the size distribution of myosin clusters across different conditions, we fitted the myosin cluster intensity distribution to a lognormal distribution and used the mode of this distribution to represent the most probable myosin cluster size. The mode of myosin cluster intensity only marginally changed with blebbistatin washout, (fig. 2.2D). This suggests that myosin motor activity in the absence of ROCK activity is insufficient for myosin clusters growth.

In contrast, when Y-27 is removed but blebbistatin is retained, the total amount of myosin contained within clusters across the lamella increased by ∼42% (fig. 2.2A, fig. 2.2C, Y-B+). From the histogram of myosin cluster sizes, we estimate that myosin clusters grow up to $4 - 15$ times the size of N_{min} with ROCK activity alone (fig. 2.2B, Y-B+). Compared with myosin cluster size distributions in cells treated with both inhibitors, the peak of the distribution shifts towards larger sizes and the tail widens with ROCK activity. This indicates both that the most probable myosin cluster size and the fraction of larger myosin clusters increased. This is also shown by the increasing mode of myosin cluster intensity when Y-27 is selectively washed out (fig. 2.2D). Interestingly, myosin cluster density remained at similar levels in all drug conditions (fig. 2.2E). This suggests that ROCK activity is sufficient for myosin clusters to grow, not through forming new clusters but through the accumulation of myosin to existing clusters.

To visualize ROCK-mediated myosin cluster growth, we conducted live-cell imaging of fluorescently-tagged myosin as Y-27 is selectively washed out in cells treated with both Y-27 and blebbistatin (fig. 2.3A). As Y-27 is washed out, the intensities of myosin clusters increased over 20 minutes (fig. 2.3A, B). The dynamics of individual myosin clusters reveal that most clusters are very mobile and only appear transiently for a few frames after washing out Y-27 (fig. 2.3C, Supp. Movie 2). We think this does not represent rapid assembly and

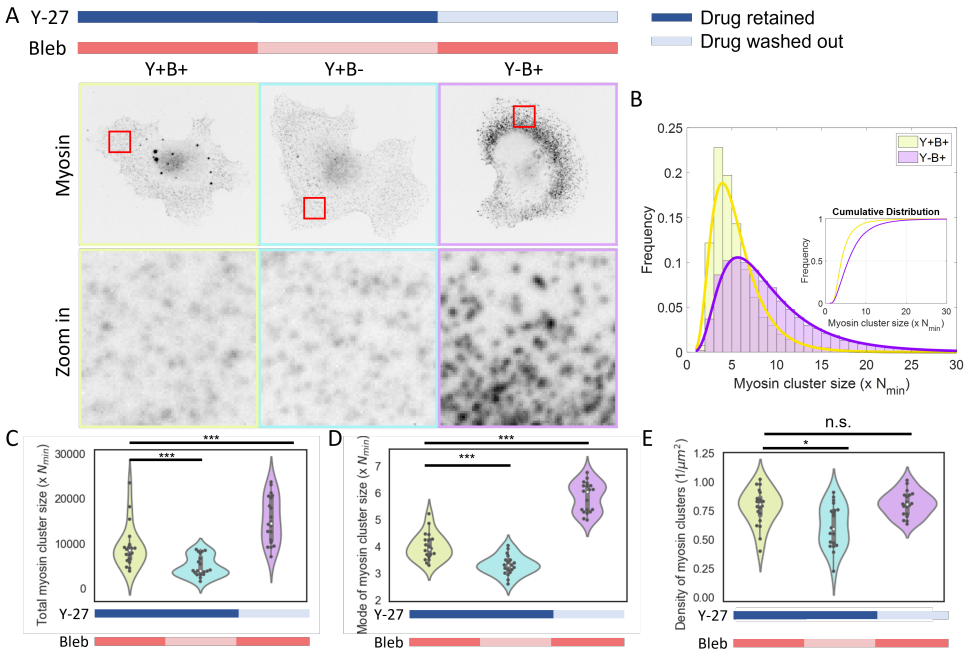

Figure 2.2: **ROCK activity is sufficient for myosin clusters to grow in the absence of myosin motor activity.** (A) Top row shows the representative myosin images of cells with or without ROCK activity and myosin motor activity. Myosin clusters were first disassembled by both Y-27632 and blebbistatin (Y+B+). Y27 or blebbistain are then either removed individually (Y+B- and Y-B+). Zoomed in myosin images are shown in the bottom row. Images are inverted. Scale bar is 10 µm for the top row and 2 µm for the bottom row. (B) Histogram of myosin cluster size between Y27/blebbistatin treated and blebbistatin treated cells. Inset shows the cumulative distribution of cluster sizes. (C) The sum of myosin cluster sizes. (D) Mode of myosin cluster size distribution. (E) Density of myosin clusters. N=20 cells for each condition. Two-sample Kolmogorov-Smirnov tests were performed in (C)-(E) to test if the measured quantity differs between conditions. n.s. signifies $p>0.05$, * signifies $p<0.05$ and *** signifies $p<0.001$.

disassembly dynamics but instead reflects that myosin is weakly bound to F-actin due to blebbistatin treatment and, consequently, leave the field of view. It is therefore challenging to track single myosin clusters over time. Nevertheless, we observed some myosin clusters growing in intensity without apparent interaction with other clusters (fig. 2.3D). This suggests that myosin clusters grow via a net association of myosin monomers or filaments to existing myosin clusters, potentiated by the increase in assembly-competent myosin driven by ROCK activity (fig. 2.3E). Moreover, myosin clusters that appear at later times have

higher intensities than myosin clusters that appear earlier in the washout (fig. 2.3C). This suggests that myosin clusters may grow while diffusing around the cytoplasm.

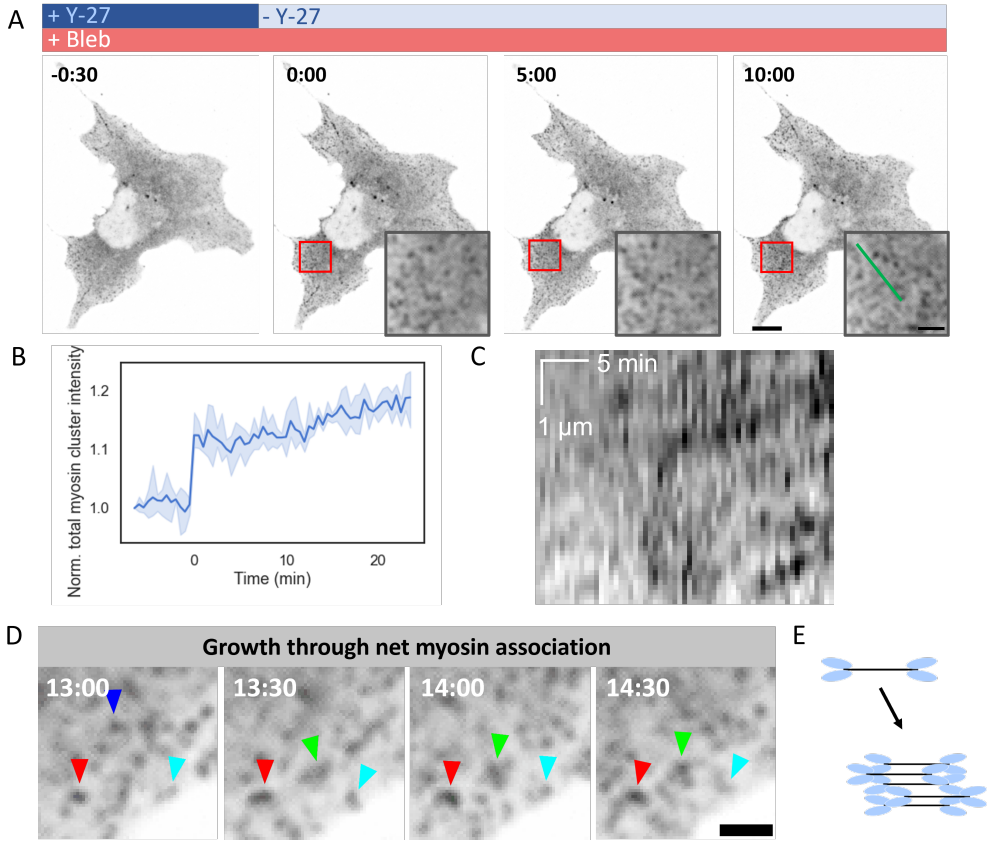

Figure 2.3: **Myosin clusters grow through net association of myosin to existing clusters without myosin motor activity.** (A) Snapshots of myosin clusters after washing out Y-27632 from Y-27632/blebbistatin treated cells. Time after washout is shown on the top left corner of each image. Inset shows zoom-in of myosin clusters in the red squares. Images are inverted. Scale 10 µm. Inset scale 2 µm. (B) The sum of intensities of all myosin clusters in the cell, normalized to their intensities before washout. N=3 cells. (C) Kymograph of myosin clusters along the green line in the inset in (A). Horizontal axis represents time and vertical axis represents spatial position. Time scale 5 minutes and spatial scale 1 µm. (D) Close-up snapshots of myosin cluster growth over time. Top-left indicates time after washout. Arrowheads indicate trackable myosin clusters over time. (E) Schematic of myosin association to existing clusters.

2.4 Myosin motor activity allows myosin clusters to grow through F-actin-dependent myosin association

Our results so far show that ROCK activity is sufficient for myosin cluster growth without myosin ATPase activity. However, myosin cluster sizes are still significantly smaller than wild-type clusters (fig. 2.1E & fig. 2.2B). Therefore, we explored the role of myosin motor activity plays. To this end, we compared myosin cluster sizes in cells treated with blebbistatin with untreated cells (fig. 2.4A). We see that the total myosin contained in clusters decreased by about 35% with blebbistatin treatment (fig. 2.4C). This is consistent with previous studies showing that myosin motor activity affects myosin filament assembly [54]. At the level of single myosin clusters, most myosin clusters in blebbistatin-treated cells contain around 4 times more myosin than N_{min} but can contain up to 18 times more than N_{min} (fig. 2.4B), which is consistent with the case when Y-27 is washed out in cells treated with Y-27 and blebbistatin (fig. 2.2B, Y-B+). In contrast, while the most probable myosin cluster size only modestly increased to 5 – 6 times more than N_{min} in control cells (fig. 2.4B, D), there is a larger fraction of myosin clusters that contain more than 15-fold of N_{min}, reaching up to 28-fold of N_{min} (fig. 2.4B). As in the case of ROCK-dependent myosin cluster growth, myosin cluster density remains the same with blebbistatin treatment (fig. 2.4E).

To understand how myosin motor activity can further enhance myosin cluster size, we performed live-cell myosin imaging as we washed out blebbistatin (fig. 2.5A, Supp. Movie 3). Consistent with fix and stain results, myosin cluster intensity increased as blebbistatin is washed out (fig. 2.5B). During this process, myosin clusters are more stably bound, persisting for more than 10 minutes (fig. 2.5C). Some myosin clusters increase intensity over time without apparent local motion or interaction with neighboring clusters, suggesting an increased net myosin association to existing clusters (fig. 2.5C, D). We also observe some myosin clusters undergo local motion toward each other and merge into a brighter cluster (fig. 2.5C, E), suggesting myosin cluster growth through actomyosin sliding.

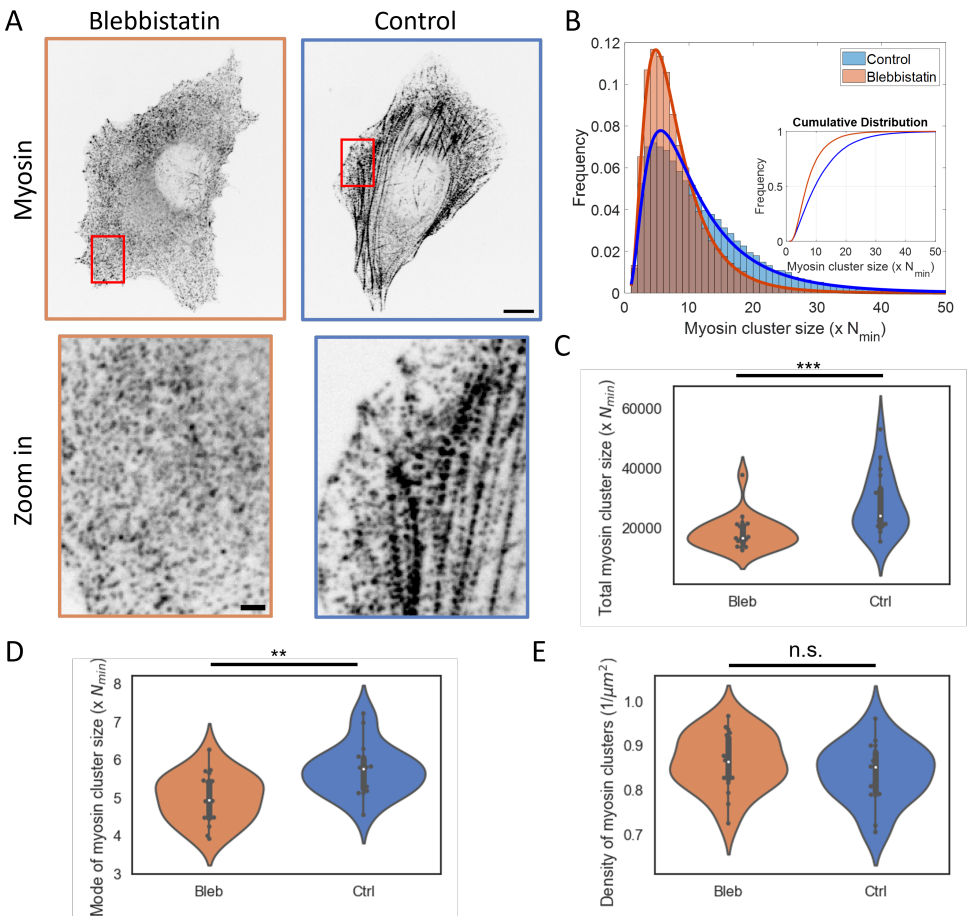

Figure 2.4: **Myosin motor activity allows for myosin cluster growth.** (A) Top row shows representative myosin images in cells treated with or without blebbistatin. Bottom row shows zoomed-in myosin images in the red boxes in the top row. Images are inverted. Scale bar is 10 µm for the top row and 2 µm for the bottom row. (B) Histogram of myosin cluster sizes between blebbistatin treated and control cells. Inset shows the cumulative distribution of both conditions. (C) The sum of all myosin cluster sizes. (D) Mode of myosin cluster size distribution. (E) Density of myosin clusters. N=20 cells for blebbistatin-treated cells and N=18 cells for control cells. Two-sample Kolmogorov-Smirnov tests were performed in (C)-(E) to test if the measured quantity differs between conditions. n.s. signifies $p>0.05$, ** signifies $p<0.01$ and *** signifies $p<0.001$.

Since blebbistatin does not impact RLC phosphorylation, we reasoned that myosin motor activity can only indirectly affect myosin association. Since F-actin has been proposed to regulate myosin assembly and myosin cluster growth at the leading edge [46, 47, 62], we wondered if F-actin could play a role. Consistent with this idea, myosin cluster sizes across

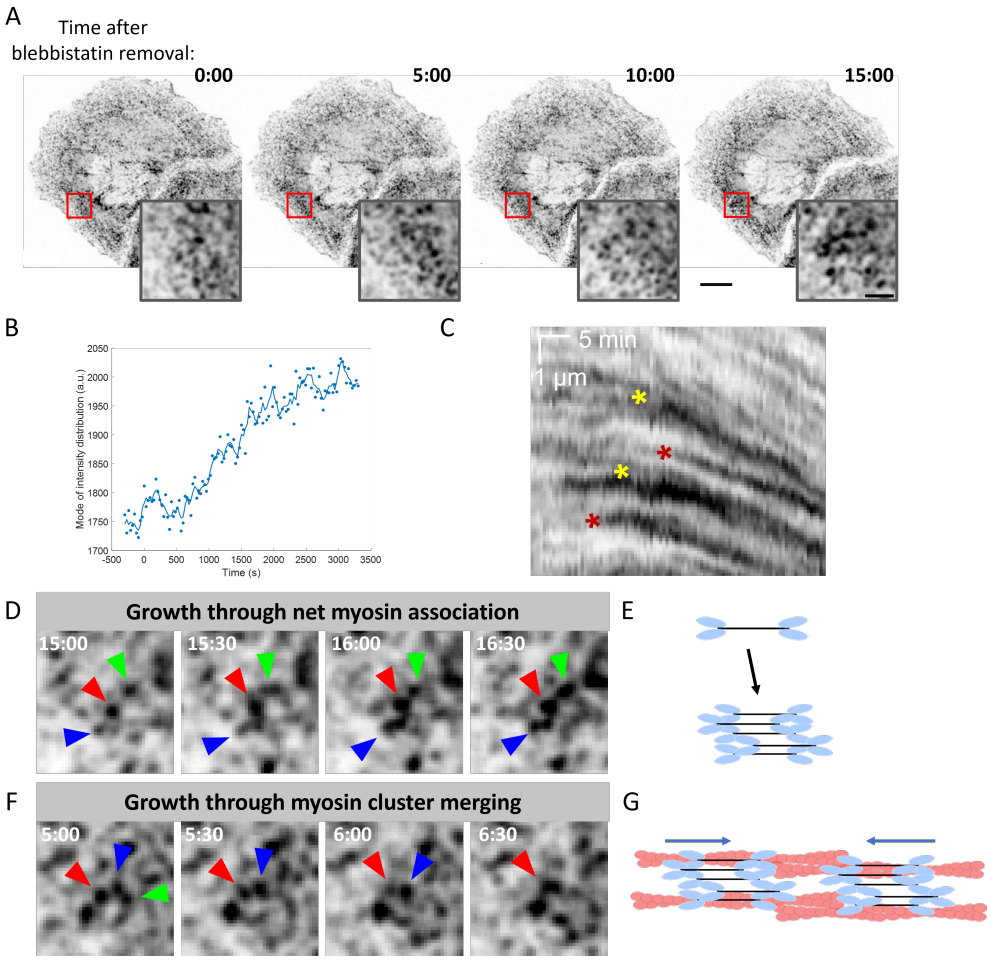

Figure 2.5: **Myosin motor activity grows myosin clusters through net myosin association or cluster merging.** (A) Snapshots of time-lapse imaging of myosin clusters during blebbistatin washout. Inset shows zoom-in of myosin clusters in the red squares. Images are inverted. Scale bar 10 µm. Inset scale bar 2 µm. (B) Myosin cluster intensity increases with blebbistatin washout. (C) Kymograph of myosin clusters. Maroon asterisks indicate cluster growth events through myosin association and yellow asterisks indicate two clusters merging. (D) Close-up snapshots of myosin clusters increasing intensity over time through net myosin association. Arrowheads indicate example myosin clusters. (E) Schematic of myosin association with existing clusters. (F) Close-up snapshots of myosin clusters increasing intensity through merging with another cluster driven by actomyosin sliding. Arrowheads indicate example myosin clusters. (G) Schematic of myosin cluster growth via actomyosin sliding.

the cell positively correlate with the underlying F-actin intensity (Supp. Fig. 3). Since different stress fiber architecture contains variable amounts of myosin, we restricted our analysis to mature transverse arcs and ventral stress fibers. On these stress fibers, myosin

cluster sizes correlate strongly with the intensity of F-actin bundles (fig. 2.6A, C). On the other hand, there are few F-actin bundles in blebbistatin-treated cells. On these bundles, however, myosin cluster sizes showed much less positive correlation with the intensity of remaining F-actin bundles (fig. 2.6B, C). Since both the slope and R^2 of the correlation decreased with blebbistatin treatment (fig. 2.6D, E), this suggests that F-actin plays a role in myosin cluster growth only in the presence of myosin motor activity and/or strong binding.

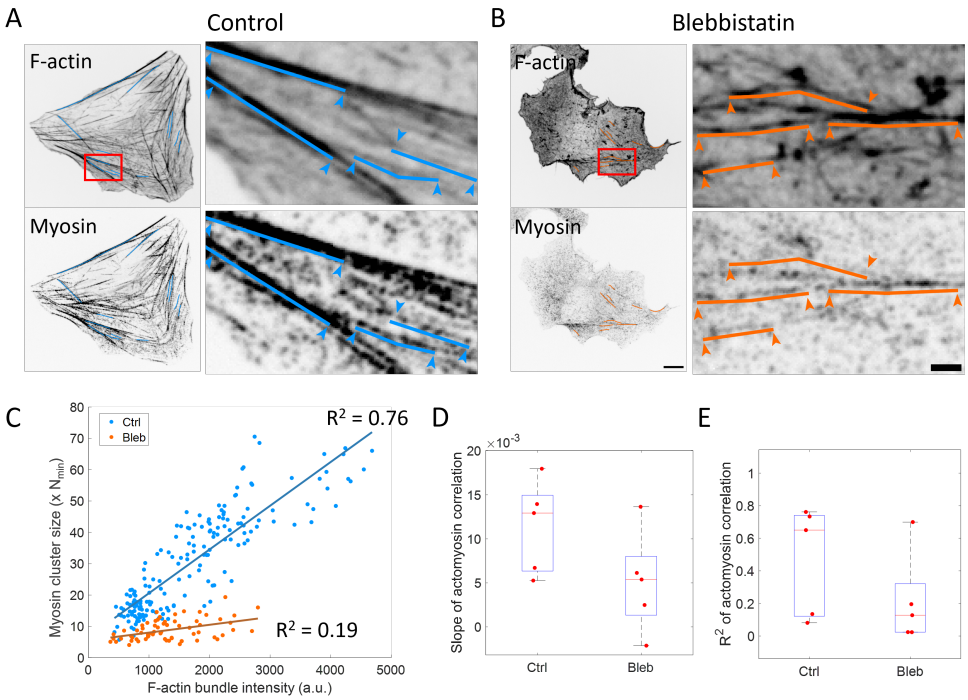

Figure 2.6: **Myosin cluster sizes correlate with F-actin bundle intensity under myosin motor activity.** (A) F-actin and myosin on select F-actin bundles in control cells. Left column shows all segments of F-actin bundles that are selected for analysis. Right column shows zoomed in view of a few F-actin bundles. Solid lines represent F-actin bundles where actomyosin correlation is examined. Arrowheads indicate the end points of the segment. (B) F-actin and myosin on select F-actin bundles in blebbistatin-treated cells. Scale bar is 10 µm for the whole cell image and 2 µm for the zoomed in image. (C) Correlation between myosin cluster size and F-actin bundle intensity in control and blebbistatin-treated cells. Correlation is plotted for myosin clusters on every selected bundles in a single cell. (D) Slope of the correlation. N=5 cells in each condition. (E) R^2 of the correlation. N=5 cells in each condition.

To further understand how F-actin architecture affects myosin cluster size, we perturb

the stress fiber architecture and see how myosin clusters respond. First, we disrupted F-actin crosslinking by knocking down α-actinin1 via siRNA. Under α-actinin1 knock-down, dorsal stress fibers were abolished, and transverse arc bundles reduced in actin intensity (fig. 2.7A, B), which agrees with previous reports [2, 63]. The total amount of myosin within clusters across the lamella does not change significantly (Supp. Fig. 4B), which is also consistent with a previous report that RLC phosphorylation levels remain unchanged [2]. However, the sizes of myosin clusters shifted towards smaller sizes (Supp. Fig. 4A). While the most probable size of myosin clusters is similar (Supp. Fig. 4C), myosin clusters can only grow up to 20 times of N_{min} as opposed to the 30 times of N_{min} in control conditions. The density of myosin clusters also remains unchanged under α-actinin knockdown (Supp. Fig. 4D). The concurrent disruption in F-actin bundles and large myosin clusters suggests that myosin association to F-actin bundles reduced under α-actinin1 knockdown. Indeed, when we look at cluster sizes on larger transverse arcs or ventral stress fibers, myosin cluster sizes exhibit reduced positive correlation with F-actin bundle intensity (fig. 2.7C). Both the slope and R^2 of the correlation decreased with α-actinin1 knockdown (fig. 2.7D, E). This suggests that myosin cluster sizes on F-actin bundles are reduced when F-actin bundles are disrupted.

On the other hand, we saw a qualitatively different result when we disrupted the smallest F-actin bundles and meshwork within the lamella by treating cells with low doses of latrunculin A (LatA). Upon treatment with 50 nM LatA, large F-actin bundles such as ventral stress fibers became the dominant F-actin architecture in cells while thin F-actin bundles were depleted (fig. 2.7F, G). The sizes of myosin clusters didn't change significantly (Supp. Fig. 4E & 4G), but the total amount of myosin within clusters decreased (Supp. Fig. 4F) due to the decrease in myosin cluster density (Supp. Fig. 4H). With thin F-actin bundles depleted, myosin clusters accumulated more on larger transverse arcs and ventral stress fibers, as seen by the larger slope of the positive correlation between myosin cluster sizes with F-actin bundle intensity (fig. 2.7H, I). The R^2 of the correlation remained similar

(fig. 2.7J). Together with the α-actinin1 knockdown results, our results suggest that myosin cluster sizes depend on the underlying F-actin architecture.

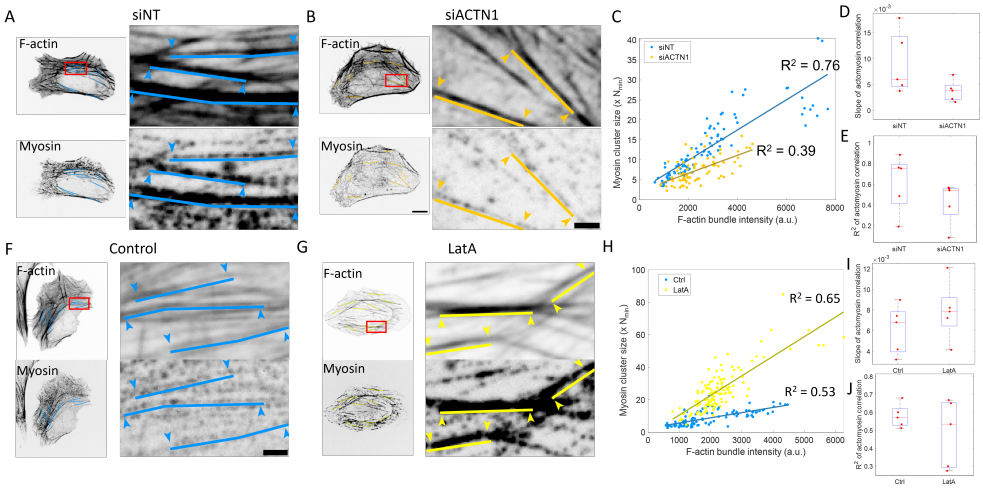

Figure 2.7: **Myosin association to F-actin bundles depends on F-actin architecture.** (A) F-actin and myosin on select F-actin bundles in scramble siRNA-treated cells. Left column shows all segments of F-actin bundles that are selected for analysis. Right column shows zoomed in view of a few F-actin bundles. Solid lines represent F-actin bundles where actomyosin correlation is examined. Arrowheads indicate the end points of the segment. (B) F-actin and myosin on select F-actin bundles in α-actinin1 siRNA-treated cells. Scale bar is 10 µm for the whole cell image and 2 µm for the zoomed in image. (C) Correlation between myosin cluster intensity and F-actin bundle intensity in scramble and α-actinin1 siRNA-treated cells. Correlation is plotted for myosin clusters on every selected bundles in a single cell. (D) Slope of the correlation between scramble and α-actinin1 siRNA-treated cells. N=5 cells in each condition. (E) R^2 of the correlation between scramble and α-actinin1 siRNA-treated cells. N=5 cells in each condition. (F) F-actin and myosin on select F-actin bundles in control cells. (G) F-actin and myosin on select F-actin bundles in LatA-treated cells. Scale bar is 10 µm for the whole cell image and 2 µm for the zoomed in image. (H) Correlation between myosin cluster intensity and F-actin bundle intensity in control and LatA-treated cells. Correlation is plotted for myosin clusters on every selected bundles in a single cell. (I) Slope of the correlation between control and LatA-treated cells. N=5 cells in each condition. (J) R^2 of the correlation between control and LatA-treated cells. N=5 cells in each condition.

2.5 Myosin cluster growth with a positive feedback is sufficient to recapitulate the broad range of myosin cluster sizes

With our experimental results showing myosin clusters growing via net association to existing clusters, we wanted to quantitatively describe myosin cluster growth. To this end, we constructed a toy model to simulate myosin cluster growth. We modeled myosin cluster growth as a Monte Carlo process, where a predetermined number of myosin filaments (N_{myo}) iteratively bind randomly to a 1D grid of 10000 points. The number of grid points is fixed because myosin cluster density remained similar across almost all experimental conditions (fig. 2.2E and fig. 2.4E). The simulation iterates through all myosin filaments, where one myosin filament binds randomly to a grid point in each iteration. (fig. 2.8A). The probability for the myosin filament on a given iteration to bind to grid point i is given by $P_i = \frac{1+\alpha M_i}{\sum_i P_i}$, where M_i is the number of myosin filaments at that grid point. The parameter α is an affinity parameter that captures scenarios where myosin filaments preferentially bind to existing myosin clusters. This is motivated by recent literature that suggests myosin filaments preferentially bind to existing myosin clusters [46, 47, 60].

First, we use our toy model to simulate myosin cluster growth without myosin motor activity, specifically when Y-27 is washed out in cells treated with both Y-27 and blebbistatin (fig. 2.2A & fig. 2.8B, i). To make a meaningful comparison between the simulation and experiments, we initialized the simulation such that the size of myosin clusters on each grid matches the size distribution in cells treated with both Y-27 and blebbistatin (fig. 2.8B, i, Y+B+). This is done assuming N_{min} represents one myosin filament. As a result, the initial total amount of myosin within clusters in the simulation is approximately 47000. Since our experimental results showed that ROCK-dependent myosin cluster growth increases assembled myosin by about 42% (fig. 2.2C), the simulation iterates through the binding of approximately 20000 additional myosin filaments. If we assume that myosin filaments can bind to each grid point with equal probability (α=0), corresponding to uniform growth rates

across the cell, the myosin cluster sizes at the end of the simulation exhibit a Gaussian-like distribution (fig. 2.8B, ii). However, this result contradicts the experimentally observed lognormal distribution when we selectively wash out Y-27 (fig. 2.8B, i, Y-B+). When the affinity parameter is non-zero (α>0), the simulated cluster sizes start to qualitatively recapitulate the lognormal distribution of myosin cluster sizes in the absence of myosin motor activity (fig. 2.8B, iii). We quantified the error between simulated and experimental cluster sizes by calculating the average distance between the cumulative distributions of experimental-measured and simulated myosin cluster sizes. The error decreased with increasing α but started to converge around α=10 (Supp. Fig. 5). This suggests that the simulated results became insensitive to changes in α, presumably due to the finite size of our simulation setup. On the other hand, the simulated results depend heavily on the number of myosin iterated through the simulation. When we scan through a range of N_{myo}, the simulation error is the lowest when N_{myo} is 20000, which coincides with experimentally quantified results (fig. 2.8B, iv)! This suggests that the limiting pool of available myosin is important for setting myosin cluster sizes.

We next explored if the same simulation framework and parameters can capture myosin cluster growth under myosin motor activity, specifically when blebbistatin is washed out from cells (fig. 2.4A & fig. 2.8C, i). To make a meaningful comparison with experiments, we initialized the simulation such that myosin cluster size on each grid matches the myosin cluster size distribution in blebbistatin-treated cells (fig. 2.8C, i). Using the same assumption as before, the initial total myosin contained in clusters in the simulation is approximately 81000. Since untreated cells show 54% more assembled myosin than blebbistatin-treated cells in our experimental quantification (fig. 2.4C), the simulation iterates through the binding of about 44000 additional myosin filaments. As in the case of myosin cluster growth without motor activity, uniform myosin binding probability (α=0) fails to capture the lognormal distribution of myosin cluster sizes in control cells (fig. 2.8C, ii). When the affinity parameter is

non-zero (α>0), the simulated result once again qualitatively recapitulated the experimental cluster sizes in control cells (fig. 2.8C, iii). The error between simulated and experimental results decreased with increasing α but again converged around α=10 (Supp. Fig. 5). The optimal N_{myo} that produces the least error between simulated and experimental results is around 37500, which is about 15% less than the experimentally measured N_{myo} (fig. 2.8C, iv). This is likely due to the F-actin-dependent myosin cluster regulation not captured in this toy model. Taken together, our results suggest that myosin cluster sizes on stress fibers are set by a limiting pool of myosin available for cluster growth with myosin self-affinity.

2.6 Discussion

Our results combining experiments and simulations are consistent with the picture that myosin clusters grow by myosin association to a set number of myosin clusters. We found that the most important factor that determines myosin cluster size is the limited availability of cytoplasmic myosin available to to grow clusters. We find this is regulated by both ROCK and myosin motor activity (fig. 2.9). F-actin architecture can further regulate myosin cluster sizes (fig. 2.9). On the other hand, the nucleation of myosin clusters is independent of these regulations, as we found that the density of myosin clusters remains at similar levels. This is consistent with the idea that the sizes of subcellular organelles can be controlled by the competition for a limiting pool of available components, as proposed for flagella, centrosomes, and F-actin architectures [64, 65]. This insight is only possible through our combination of endogenous tagging, quantitative imaging, analysis, perturbation, and modeling.

A novel finding of this study is that myosin cluster growth can occur independently of myosin motor activity. ROCK activity alone allows myosin clusters to grow from 3 times to 4-15 times the size of N_{min}. Since myosin self-affinity is required for our in silico model to recapitulate experimental results, our results suggest that there is biochemical affinity between myosin filaments. This may explain the stack or ribbon configuration of myosin clusters ob-

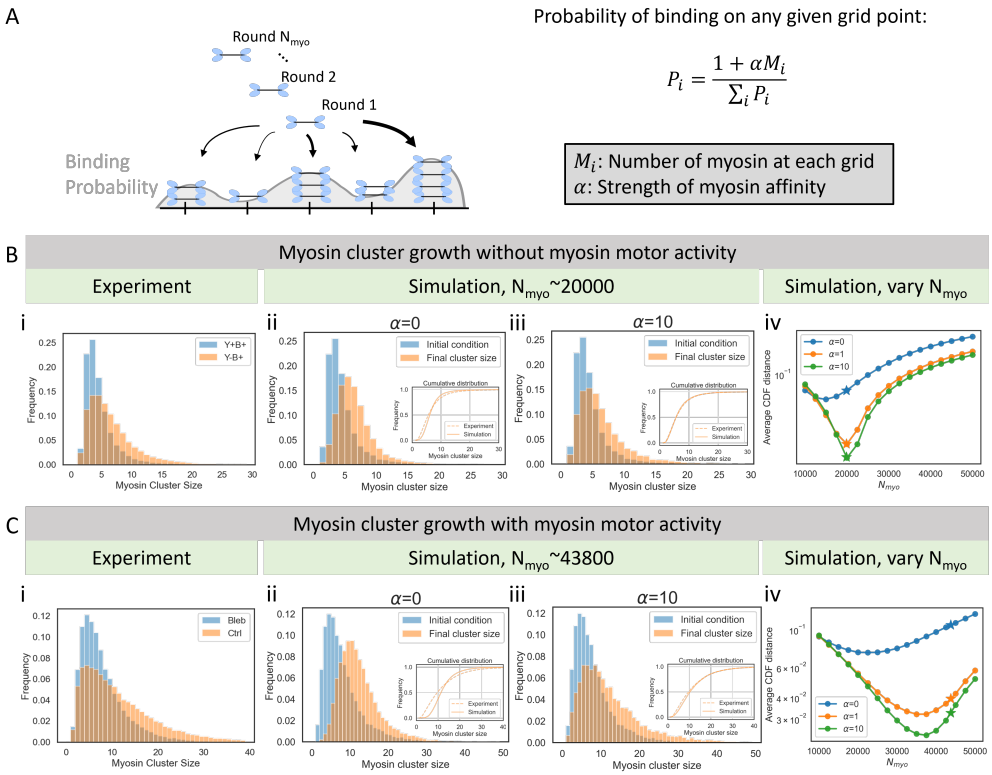

Figure 2.8: **Myosin cluster growth with positive feedback is sufficient to recapitulate the broad range of myosin cluster sizes.** (A) Schematic of the simulation setup. (B) Simulation of myosin cluster growth without myosin motor activity. (i) Experimentally observed myosin cluster size distribution in cells before (Y+B+) and after (Y-B+) washing out Y-27 in cells that are treated with both Y-27 and blebbistatin. (ii) Simulation when myosin binding probability is uniform across all grid points (α=0). Inset shows the cumulative distribution of the experimental and simulated results. (iii) Simulation when myosin has an affinity toward existing myosin clusters (α=10). Inset shows the cumulative distribution of the experimental and simulated results. (iv) Average distance between cumulative distributions of the experimental and simulated cluster sizes across different α and N_{myo} values. Stars show the N_{myo} determined by experimental quantifications. (C) Simulation of myosin cluster growth with myosin motor activity. (i) Experimentally observed myosin cluster size distribution in cells treated with blebbistatin or control cells. (ii) Simulation when myosin binding probability is uniform across all grid points (α=0). Inset shows the cumulative distribution of the experimental and simulated results. (iii) Simulation when myosin has an affinity toward existing myosin clusters (α=10). Inset shows the cumulative distribution of the experimental and simulated results. (iv) Average distance between cumulative distributions of the experimental and simulated cluster sizes across different α and N_{myo} values. Stars show the N_{myo} determined by experimental quantifications.

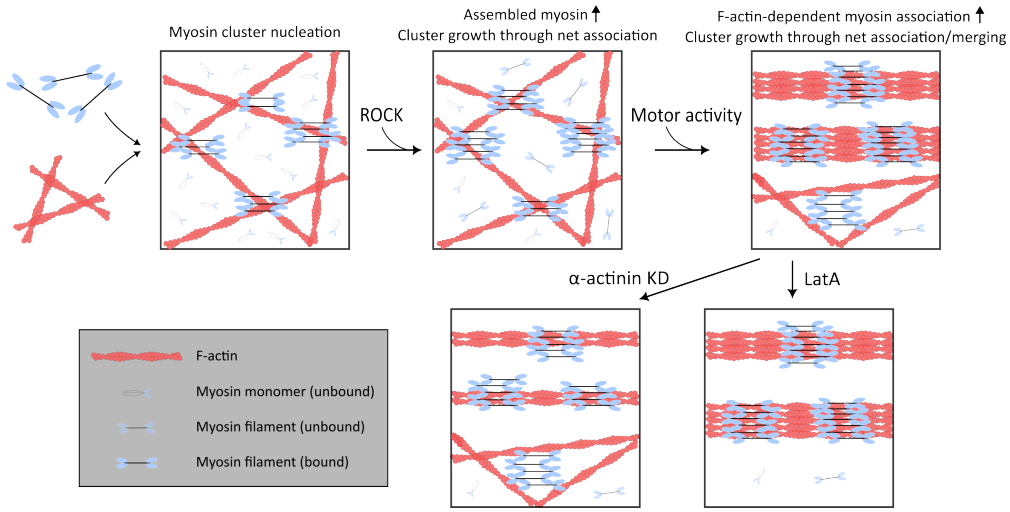

Figure 2.9: **Myosin cluster sizes are set by a limiting pool of myosin that are available for cluster growth.** Myosin filaments independent of ROCK activity nucleates myosin clusters. ROCK activity increases myosin assembly, which increases the pool of myosin available for cluster growth through increased net association. Myosin motor activity further enhances myosin cluster growth through F-actin-dependent myosin association. Myosin cluster sizes on F-actin bundles decreased when mature F-actin bundles are disrupted by α-actinin1 knockdown, and increased when thin F-actin bundles are depleted by LatA.

served with platinum EM [44, 45]. However, to the best of our knowledge, there is no reported molecular or electrostatic interaction between pairs of assembled myosin filaments. We speculate that the affinity can arise from numerous weak intermolecular interactions between heads, light chains, and tails of myosin monomers in neighboring myosin filaments [66]. These interactions can be amplified when multiple myosin filaments are involved. This is supported by a previous study that reported purified NMIIA can form large clusters in vitro [16]. Alternatively, the affinity between myosin filaments can be indirectly mediated by other molecular components. For example, some proteins associate strongly with myosin filaments and have been proposed to regulate myosin structures, such as myosin-18B [67] or Tpm 3.1 [68]. This will be an interesting topic for future research to identify the cause of myosin self-affinity, and the effect on myosin clusters when this interaction is disrupted.

Myosin cluster growth can also occur with myosin motor activity mainly through the addition of available myosin to existing myosin clusters. We think that this is due to the

increase in myosin assembly from myosin ATPase activity. While myosin motor activity doesn't affect the phosphorylation of the RLC, previous studies have reported the reduction in myosin filament assembly under blebbistatin treatment [54]. This has been attributed to the effect of mechanical tension on myosin assembly, specifically because of the catch-bond nature of myosin-actin interaction [27, 54, 69]. While recent studies suggest that only NMIIB exhibit catch-bond behavior while NMIIA is more like a slip-bond [58], NMIIA assembly can in principle be affected by NMIIB since NMIIA and NMIIB have been shown to co-polymerize into filaments [28, 55]. Another possible molecular process that can result in myosin cluster growth under myosin motor activity is through the coalescence of myosin clusters resulting from their lateral motion promoted by actomyosin sliding. While coalescence occurs over a longer time scale than the association of free myosin, this can serve as a parallel mechanism for myosin cluster growth or as a means to organize the quasi-sarcomeric pattern [70].

The correlation between myosin cluster sizes and F-actin bundle size may be a result of nuanced feedback between F-actin and myosin clusters, with possible mutual regulation between myosin clusters and F-actin bundle size. On one hand, myosin can be regulated by F-actin. At the molecular level, it has been reported that myosin assembly is enhanced in the presence of F-actin [62, 71, 72]. Some actin-binding protein can also regulate myosin motor activity, such as tropomyosin [73]. On the other hand, myosin can remodel the F-actin network. For example, myosin filaments can contract and remodel F-actin networks into asters [74, 75, 76]. The combined effect can effectively create a positive feedback loop to give rise to the correlation between myosin cluster sizes and F-actin bundle size.

Our understanding of myosin cluster regulation is consistent with the idea that the number and size of subcellular organelles are tightly controlled [77, 78, 79]. One model of organelle size control is that a limited pool of cytoplasmic components sets the size of these structures. This concept has been demonstrated in several organelles, such as the flagella [80], centrosomes [81], and mitotic spindles [82]. Similarly, structures that depend on the same

building blocks can compete for these limited components, as observed with different F-actin architectures [51, 65] and myosin clusters on various actomyosin structures [47, 83]. Our paper contributes to this idea by quantitatively demonstrating its applicability in stress fibers of non-muscle cells. We believe that our approach, combined with advanced microscopy, molecular biology, and perturbation techniques, will lead to further insight into how cells balance and control organelles.

2.7 Methods

2.7.1 Cell culture

U2OS cells were cultured in McCoy's 5A Medium (Sigma-Aldrich) supplemented with 10% FBS (Corning) and 2 mM L-glutamine (Invitrogen). To visualize myosin, mScarlet was knocked in at the C-terminal locus of the MYH9 gene using CRISPR. The target/Cas9 plasmid pSpCas9(BB)-2A-Puro (PX459) V2.0 (http://www.addgene.org/62988/) with target sequence AGGTAGATGGCAAAGCGGAT was engineered according to established protocols (Ran et al, 2013). To create a donor plasmid, pUC57 was digested with EcoRI and StuI and purified. A four-piece Gibson assembly was then performed. Three gBlocks (5' HDR, linker/mScarlet, and 3'HDR) were obtained from IDT with overlapping extensions to mediate Gibson assembly. The 5' HDR arm is 867 bp of genomic sequence terminating immediately prior to the endogenous STOP codon. Silent mutations (AaGTtGAcGGaAAAGCGGATGGt) were placed in the target sequence to prevent Cas9 binding and cleavage of the donor plasmid. The linker/mScarlet was placed in-frame with the coding sequence and consists of an 18 amino acid GS rich linker and mScarlet-I fluorophore. The 3' HDR arm is 684 bp immediately downstream of the MYH9 coding sequence. U2OS cells were transfected with both Cas9 and donor plasmids. After 1 week in culture, a polyclonal mScarlet positive population was obtained using fluorescent activated cell sorting (FACS).

For fluorescent recovery after photobleaching (FRAP) experiments, eGFP was knocked in at the N-terminal locus of the MYH9 gene instead. The following modifications were made for the CRISPR procedure. The target sequence for the guide RNA is AAACTTCATCAACAATCCGC. Donor plasmid was generated in pUCIDT-AmpR with internal mEGFP flanked by 5' and 3' HDR. The 5'HDR is 498 bp upstream of endogenous start and 3'HDR is 383 bp downstream of endogenous start. All cells were previously treated with BM cyclin (Roche) per manufacturer instructions to eliminate mycoplasma.

2.7.2 Drug Perturbations and Gene Knockdown

Cells were treated with 40 µM Y-27632 (EMD Millipore) or 50 µM blebbistatin (Millipore-Sigma) for at least 30 minutes. Latrunculin A (Sigma-Aldrich) is used at a sub-saturating concentration of 50 nM for 30 minutes. To knock down α-actinin, ON-TARGETplus SMARTpool human ACTN1 siRNA is used per manufacturer instructions (Horizon Discovery). For siRNA control, ON-TARGETplus non-targeting siRNA is used (Horizon Discovery).

2.7.3 Immunofluorescence

Cells were first washed with warm PBS. Then cells were fixed and permeabilized with 4% paraformaldehyde (EMS) and 0.5% Triton X-100 (Fisher Scientific), diluted in 1.5% BSA (Fisher Scientific) and cytoskeletal buffer (0.01M MES, 0.003M MgCl2, 0.138M KCl, 0.002M EGTA, pH 6.8). To visualize F-actin, cells were then washed with PBS then incubated with Alexa-647 phalloidin (SIGMA? 1:1000), 0.5% Triton X-100, and 1.5% BSA diluted in cytoskeletal buffer. Cells were then washed with PBS and mounted onto a coverslip with ProLong gold antifade reagent (Invitrogen).

2.7.4 Microscopy and Live Cell Imaging

Cells were imaged on an inverted Nikon Ti-E (Nikon, Melville, NY) with a Yokogawa CSU-X confocal scanning head (Yokogawa Electric, Tokyo, Japan) and laser merge model with 491, 561, and 642nm laser lines (Spectral Applied Research, Ontario, Canada). Images were collected on a Zyla 4.2 sCMOS Camera (Andor, Belfast, UK). A 60x 1.2 Plan Apo water (Nikon) objective was used to collect images. MetaMorph Automation and Image Analysis Software (Molecular Devices, Sunnvyale,CA) controlled all hardware. For quantitative myosin cluster size analysis, all imaging conditions are controlled to be the same in each set of experiments, including laser intensity and exposure time. For fluorescence recovery after photobleaching (FRAP) experiments, Airyscan imaging was performed on a Zeiss LSM 980 microscope equipped with the Airyscan 2 detector. Images were acquired using the MPLX SR-4X mode and processed by Zen Blue 3.0 software using the Airyscan processing feature with default settings. For live cell imaging, cells were mounted on an imaging chamber (Chamlide) and maintained at 37 °C. For live cell imaging, cell medium was replaced with Dulbecco's Modified Eagle Medium without phenol red (Corning) supplemented with 10% FBS, 2mM L-glutamine, 1% penicillin-streptomycin, 10mM HEPES and 30 µL/mL Oxyrase (Oxyrase Inc.).

2.7.5 Image Processing

For the quantification of myosin cluster sizes, confocal images were captured ∼2 µm around the focal plane to capture all intensities and z projection ∼1 µm was performed around the focal plane where myosin is in focus. To remove diffuse myosin background, immunofluorescence images were first background subtracted using a top-hat filter with a circular element with a diameter of 50 pixels. Then myosin clusters were localized using a feature-finding code [59]. The identified features were filtered based on the general criteria: minimum intensity, maximum radius of gyration, maximum eccentricity, and intensity divided by radius

of gyration. Features outside of the cell area and features closer than 2 pixels apart (0.2 µm) were also excluded. Myosin puncta intensity were then fitted to a lognormal distribution using maximum-likelihood estimation (Matlab).

Live-cell imaging movies were first corrected for photobleaching. The photobleaching curve was generated by summing all pixel intensities within a cell. The photobleaching curve is then fitted empirically to a double exponential decay function of the form $q(t) = Ae^{-bt} + (1-A)e^{-ct}$. Then intensities were corrected by dividing the imaging intensity to the curve $I_{corrected}(t) = \frac{I(t)}{q(t)}$. Afterwards, movies were either denoised by applying a spatial Gaussian filter (sigma=1 pixel) or by Noise2Void [84].

To analyze FRAP experiments, both FRAP and control regions were identified. A double normalization scheme is used to normalize data and correct for photobleaching $I_{corr} = \frac{I_{roi}}{I_{ref}}\frac{I_{ctrl,pre}}{I_{roi,pre}}$. The FRAP curve is fitted to $FRAP(t) = C(1-e^{-\alpha t})$ to extract the recovery half time $\tau_{1/2} = \frac{ln2}{\alpha}$ and the mobile fraction C. All analysis codes are available upon request.

2.7.6 Simulation of Myosin Cluster Growth

The simulation setup is summarized in the main text. To match the initial myosin cluster size distribution in the simulation with experimental conditions, each grid point is initialized with a cluster size that is randomly sampled from the experimental cumulative distribution of cluster sizes. After all grid points have been initialized, the initial total cluster size can be calculated, and N_{myo} can be determined by percent increase of total myosin cluster sizes in experimental quantifications as described in the main text. The simulation iterates through the random binding of N_{myo} myosin filaments to a grid. In each iteration, one myosin filament binds to a grid chosen by the default Python function choices, with the probability to choose each grid being $P_i = \frac{1+\alpha M_i}{\sum_i P_i}$ as described in the main text. Code is available on Github.

CHAPTER 3

MYOSIN CLUSTER DYNAMICS REVEALS THE MATERIAL RESPONSE OF STRESS FIBER NETWORKS

3.0 Preamble

This chapter documents a collaborative project with Mehdi Molaei, Steven Redford, and others to develop a generalized method to extract material response functions directly from experimental data. From measured velocity fields of active actomyosin systems, the material response function reveals interesting material properties such as viscoelasticity. While the method was applied to various reconstituted actomyosin networks *in vitro* (sections 3.2 through 3.5), We also applied the method to the stress fiber networks and demonstrated that our method is capable of distinguishing different contractile modalities (section 3.6). The manuscript has been submitted to PNAS and is also available on arXiv [85]. Mehdi Molaei developed the method and computational implementation. Steven Redford, Danielle Scheff, Patrick Oakes, and Wen-hung Chou performed experiments. Mehdi Molaei and Steven Redford carried out the analysis. Medhi Molaei, Steven Redford, Wen-hung Chou, and Margaret Gardel wrote the manuscript.

3.1 Introduction

Active systems can be found at various scales across the natural world. From flocks of birds and schools of fish [86, 87], to swarms of bacteria [88, 89] and the protein filaments inside of cells [90], a system is considered active if individual agents– birds or molecular motors– locally convert energy into mechanical work [91]. These local injections of energy produce forces, flows, and dynamic patterns on scales much larger than the active components themselves [92, 93]. While all active systems share an underlying character, the structure and dynamics

exhibited by each is a consequence of their specific mechanisms of energy injection, long range structural interactions, hydrodynamic milieu, and boundary conditions [87]. Understanding how these factors conspire to produce the emergent phenomena we observe is an important challenge not just for understanding complex natural systems but also for designing novel and potentially autonomous materials. The myriad length and time scales often present, however, make characterizing the mechanics and dynamics of active systems difficult.

When trying to gain access to length and time scales of active systems, the most easily accessible and plentiful data available are dynamic fields (e.g. velocity or intensity fields). Many methods have been developed to analyze these fields [94, 95, 96]. Correlation functions in particular have proven useful for extracting both length and time scales from velocity fields [96]. In the process, however, these methods reduce the information in complicated experimental fields to a few specific dimensions, limiting the insights we can glean. A complete picture of active dynamics would report the localized response of the system to an active perturbation. In thermally driven systems, material responses can be obtained from microrheology [97, 98, 99]. Two-point microrheology enables measurement of length and time scale dependent responses however the paucity of data necessitates spatial averaging over radial dimensions [94]. Recently, correlated displacement velocitometry was introduced which overcomes this limitation by considering the motion of many particles with respect to an averaged source [100]. This method allowed for the measurement of interfacial flow around thermally driven colloids in two dimensions. By taking into account the internal directions of a displacement field this method effectively extended correlation analysis to measure the response function of a simple fluid near thermodynamic equilibrium.

Here we extend this method to measure the response of active systems with unknown material properties far from equilibrium. We show that the idea introduced in ref. [100] can be applied to any number of fields readily obtained from experimental data. Furthermore, by considering cross correlations we measure material response not only to displacement but

other salient perturbations. We utilize this method to elucidate material and dynamical responses in a range of active materials composed of the biopolymer F-actin driven by myosin molecular motors. Specifically, in an active extensile nematic we extract the time-dependent length scales associated with vortical and shear perturbation that provide insight into turbulent flows. In a contractile active gel, we find that the ratio of these two critical length scales presage the onset of contractility. Furthermore, considering the temporal decay of these response functions allows us to distinguish viscous from viscoelastic dissipation in the nematic and the gel, respectively. Finally we show that this method can be harnessed to probe the mechanics of the actomyosin cytoskeleton in living cells. While we focused our attention here on active actomyosin materials this method should be of broad utility in the study of complex systems.

3.2 Measurement of response functions in 2D active materials

To begin, we consider a displacement field for a two dimensional active material. fig. 3.1A shows one such field from an experimental active system. As typical active materials contain a number of length and time scales, our approach will be to extract as much information as we can from this important dynamic field. To do so, we will approach correlation analysis not as conventional autocorrelation but as generalized cross correlation between some field $\boldsymbol{p}$ and the displacement field $\boldsymbol{u}$. The real trick here will be to take special notice of any directional information in $\boldsymbol{p}$. This directional information will help the correlation to represent an averaged response of $\boldsymbol{u}$ to the specific perturbation represented by $\boldsymbol{p}$.

Because $\boldsymbol{p}$ could in principle be a high rank tensor field and interpreting high ranked correlation functions is difficult (See SI), we introduce the general correlation function $\boldsymbol{\chi_p}$.

$$\boldsymbol{\chi_p}(\boldsymbol{R},\tau) = \langle p(\boldsymbol{r}_1,t)\boldsymbol{u}(\boldsymbol{r}_2,t+\tau)\delta(\boldsymbol{R}-\boldsymbol{r}'_{12})\rangle_{\boldsymbol{r}_1,\boldsymbol{r}_2,t}, \tag{3.1}$$

here p is the scalar magnitude of the field $\boldsymbol{p}$ which renders $\boldsymbol{\chi_p}$ the same rank as $\boldsymbol{u}$. $\langle\cdot\rangle_{\boldsymbol{r}_1,\boldsymbol{r}_2,t}$ denotes averaging over space and time. Since p and $\boldsymbol{u}$ are often discrete measurements, the average is computed by binning our data over a window of chosen size, which is represented by the finite width delta function δ. $\boldsymbol{R}$ is the location in a new Euclidean space with the same dimensionality as $\boldsymbol{u}$. Finally, $\boldsymbol{r}'_{12}$ is the distance vector between $\boldsymbol{p}$ and $\boldsymbol{u}$, which will be constructed in this new coordinate system to report on the location of $\boldsymbol{u}(\boldsymbol{r}_2)$ with respect to the position and heading of $\boldsymbol{p}(\boldsymbol{r}_1)$. The purpose of $\boldsymbol{r}'_{12}$ is to center the average such that each $\boldsymbol{p}(\boldsymbol{r_1})$ is located at the origin of $\boldsymbol{R}$. In practice, we will be dealing not with $\boldsymbol{\chi}$ itself but rather the normalized correlation field $\boldsymbol{U_p} = \boldsymbol{\chi_p}/\sqrt{\langle p^2\rangle}$. In tandem with the field $\boldsymbol{p}$ the choice of coordinate system in which $\boldsymbol{r}'_{12}$ is measured is a critical one and has important ramifications for how we interpret these correlations. To see why let us consider a concrete example.

We can consider the displacement-displacement auto-correlation function in this new setting; $\boldsymbol{U_u} = \boldsymbol{\chi_u}/\sqrt{u^2}$. Our objective is to understand how the displacement field responds to each specific $\boldsymbol{u}(\boldsymbol{r_1})$. This means we want to take into account not only the location $\boldsymbol{r_1}$ but also the heading of $\boldsymbol{u}(\boldsymbol{r_1})$. To do so, we set up a new coordinate system whose Y axis aligns with $\boldsymbol{u}(\boldsymbol{r_1})$. That is, we define $\boldsymbol{r'_{12}} = \boldsymbol{M}(\boldsymbol{r_2} - \boldsymbol{r_1})$, where $\boldsymbol{M} = \begin{pmatrix} \cos(\theta_1) & -\sin(\theta_1) \\ \sin(\theta_1) & \cos(\theta_1) \end{pmatrix}$ is the rotation matrix in which θ_1 is the angle between $\boldsymbol{u}(\boldsymbol{r_1})$ and the Y axis of the lab frame. By defining $\boldsymbol{r}'_{12}$ in this way, $\boldsymbol{U_u}$ reports on the correlation of the displacement field with a perturbing vector pointing along the Y axis. By normalizing by $\sqrt{\langle u^2\rangle}$ this correlation reports on the average behavior of the displacement field with respect to an impulse of defined direction and magnitude, (fig. 3.1C). Put differently, the function $\boldsymbol{U}_u$ reports on the averaged *response* of the displacement field $\boldsymbol{u}$ to a perturbation of unit magnitude along the Y axis. This procedure is closely related to what was utilized recently to measure the Stokeslet flow induced by Brownian motion of passive colloids at an interface [100]. By taking this directional information into account, the resulting response function is not radially

symmetric as one would expect from traditional auto-correlation. Rather, the resulting displacement response function is only reflectively symmetric about the Y axis (fig. 3.1C,ii). As one might expect, the response to a displacement along one axis decays at different rates for different angles with respect to that impulse. The response in the longitudinal direction $U_{u,\parallel} = U|_{X=0}$ propagates over the largest distance and in the transverse direction, $U_{u,\perp} = U|_{Y=0}$ over the shortest distance (fig. 3.1C,ii). The difference between these two length scales is mainly related to the hydrodynamic coupling of the active material to the viscous bulk fluids [101, 102, 103]. The ratio of these two length scales quantifies the ratio of the kinetic energy that is dissipated within the 2d system (active nematic in this case) and kinetic energy dissipated externally. These two spatial length scales, however, get convoluted when calculating the conventional displacement auto-correlation function $C_{\boldsymbol{u}\cdot\boldsymbol{u}} = \langle \boldsymbol{u}(\boldsymbol{r}) \cdot \boldsymbol{u}(\boldsymbol{r}+\boldsymbol{R})\rangle_r / \sqrt{\langle \boldsymbol{u}(\boldsymbol{r})\cdot\boldsymbol{u}(\boldsymbol{r})\rangle_r}$ as all perturbations $\boldsymbol{u}$ are treated identically regardless of heading. In fact, this traditional auto-correlation function is equal to the azimuthal average of the response function we consider, $C_{\boldsymbol{u}\cdot\boldsymbol{u}} = 1/2\pi \int_0^{2\pi} U_Y(\boldsymbol{R}) d\theta = (U_\perp + U_\parallel)/2$; where θ is the angle in polar coordinates. By taking into account the headings of each element of the displacement field as we construct the correlation function we are able to access important two dimensional features of flow responses. Unfortunately, while this description of the auto-correlation response contains more information than the previous version, determining a length scale from these functions still requires a model. This stems from the fact that any auto-correlation function must inherently be maximally correlated with itself at the origin. Without any universal scaling describing the decay of this correlation in active systems we are left to approximate. We will show that such ambiguity may not exist in responses to higher order perturbations.

To capture the response of the displacement field to high order modes of deformation, we explore the response of the displacement field to its own gradients, $\nabla \boldsymbol{u}$. In a linear system, we begin by decomposing the displacement gradient tensor $\partial_i u_j$ into the anisotropic symmetric

traceless strain rate tensor, $S_{ij} = (\partial_i u_j + \partial_j u_i)/2 - \partial_k u_k I_{ij}/2$, the isotropic symmetric strain rate tensor $D_{ij} = \partial_k u_k I_{ij}/2$, and the circulation tensor $\Omega_{ij} = (\partial_i u_j - \partial_j u_i)/2$. Here, $\boldsymbol{I}$ is an identity tensor with the same rank as $\partial_i u_j$. This choice of decomposition has great physical utility as in two dimensions it corresponds to separating the contributions of pure shear, normal, and vortical deformation from one another. Having performed this decomposition, we construct a family of response functions $\boldsymbol{U_S}, \boldsymbol{U_D}, \boldsymbol{U_\Omega}$ corresponding to the response of the deformation field to the different perturbations, each of which quantifies different flow structures in $\boldsymbol{u}$. We will defer the physical interpretation of these response functions in the various systems for the later sections but will focus here on the methodology for constructing each. Specifically, let us focus on the critical question of how to choose a coordinate system.

Among these tensors, $\boldsymbol{D}$ – which quantifies bulk contraction or extension – does not have a unique eigendirection and can be fully described by its first principal invariant. Therefore it can be treated as a scalar field, D. As scalar fields do not have headings, we cannot choose a meaningful angle about which to rotate. In such cases, we default to a translation of the lab frame (fig. 3.1D,i). More precisely, in the case of a scalar perturbation field we simply take $\boldsymbol{r'_{12}} = (\boldsymbol{r_2} - \boldsymbol{r_1})$. A similar situation arises with the circulation tensor $\boldsymbol{\Omega}$ in two dimensions. This tensor has only one pseudovector which is normal to the plane of observation with rotation rate equal to vorticity $\nu = \hat{\boldsymbol{e}}_z \cdot \boldsymbol{\nabla} \times \boldsymbol{u}$. As the pseudovector of $\boldsymbol{\Omega}$ provides no extra information, we will use the scalar vorticity field, ν, throughout this work and choose the simple translation of the lab frame as our coordinate system (fig. 3.1D,i). In the case of both D and ν, the resulting response function is radially symmetric which is a product of the lab frame coordinate that we have chosen (fig. 3.1D,ii). Intuitively, we expect a system's response to vortical perturbation, $\boldsymbol{U}_\nu$ or normal deformation to be radially symmetric which is the case in the measured responses (fig. 3.1D,ii).

Unlike its cousins, $\boldsymbol{S}$ is not a scalar field and thus requires more care when choosing coordinates. $\boldsymbol{S}$ possesses two eigenvectors which identify pure shear directions with eigen-

values $\pm\lambda$ indicating shear rate. To construct $\boldsymbol{\chi}_S$ in this case we setup a coordinate system similar to the case of displacement auto-correlation where the Y axis is aligned with the eigendirection corresponding to the positive eigenvalue, (fig. 3.1E,i). It is important to note here that it does not truly matter which eigenvector we choose so long as we are consistent while constructing the response function. As a convention, we have chosen the eigenvector associated with positive shear as we will eventually turn this method on an extensile system. The eigenvalue of $\boldsymbol{S}$ in this direction, λ, is used as the scalar field which normalizes the correlation. The shear response function we construct, $\boldsymbol{U_S} = \boldsymbol{\chi_S}/\sqrt{\lambda^2}$ is therefore the response function of the system to a pure extensile shear perturbation at the origin pointing outwards along the Y axis as seen in fig. 3.1E,i. Since $\boldsymbol{S}$ is a symmetric and traceless tensor, the resulting response function $\boldsymbol{U_S}$ is symmetric about both X and Y axes (fig. 3.1E,ii). This is the high rank extension of what we have seen already. Scalar fields, having no internal directions in the plane, form radially symmetric correlation functions while vector fields yield only one axis of symmetry. This response to a second rank tensor which represents bidirectional motion yields a response function that is symmetric about two separate axes.

So far we have only measured equal-time response functions. Evaluating the response after some lag time however is straightforward. Taking a perturbation field $\boldsymbol{p}(\boldsymbol{r}_1)$ at time t the delayed response function is constructed from $\boldsymbol{u}$ measured after some delay time $t+\tau$. A snapshot of the velocity field from fig. 3.1A measured at $\tau = 12\,\mathrm{s}$ is shown in fig. 3.1B. From these two displacement fields corresponding response functions $\boldsymbol{U_u}(\tau)$, $\boldsymbol{U}_\nu(\tau)$, and $\boldsymbol{U_S}(\tau)$ are computed at $\tau = 12\,\mathrm{s}$ (fig. 3.1C-E,iii). The spatiotemporal response functions as measured here provide useful information about spectral properties of the dynamics of active matter in the time domain, which has proven challenging so far to gain access to [104].

Thus far then we have focused solely on technical implementation of this approach. We have demonstrated that by taking into account internal headings of a perturbing filed, we can use the familiar language of correlation functions to construct functions that report on

the response of a displacement field to these specific perturbations. After decomposing the displacement gradient tensor into constituent parts we demonstrated how to construct similar response functions for various ranks of perturbing inputs. Finally, we have seen a simple procedure to extend this framework into the time domain. Having detailed these technical steps, we now utilize our analysis on real data. In each we will ask what information this new approach can reveal compared to previously established methods for a few well characterized active systems.

3.3 Response Functions Reveal Characteristic Length Scales in Active Nematic Turbulence

We begin by analyzing the flow structures of an active nematic liquid crystal, as their steady state dynamics are well characterized [87, 92, 105]. Here we consider an extensile nematic composed of short actin filaments driven by mysoin motors [106, 107]. Figure 3.1A and B are snapshots of the displacement field $\boldsymbol{u}$ of an active nematic measured over $\Delta t = 2\,\mathrm{s}$ at two different time points. We measure the displacement response $\boldsymbol{U_u}$ in this system and find a difference in decay length between the direction parallel and perpendicular to the averaged displacement vector (fig. 3.1C,ii). The monotonic decay of these traces preclude the extraction of an unambiguous length scale as quantifying the decay would require a model or ansatz, fig. 3.1C,ii. The non-monotonic shape of the vortical and shear responses overcome this limitation (fig. 3.1D,E iv).

The azimuthal average of the vortical response function $U_\nu(R)$, exhibits a clear peak (fig. 3.1D,iv). Since the helicity $\langle \nu(\boldsymbol{r})\boldsymbol{u}(\boldsymbol{r})\rangle_{\boldsymbol{r}}$ in a 2D nematic field is zero, U_ν starts from zero at the origin and rises to the characteristic magnitude U_ν^* at the characteristic length scale R_ν^*, before decaying at large distances due to dissipation mechanisms [104]. To put the characteristic length scale $R_\nu^* = 14.1\,\mu\mathrm{m}$ in context with established methods, we measure the distribution of vortex sizes using the standard Okubo-Weiss parameter and velocity

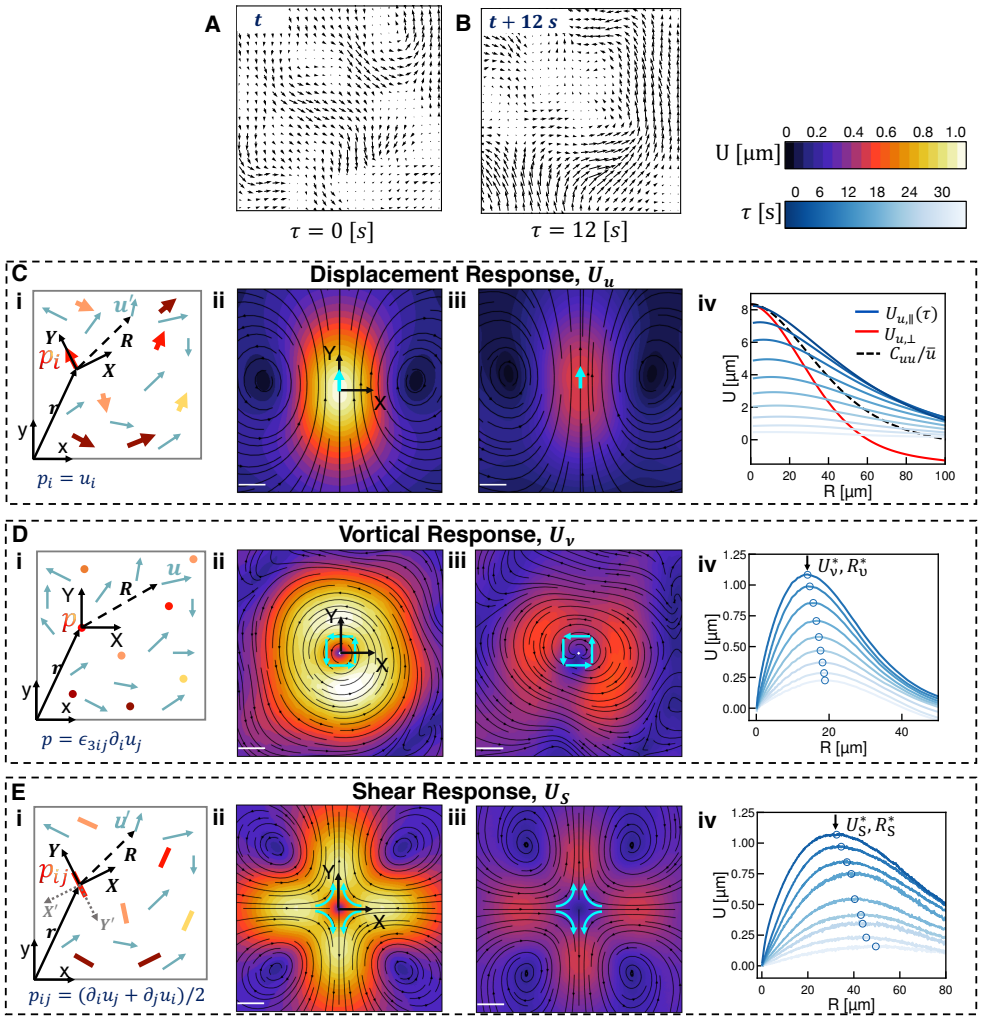

Figure 3.1: **Measuring directionally rectified correlations reveals response functions in active materials.** A,B) Displacement fields measured by optical flow from fluorescence microscope images of an active nematic liquid crystal at $t = 0s$ (A) and $t = 12s$ (B). Displacements measured over $\Delta t = 2\,\mathrm{s}$. (i) Schematic of coordinate transformation and ensemble formation for the response of the two dimensional displacement field $\boldsymbol{u}$ to various perturbation fields $\boldsymbol{p}$. $\boldsymbol{p}$ is either the displacement field itself, u (C), the vorticity field, ν (D), or the anisotropic strain rate field, $\boldsymbol{S}$ (E). (ii) Equal time two dimensional response of the displacement field in (A) to each of the respective perturbations. Ensembles are constructed such that the Y axis in (i) is the same as (ii). Streamlines indicate the direction of the resulting response function and color indicates the magnitude; scale bars are 5 μm. (iii) The $\tau = 12s$ time delayed response function. The perturbation coordinate system is set at $\tau = 0s$ and the response is measured at $\tau = 12s$. (iv) One dimensional profiles of the responses calculated at various lag times. Lighter colors indicate longer lag times. (Continued on the following page)

Figure 3.1: (Continued) C,iv) One dimensional profile is constructed by tracing along the major axis (blue). Note that the azimuthal average is simply the average of the major axis trace and the minor axis trace (red). D,iv) One dimensional profile is constructed by azimuthally averaging. Model free characteristic deformation U^* and length R^* scales at the various lag times indicated by open circles. E,iv) One dimensional profile constructed as a trace along the Y axis. The origin symmetry of the field shown is unique to divergence free systems. Note the large characteristic length scale in comparison to vortical deformation fields.

winding number [92, 108, 109] (Fig. S1). Applying this method to our distribution we find an average vortex area of $(688 \pm 9)\,\mu\text{m}^2$. This is in close agreement with the vortex area calculated from our model free vorticity length scale $\pi(R_\nu^*)^2 = 624\,\mu\text{m}^2$. Thus the vortical response function reports a critical length scale that is commensurate with the radius of an average vortex in the system.

The shear response $\boldsymbol{U_S}$ for an active nematic exhibits a high degree of reflective symmetry (fig. 3.1E,ii). In this case $\boldsymbol{U_S}$ is symmetric about not only the X and Y axes as we would expect from the response to a second order tensor, but also the diagonal $Y = X$. This symmetry arises from the incompressibility of the nematic film. Because $\boldsymbol{U_S}$ is diagonally symmetric, we consider only the one dimensional trace along the Y axis (fig. 3.1E, iv). Similar to the vortical response, this one dimensional trace rises from zero at small length scales and decays due to various dissipation mechanisms giving a critical magnitude, $U_{\boldsymbol{S}}^*$, and length scale, $R_{\boldsymbol{S}}^*$, of flow structures associated with shear perturbation. In this case, this one dimensional response trace starts from zero at the origin because inertial advection $\boldsymbol{u} \cdot \boldsymbol{\nabla u}$ at small length scales is zero. It is interesting to note that in general $R_{\boldsymbol{S}}^* > R_\nu^*$. This is because the shear deformation field $\boldsymbol{U_S}$ is coupled to pressure gradients in the system while the vortical deformation field, in the absence of inertial effects, is not [87, 110]. Vortical perturbation at the origin only propagates by the curl of force density due to elastic, flow-alignment, and active stresses and thus is dictated in large part by the systems shear rheology [103]. Because these scales are model-free and unambiguous they allow for comparisons between active nematics with different levels of activity and reveal a scaling law in nematic

dynamics (Fig. S2) [111, 112].

3.4 Critical Length Scales Anticipate the Onset of Contractility in an Active Gel

In contrast to active nematics that exhibit dynamics at steady state, the structure and dynamics of contractile active gels evolve over time (fig. 3.2 A-C,i, actin fluorescence in grey scale, myosin fluorescence in magenta, and Fig. S3) [76, 113]. The gels we consider are composed of long actin filaments driven by Myosin II motors which crosslink and buckle filaments leading to bulk contraction [113]. One interesting feature is that after the addition of myosin motors at $t = 0\,\mathrm{min}$, the gel does not contract immediately. Rather as myosin filaments settle onto the network and stresses slowly build up, the divergence of the displacement field $\langle \boldsymbol{\nabla} \cdot \boldsymbol{u} \rangle$ remains negligible for a time before rapidly decreasing as the system irreversibly contracts (fig. 3.2D, black circles). This delay has been a particular focus of studies on active gels, specifically the relation between the buildup and spectrum of internal stresses and the stability or contractility of the system [114]. To investigate this transition in detail we measure the shear $\boldsymbol{U_S}$ and normal $\boldsymbol{U}_D$ response at three representative stages of contractility where $\langle \boldsymbol{\nabla} \cdot \boldsymbol{u} \rangle$ of ~ 0, 0.01, and 0.1 (fig. 3.2D, vertical dashed lines). As we expect, the magnitude of the normal response $\boldsymbol{U}_D$ increases as contractility builds reflecting the compression of the gel (fig. 3.2A-C,iii; F).

One striking feature of the contractile gel is that the shear response in the transverse direction decays more quickly than along the major axis of contraction (fig. 3.2B,ii, comparing the X (transverse) and Y (contraction) axes). The asymmetry becomes even more pronounced for increasing divergence (fig. 3.2B-C,ii). We can think about this deviation from symmetry as the addition of an isotropic response that represents the net contraction of the system due to shear perturbations. To isolate these different modes of deformation, $\boldsymbol{U_S}$ can be separated into an isotropic and anisotropic part $\boldsymbol{U_S} = [-U_{\boldsymbol{S}R,aniso} \cos 2\theta +$

$U_{\boldsymbol{S},iso}]\hat{\boldsymbol{e}}_R + U_{\boldsymbol{S}_{\theta,aniso}} \sin 2\theta \hat{\boldsymbol{e}}_\theta$, where $\boldsymbol{U}_{\boldsymbol{S},aniso}$ gives the strain dipolar modes, and $\boldsymbol{U}_{\boldsymbol{S},iso}$ gives the compressional mode. Splitting the response in this fashion allows us to track the progression of contraction in the gel directly from the shear response. Specifically, the azimuthal average of the isotropic shear response per unit area at $R^*_{\boldsymbol{S}}$, $U_{\boldsymbol{S},iso}(R^*)/R^*_{\boldsymbol{S}}$, is equal to the average divergence, $\langle \boldsymbol{\nabla} \cdot \boldsymbol{u} \rangle$, of the displacement field (fig. 3.2D, solid black line). The isotropic shear response $\boldsymbol{U}_{\boldsymbol{S},iso}$ then, is reporting on the magnitude of contraction induced by local shear stress. Thus in this system, which is driven by the local sliding of pairs of filaments [113], this response captures the global divergence. It should be noted here the relationship between $\boldsymbol{U}_{\boldsymbol{S},iso}$ and $\boldsymbol{U}_D$. The normal response $\boldsymbol{U}_D$ measures the system's response to the contraction captured by $\boldsymbol{U}_{\boldsymbol{S},iso}$. Considering the azimuthal average of each, we find that both $U_{\boldsymbol{S},iso}$ (fig. 3.2E, dots) and U_D (fig. 3.2F, lines) increase as contractility increases. $U_{\boldsymbol{S},iso}$ decays weakly as a function of distance, reflecting the spatial dependence of local contractility (fig. 3.2E,dots). U_D exhibits a clear peak indicating a length scale over which contractility drives maximal material deformation (fig. 3.2F). A similar peak occurs in $\boldsymbol{U}_{\boldsymbol{S},aniso}$ which captures material rearrangements due to shear (fig. 3.2E, solid lines). Furthermore, as contractile flows in the material increase, the energy scale and extent of this local shear response – both R^* and U^* – grow monotonically (Fig. S4). Interestingly, after these peaks none of these responses decay fully to zero (fig. 3.2E,F). As noted in the nematic, at steady state the far field response decays to zero. The lack of such decay in the far field ($R > R^*$) indicates that the contractile gel dynamics are not at steady state.

In addition to specifically enumerating these mesoscale deformations due to contractile stress, the resolution of our measurement reveals features that seem to presage the onset of contractility. Recall that the length scale associated with shear response $R^*_{\boldsymbol{S}}$ is typically larger than the length scale associated with the vortical response $R^*_{\boldsymbol{S}}$ (fig. 3.1D-E,iii,Fig. S4-5). Interestingly, the ratio of these length scales $R^*_\nu/R^*_{\boldsymbol{S}}$ increases over time reaching its maximal value of ~ 0.9 just prior to the onset of $\langle \boldsymbol{\nabla} \cdot \boldsymbol{u} \rangle < 0$ (fig. 3.2D, open blue squares).

Prior work has shown in strongly driven F-actin networks that the rate of energy dissipation and filament bending energy increases until the onset of contractility [114]. In this light, we surmise that the increase of $R^*_\nu/R^*_{\boldsymbol{S}}$ reflects the decoupling of the pressure and shear deformation fields via filament bending until bulk contraction once again suppresses these fluctuations.

3.5 Temporal Decorrelation of Responses Enumerate Modes of Dissipation Across Length Scales

We next investigated dissipation across different length scales. Recall that in the active nematic, all the curves of $U_{\boldsymbol{S}}(\tau)$ as a function of lag time (fig. 3.1E,iv fig. 3.3A, red curve), shared a similar form. Namely, $U^*_{\boldsymbol{S}}$ decreases and $R^*_{\boldsymbol{S}}$ increases as τ grows, until at longer lag times the response is negligible (fig. 3.3A, red curves; lighter colors indicate longer lag times). This steady decorrelation in time is characteristic of viscous dissipation. In contrast to this monotonic decay, $U^*_{\boldsymbol{S}}$ in the contractile gel becomes *negative* at intermediate lag times before approaching zero (fig. 3.3A, blue curves). This anticorrelated signal is a strong signature of elasticity with the reduced peak height reflecting contributions from viscous dissipation. This contractile gel then bears a strong signature of viscoelasticity dissipation; biochemical modifications to the contractile gel that enhance viscous relaxation abrogate this response (Fig. S5).

We quantify the length-scale-dependent dissipation in the active nematic by considering the normalized relaxation of $U_{\boldsymbol{S}}(\tau)$ at several distances R with respect to the peak $R^*_{\boldsymbol{S}}$ (fig. 3.3B). Each relaxation is fit to a scaled exponential function, $U(\tau) = \exp(-[\tau/\tau_r(R)]^{\gamma(R)})$; where $\tau_r(R)$ is the size dependent decay time and $\gamma(R)$ is the size dependent scaling factor. We define the decay time from scale-dependent response measurements, $\tau_r(q = 2\pi/R)$ as the time that the normalized response profile (fig. 3.3B) relaxes to the inverse of the Euler number, ~ 0.368. For $R = 0$ we find that the scaling factor $\gamma = 1$ consistent with diffusive

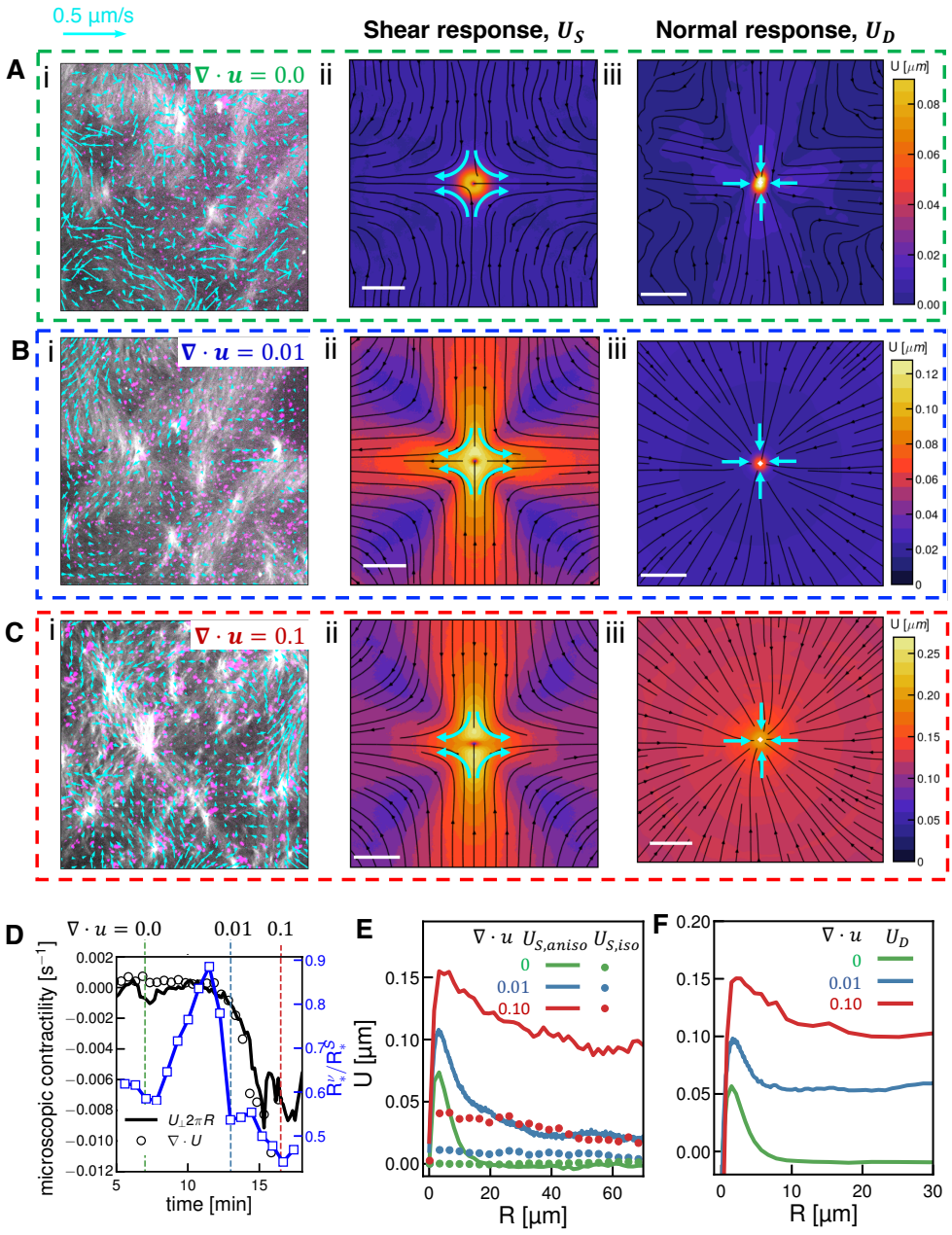

Figure 3.2: **Response functions identify key dynamic consequences of contraction in *in vitro* actomyosin networks.** i) Micrographs of fluorescent actin (gray) and myosin (magenta) overlaid with scaled velocity vectors (blue) for the active gel at various divergences (A-C). Colors correspond to divergences indicated in (D), each box is $100 \times 100 \mu m^2$ of the field of view. ii) Equal time shear response for the velocity fields in (i). iii) Normal (compression) response for the velocity fields in (i). Streamlines indicate the direction of the resulting correlation field and color indicates the magnitude; scale bars are 5 μm. (Continued on next page)

Figure 3.2: (Continued) D) Divergence of the velocity field (black circles) as a function of time for a contractile active gel. The azimuthal average of the isotropic shear response per unit area at $R = R^*_{\boldsymbol{S}}$, $U_{\boldsymbol{S},iso}(R^*_{\boldsymbol{S}})/R^*_{\boldsymbol{S}}$ (solid black line) agrees with the calculated divergence. The green, blue, and red dashed lines indicate the points taken as characteristic of the gel before contraction, at the onset of contraction, and deep in the contractile regime. Numerical labels indicate the value of divergence at these points. Ratio of characteristic length scales $R^*_\nu/R^*_{\boldsymbol{S}}$ as a function of time (solid blue line, open blue squares). Time axis indicates elapsed time after the addition of myosin motors. (E) One dimensional traces of the symmetric ($U_{\boldsymbol{S},iso}$, solid lines), and anisotropic ($U_{\boldsymbol{S},aniso}$, dotted line) decomposition of the shear response function in (ii) as a function of distance R. (F) One dimensional traces of the normal (compressional) response in (iii) as a function of distance R.

relaxation of the shear response (fig. 3.3B, red curve). At large scales, $R = 2R^*_{\boldsymbol{S}}$, the relaxation profile is a stretched exponential $\gamma = 2$, diagnostic of ballistic type motion [115, 116] (fig. 3.3B, green). At intermediate scales, $R^*_{\boldsymbol{S}}/2 \leq R \leq R^*_{\boldsymbol{S}}$, γ transitions smoothly between these extremes, indicating the transition between stochastic and flow dominated dissipation in the active nematic (fig. 3.3B, blue and black).

To put these results in context, we compare our results to measurements from the established technique of differential dynamic microscopy (DDM) [95, 116, 117]. We calculate the dynamic structure function $D(q, \tau)$ from time lapse images of the active nematic considered above over a range of wave-numbers q, from $0.1\,\mu\text{m}^{-1}$ to $1\,\mu\text{m}^{-1}$ and lag times $1 < \tau < 200\,\text{s}$ (fig. 3.3C, color indicates q). We define a characteristic timescale $\tau_r(q)$ as the lag time when $D(q, \tau)$ reaches 63.2% of $D(q, \infty)$; where $D(q, \infty)$ is the plateau value at long lag time. For short lag times, $\tau < \tau_r(q)$, $D(q, \tau)$ follows a power law, $\tau^{\gamma_{DDM}}$ reflecting high frequency relaxation. Consistent with our response function analysis, we find $\gamma_{DDM} = 2$ for $q < 0.1\,\mu\text{m}^{-1}$, and $\gamma_{DDM} = 1$ for $q > 1\,\mu\text{m}^{-1}$ indicating ballistic type motion at long length scales and diffusive type motion at short length scales (fig. 3.3C). Similar to scale dependent response functions, we find a smooth transition between these behaviors in intermediate regimes (fig. 3.3C).

While both methods agree on qualitative scaling at extreme scales we find that the critical time scales $\tau_r(q)$ extracted from DDM are uniformly shorter than relaxation times found

using our response analysis (fig. 3.3D, black squares DDM, colored squares response analysis). Furthermore, this is not the product of a mere baseline shift but rather of markedly different scaling (fig. 3.3D). For large q the relaxation time measured by DDM scales as $\tau \sim 1/q$. Over the same range U_ν becomes q independent (fig. 3.3D, open green squares). This disconnect can be understood as DDM relaxation necessarily combines advection of material structure and dynamic relaxation processes. As such DDM correlations relax quickly. In contrast, U_ν stops scaling below the agent size in the system – $\sim 1\,\mu$m here (fig. 3.3D, green) – while τ_r from shear and vortical responses scale weakly with wave number in small scales, $\tau_r \sim q^{-0.25}$ (fig. 3.3D, blue and red). This slower scaling of $\tau_r(q)$ reflects the relaxation of only one source of strain. While DDM combines many modes of relaxation, response functions allow us to tease apart relaxation from many sources of stress independently.

3.6 Response functions differentiate modes of cellular contractility

We now explore whether our method can distinguish different modes of actomyosin contractility in living cells. In adherent cells, the actomyosin cytoskeleton is organized into networks and bundles with highly stereotyped architecture and dynamics [35]. Transverse arcs are actomyosin bundles formed near the cell periphery and oriented parallel to the cell edge. Myosin activity continually drives the coalescence and contraction of transverse arcs resulting in their in continual inward motion, a dynamic process known as retrograde flow [35, 37]. In contrast, ventral stress fibers are highly stable actomyosin bundles anchored on each end by focal adhesions [35, 37]. While both architectures can coexist, broadly circular U2OS osteosarcoma cells and elongated NIH 3T3 fibroblast cells predominantly display transverse arcs and ventral stress fibers, respectively (fig. 3.4A,B). In each cell type, time-lapse imaging of fluorescently labeled myosin is used to obtain displacement fields of the actomyosin dynamics (fig. 3.4A,B, stress fibers grey, flow field blue arrows).

The shear response $\boldsymbol{U_S}$ is then calculated for different lag times (fig. 3.4ii) and as in

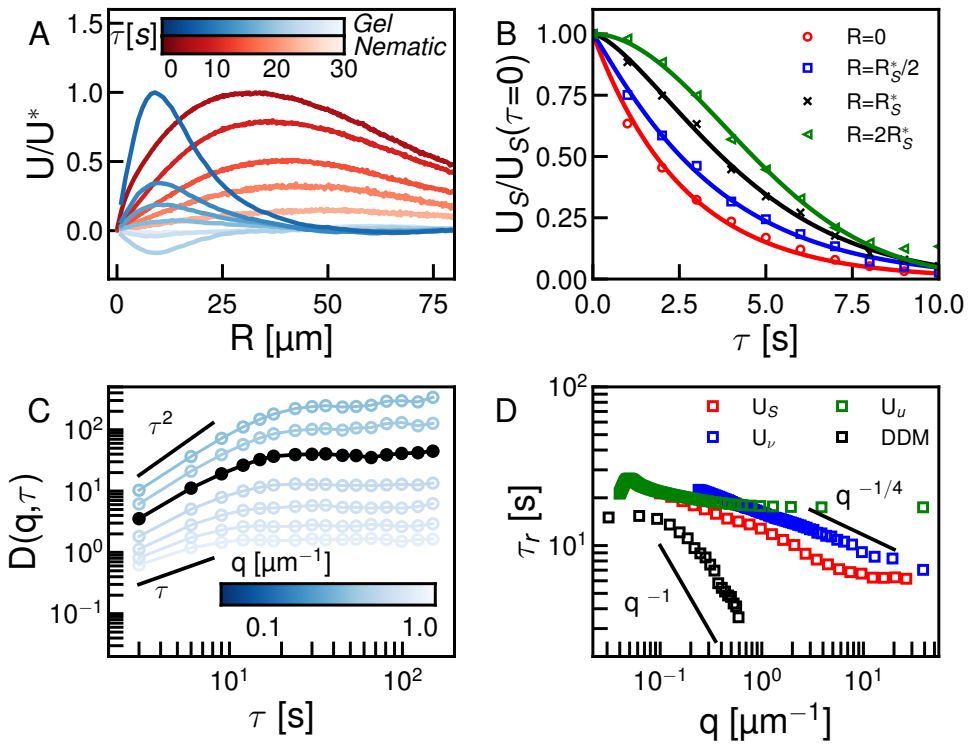

Figure 3.3: **Temporal dependence of correlated displacement field reveals characteristic time scales of active materials.** A) Normalized one dimensional shear response, $U_{\boldsymbol{S}}$, for an active nematic (blue) and active gel (red) measured at different delay time τ (see scale bar). B) Normalized shear response as a function of delay time τ measured at different spatial scales with respect to the critical length scale R^*. Experimental data is indicated with symbols solid lines are fit of the data to a stretched exponential. C) Dynamic structure function $D(q,\tau)$ at different wave number q (see scale). $D(q = 2\pi/R^*, \tau)$ is plotted in black. τ^2 and τ scaling are indicated. D) Characteristic time scales τ_r as a function of wave number q for DDM (black) and displacement (U_u, green), shear (U_S, red), or vortical (U_ν, blue) response.

fig. 3.2E is split into one dimensional traces of the anisotropic $U_{\boldsymbol{S},ansio}$ (fig. 3.4iii) and isotropic $U_{\boldsymbol{S},iso}$ (fig. 3.4iv) components. The most dramatic difference between these architectures is in the isotropic shear response. In transverse arcs this response increases linearly as a function of distance and does not diminish over time, reflecting long range and coherent retrograde flow (fig. 3.4A,ii,iv). The isotropic shear response is entirely absent in ventral stress fibers reflecting a lack of contractile dynamics (fig. 3.4B,ii,iv). In contrast to the differences in the isotropic shear response, in both cases the anisotropic shear response

at $\tau = 0\,\mathrm{s}$ is peaked around $1\,\mu\mathrm{m}$ (fig. 3.4A-B,iii red). This reflects a similar length scale of maximal shear distortion. By $\tau = 10\,\mathrm{s}$ the anisotropic shear response in transverse arcs decays completely (fig. 3.4A,iii blue). This indicates that shear deformations in transverse arcs decorrelate faster than the time scale τ. In contrast, in ventral stress fibers $U_{\boldsymbol{S},ansio}$ persists at $\tau = 10\,\mathrm{s}$ (fig. 3.4B,iii blue) reflecting longer lived shear distortions. The disparity in anisotropic shear response at later lag time reveals differences in local dissipation of shear stress arising from differences in boundary conditions and local mechanical properties.

Both ventral stress fibers and transverse arcs reflect steady state dynamics common in adherent cells. Perturbations around these steady states can be queried via recently developed optogenetic techniques. Regional activation of RhoA in NIH 3T3 cells drives increased local actomyosin contractility and induces flow in adjacent ventral stress fibers [118]. Using this previously published data, we measure the shear response of ventral stress fibers prior to (fig. 3.4B) and during (fig. 3.4C) regional RhoA activation in the orange box indicated in fig. 3.4C,i. Activation induces a shear response qualitatively similar to transverse arcs but with some important distinctions. The most notable similarity is that upon optogenetic activation, ventral stress fibers exhibit a linearly increasing isotropic shear response that is consistent over $\tau = 10\,\mathrm{s}$ but with a decreased magnitude (fig. 3.4C,iv). This underscores that a spatial gradient of contractile stress is sufficient to induce long range coherent flows in ventral stress fibers (fig. 3.4C,iv). Interestingly, the anisotropic shear response at short scales of ventral stress fibers with and without regional activation are qualitatively similar (fig. 3.4A-C,iii). In longer length scales, however, while the anisotropic response decays to 0 in the case without regional activation, the regional activation induces a far field response that does not fully decay reflecting the departure of the system from steady state dynamics (fig. 3.4A-C,iii). This deviation from steady state is similar to what was observed in the case of the active gel as divergence increased (fig. 3.2E, solid lines). The short and long range behavior of $U_{\boldsymbol{S},ansio}$ over lag times allow us to discern local mechanical

properties and degree of mechanical homeostasis in cellular actomyosin architectures.

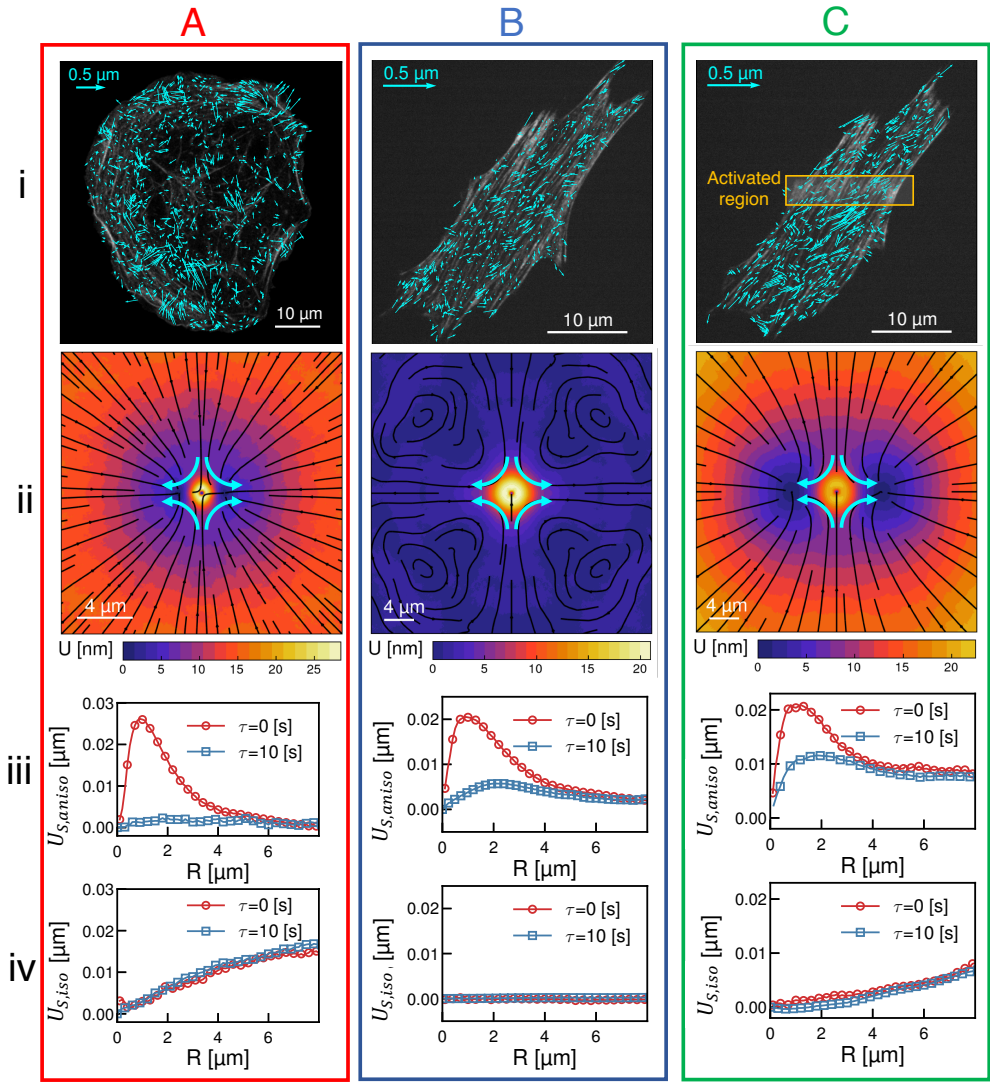

Figure 3.4: **Utilizing response functions to differentiate mechanical response of the actomyosin cytoskeleton in living cells.** (i) Micrographs of the actin fibers (grey) overlaid with myosin displacement vectors (blue) for A) transverse arcs (in a U2OS cell), B) ventral stress fibers (in an NIH 3T3), and C) regional stimulated ventral stress fibers (NIH 3T3). The orange box in (C,i) indicates the region of optogenetic activation. (ii) Shear response $\boldsymbol{U_S}$ for the displacement fields shown in (i). Streamlines indicate the direction of the response and color indicates the magnitude (see color bars). (iii, iv) One dimensional traces of the anisotropic, $\boldsymbol{U_S}_{,aniso}$ (iii), and isotropic $\boldsymbol{U_S}_{,iso}$ (iv), parts of the shear response shown in (ii) measured at lag times of $\tau = 0\,\mathrm{s}$ (red) and $\tau = 10\,\mathrm{s}$ (blue).

3.7 Conclusions

Here we have introduced a method that extends correlation analysis to probe the full response function of active systems. Traditional correlation analysis takes into account only the position of each element of the field over which the correlation is measured, averaging over field elements that may point in different direction to produce radially symmetric correlation functions. Here we overcome this inherent dimensionality reduction by constructing correlations in which we align the correlation average with each field element in turn. By aligning our correlations, we take into account the response of the field in multiple dimensions and effectively measure a material response function from data. While we focused here on the response of a displacement field u to some derivative of itself, this method can be applied more generally. In fact, we can apply the same method to measure the response of any tensor field $\boldsymbol{q}$ to a meaningful perturbative field $\boldsymbol{p}$. We can thus extend the basic framework presented here to gain insights into other many body systems with complex dynamics such as high order quantum systems.

To demonstrate the utility of this technique we compared the response of the displacement field in active actomyosin materials to previously established methods. We found that the critical length scale of the vorticity response in an active nematic, R^*_ν, is equal to the average vortex radius measured with traditional analyses [92]. We decomposed the shear response of an active gel into anisotropic and isotropic parts and found that the isotropic part captured the same contractions as the divergence of the velocity field [113]. Furthermore, our method enumerated a transition from diffusive like relaxation at small scales to ballistic like relaxation at large length scales in agreement with previous analysis [117]. In addition to these expected results we also found that the ratio of vortical to shear length scales presaged the onset of contractility in active gels. This provides a window into stress buildup and propagation and how it relates to the onset of compressibility in contractile gels. The temporal relaxation of shear responses allowed us to capture viscoelastic relaxation in

multiple materials. This enables future work to address how the peculiarities of local driving affect long range dissipation in active system. Finally, we also demonstrated the utility of this method to measure material properties of the actomyosin cortex in vivo. This represents a powerful new tool to query cell mechanics.

The specific measurements presented in this work are in many ways simply the lowest hanging fruit. A great deal of promise remains to be unlocked by combining the analysis presented here with specific experimental perturbations. By measuring response functions over a range of conditions one could calibrate the method and allow for a truly quantitative understanding of complex systems. In nematics alone one could imagine using such a procedure to detail the effect of substrate coupling, filament length, or even active agent composition on mechanics and dynamics. In cells, one could imagine genetically perturbing an actin accessory protein and specifically understanding how the mechanics of the network respond to that perturbation. Because the method isn't based on any specific physical model we can apply it to these systems and many more, including those with unknown mechanics. As such, we envision this method being of great use from dynamic systems to cell biology.

3.8 Methods

3.8.1 Active nematics and gel preparation

Experiments were performed as described previously [107, 113]. Briefly, 2 µm actin 10% labelled with tetramethylrhodamine-6-maleimide (TMR) was polymerized in F-buffer [10 mM imidazole, 1 mM MgCl2, 50 mM KCl, 0.2 mM egtazic acid (EGTA), pH 7.5] in the presence of 1mM (gel) or 100 µM (nematic) ATP. To minimize photobleaching, an oxygen scavenging system (4.5 mg/mL glucose, 2.7 mg/mL glucose oxidase(cat#345486, Calbiochem, Billerica, MA), 17000 units/mL catalase (cat #02071, Sigma, St. Louis, MO) and 0.5 vol. % β-mercaptaethanol is added to the actin mixture. 0.3% w% 400 cP methylcellulose is added

to this mixture to crowd actin filaments to the bottom of the sample volume. Nematic samples also included 30nM f-actin capping protein to limit filament growth while gels were uncapped. Nematic samples were driven by 100nM synthetic tetrameric motors as described in [119], while gels were driven by 50nM rabbit skeletal muscle Myosin II [113].

The sample was imaged on an Eclipse-Ti inverted microscope (Nikon, Melville, NY) in confocal mode utilizing a spinning disk (CSU-X, Yokagawa Electric, Musashino, Tokyo, Japan) and a CMOS camera (Zyla-4.2 USB 3; Andor, Belfast, UK). Nematic experiments were imaged collecting one frame every 2 seconds, while gels were imaged one frame every 5 seconds. Gel data in figure 3A is from [113].

3.8.2 Flow field measurement

In nematics velocity fields were calculated using the method of optical flow detailed in [120] using the Matlab code available at (https:// ps.is.mpg.de/code/secrets-of-optical-flow-code-for-various-methods) and the 'classic+nl-fast' method. These predictions were processed into proper units in Matlab. Velocity fields in cells were determined using Quantitative Fluorescence Speckle Microscopy, QFSM [121, 122].

3.8.3 Response function measurement

The code utilized in this manuscript (and sample data) are all found at https://github.com/Gardel-lab/ResponseFunction.git. In brief, gradients of the velocity fields $\boldsymbol{\nabla u}$ are calculated using localized polynomial fitting and finite element method for the fields measured by the optical flow and QFSM respectively. The eigenvalues, λ, of the strain rate tensor, $\boldsymbol{S}_{ij}$ which is symmetric part of the $\boldsymbol{\nabla u}$, is calculated by solving the characteristic equation $|\boldsymbol{S} - \lambda \boldsymbol{I}| = 0$, and eigendirections are obtained by plugging λ in the systems of equation $\boldsymbol{S} - \lambda \boldsymbol{I} = 0$ where $\boldsymbol{I}$ is the identity tensor. For the active nematic the eigendirection associated with the positive eigenvalue and for active gel and cell data the eigendirection associated with the negative

eigenvalue are chosen as direction to setup the coordinate system for ensemble averaging as described in [100]. The data measured close to the edge of the field of view is discarded to prevent error from optical flow measurement to propagate to the measured response functions. $\boldsymbol{\nabla u}$ and its decomposed components, $\boldsymbol{S}$, $\boldsymbol{\Omega}$, and $\boldsymbol{D}$ are measured over grid points with spacing large enough to prevent oversampling the data. The correlation length of these components in different systems are used to select the spacing; for example, we chose the distance where the normalized auto-correlation functions of vorticity or strain rate tensor drops to 0.5. In general, in the chaotic and noisy system the grid spacing should be smaller than grid spacing in highly coherent systems.

3.8.4 Cell culture

U2OS cells with NMIIA endogenously tagged with eGFP is a generous gift from Dr. Jordan Beach (Loyola University Chicago). U2OS cells were cultured in McCoy's 5A Medium (Sigma-Aldrich) supplemented with 10% FBS (Corning) and 2 mM L-glutamine (Invitrogen). NIH 3T3 (ATCC) were cultured in DMEM (Mediatech) supplemented with 10% FBS (Corning) and 2 mM L-glutamine (Invitrogen). Myosin was visualized by transfecting an mApple-RLC (gift of Mike Davidson, University of Florida) plasmid.

3.8.5 Microscopy and live cell imaging

For the imaging of myosin dynamics in U2OS cells, Airyscan imaging was performed on a Zeiss LSM 980 microscope equipped with the Airyscan 2 detector. Images were acquired using the MPLX SR-4X mode and processed by Zen Blue 3.0 software using the Airyscan processing feature with default settings. During live cell imaging, cells were mounted on an imaging chamber (Chamlide) and maintained at 37 °C. For live cell imaging, cell medium was replaced with Dulbecco's Modified Eagle Medium (DMEM) without phenol red (Corning) supplemented with 10% FBS, 2 mM L-glutamine, 1% penicillin-streptomycin, 10 mM HEPES

and 30 µL/mL Oxyrase (Oxyrase Inc.).

As decribed in [118], the NIH 3T3 cell was imaged on an inverted Nikon Ti-E microscope (Nikon, Melville, NY) with a Yokogawa CSU-X confocal scanhead (Yokogawa Electric, Tokyo, Japan) and laser merge module containing 491, 561 and 642 nm laser lines (Spectral Applied Research, Ontario, Canada). Images were collected on Zyla 4.2 sCMOS Camera (Andor, Belfast, UK). Local recruitment using the optogenetic probe [118] was performed using a 405 nm laser coupled to a Mosaic digital micromirror device (Andor). Images were collected using a 60X 1.49 NA ApoTIRF oil immersion objective (Nikon). All hardware was controlled using the MetaMorph Automation and Image Analysis Software (Molecular Devices, Sunnyvale, CA).

CHAPTER 4

REGULATION OF MYOSIN CLUSTER DYNAMICS

4.0 Preamble

This chapter documents two preliminary projects conducted early on during my Ph.D. The two projects focus on understanding factors that regulate myosin cluster dynamics. Section 4.1 investigates the nature and regulation of myosin turnover dynamics. Section 4.2 investigates whether F-actin regulates NMII assembly. The conclusions made in this chapter are based on preliminary results and have not been published. While more follow-up work is required, the author believes that the preliminary investigation will serve as a primer for future research and that future research may benefit from this documentation.

4.1 Turnover Dynamics of Myosin Clusters

4.1.1 Introduction

As we have characterized in Chapter 2, myosin clusters on stress fibers constantly undergo rapid dynamics in cells. Not only do they undergo retrograde flow dynamics, assembly, and disassembly, FRAP experiments also show that the constituent myosin molecules in each myosin cluster turn over in the scale of a couple minutes. In contrast, stress fibers, which are built of myosin clusters, are stable structures that persist over minutes to hours to sustain force production. While it seems counterintuitive that the rapid turnover of myosin clusters can build stable force-generating structures, these myosin clusters are in a dynamic steady state such that their turnover serves as a recycling mechanism to provide building blocks to rapidly build new myosin structures as needed. It is therefore important to understand how the turnover of myosin clusters is regulated.

Previous studies on myosin turnover found that myosin turnover rate is controlled by the

same regulatory factors of NMII filament assembly. When NMII assembly is disrupted, such as by reducing RLC phosphorylation ([123]) or deleting the assembly-competent domain on the NMII coiled-coil tail ([57, 123]), NMII turnover becomes faster. This has been attributed to the increase in diffusing NMII monomers that can't bind to F-actin. The turnover rate has also been shown to depend on the NMII isoform: NMIIB is more stable and turns over slower than NMIIA, which has been attributed to the difference in their coiled-coil tails ([124]). This has been suggested to set the localization of the two isoforms in cells ([56, 124]). Recently, mechanical tension has been suggested to play a role in NMII turnover due to the catch-bond nature of myosin motor head ([24, 27]). In cells, there is evidence that actomyosin structures that bear more tension has a slower exchange rate ([125]). Since all these factors control both NMII assembly and NMII turnover, NMII turnover has been suggested to reflect the stability of NMII filaments.

Nonetheless, we demonstrated in Chapter 2 that myosin filaments assemble into clusters in cells. This opens up the possibility that NMII turnover can occur not just by single molecule but by single filaments. With our ability to characterize individual myosin clusters on stress fibers, we aim to investigate how myosin clusters turn over and their regulation.

4.1.2 Preliminary Results

As in Chapter 2, we visualized myosin clusters and their turnover by endogenously labeling non-muscle myosin IIA (NMIIA) using a CRISPR knock-in approach. We chose to focus on non-muscle myosin IIA due to its proposed role in force generation. In contrast to Chapter 2, we labeled NMIIA at the N-terminal head domain. Since NMIIA molecules self-assemble into a bipolar filament with the head domains at both ends of the filament, a myosin filament will appear as a pair of puncta that are ∼300 nm apart under Airyscan super-resolution imaging (fig. 4.1A). Our imaging conditions are not sufficient for single molecule imaging, so again every pair of myosin puncta represent more than one myosin filament.

In control cells, we see that while myosin clusters are stable structures, their constituents are exchanging constantly. To study myosin turnover, we conducted fluorescence recovery after photobleaching (FRAP) experiments (fig. 4.1B). The recovery half time is about 2 minutes with a mobile fraction of 80% (fig. 4.1C-E). The FRAP time scales are consistent with previous reports. Fluorescence recovery of myosin cluster intensity occurs at the level of single myosin clusters, not by assembly of new structures or transport of new structures into the photobleached region (fig. 4.1F). This indicates that our FRAP recovery reports on the myosin turnover within each myosin cluster.

To understand how myosin turns over within each myosin cluster, we look at FRAP recovery of individual myosin clusters by making a kymograph (fig. 4.1F). On each kymograph, we see band-like patterns that persist over more than 8 minutes. The bands represent the head domains of each myosin cluster, so their intensities can be used to monitor the FRAP recovery of each myosin cluster. The intensity of each myosin cluster recovers similarly as the whole photobleached region while also exhibiting continuous fluctuation (fig. 4.1G). This indicates that the turnover rate of each myosin cluster is similar but with some nuanced differences, as indicated by the fluctuations. Since we do not have single molecule sensitivity, we can't say for sure how many fluorescent molecules are recovering from photobleaching. Whether this is just random fluctuation or reflects meaningful regulation by some factors would require more careful investigation.

Since previous literature suggests that myosin turnover depends on myosin assembly dynamics, we see how myosin phosphorylation affects myosin cluster turnover. First, we inhibit myosin phosphorylation by inhibiting Rho-kinase (ROCK) with the ROCK inhibitor Y-27632. The inhibitor is used at a sub-saturating concentration (5 μM) such that stress fibers are not completely disassembled (fig. 4.2A). Even at this sub-saturating concentration, we see a dramatic increase in the FRAP recovery dynamics under ROCK inhibition (fig. 4.2A-B). The recovery half time decreased dramatically (fig. 4.2C) while the mobile

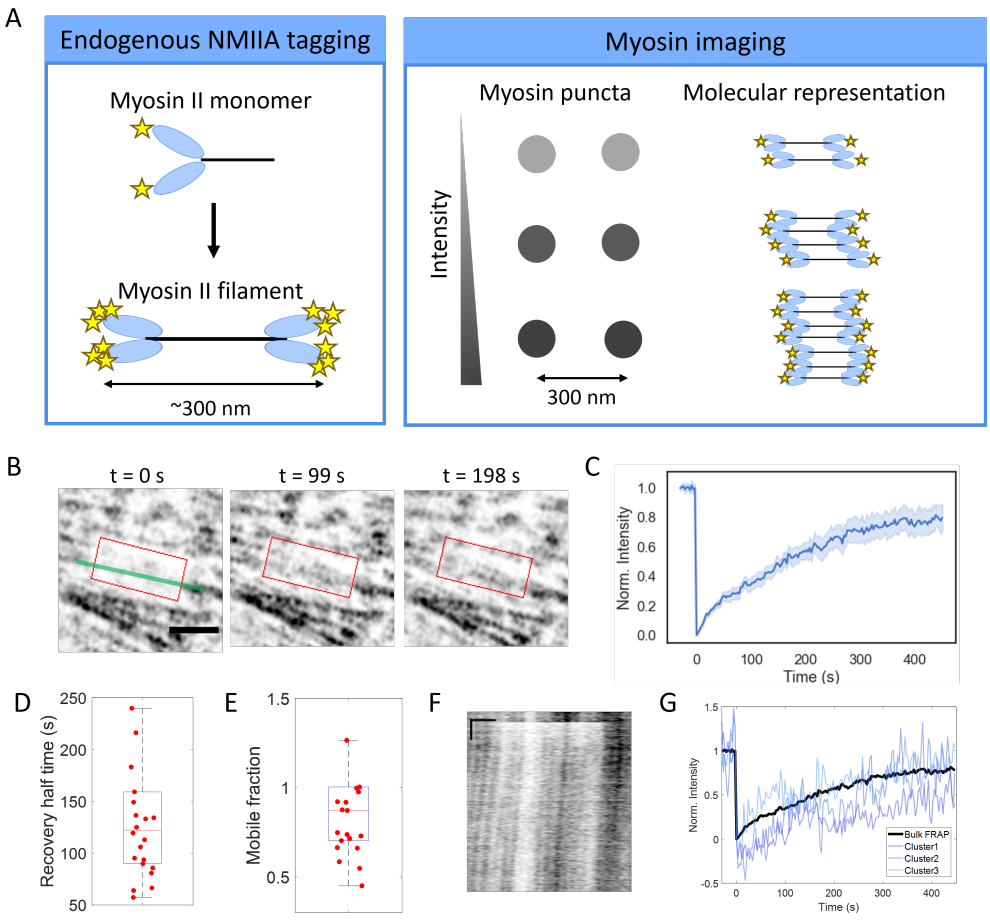

Figure 4.1: **Myosin turns over within individual myosin clusters.** (A) Schematics of the experimental setup. NMIIA is endogenously tagged at the N-terminal head domain. When imaged under super-resolution microscopy, the two heads appear as a pair of fluorescent puncta. (B) Snapshots of the FRAP experiment. Red box indicates the photobleached region. Time indicates seconds after photobleaching. Images are inverted. Scale bar is 10 µm. (C) FRAP recovery curve. (D) Recovery half times. (E) Mobile fraction. Calculated from 22 photobleached regions in 7 cells. (F) Kymograph of the photobleached region, along the green line in (B). Horizontal scale indicates 1 µm and vertical scale indicates 1 minute. (G) FRAP recovery curve of individual myosin clusters versus the recovery of the whole photobleached region.

fraction remained similar (fig. 4.2D).

The FRAP recovery time scale under ROCK inhibition agrees with previous studies (Sandquist and Means), which argued that the increase in exchange dynamics is the result of an increased pool of unassembled myosin monomers that are diffusing around the cytoplasm.

Nonetheless, the FRAP recovery of myosin clusters exhibit signatures of reaction-dominant FRAP recovery instead of diffusion-dominant recovery. Again, turnover of individual myosin clusters can be assessed by the kymograph of the photobleached region. If FRAP recovery is caused by the recovery of diffusing myosin monomers, we would expect FRAP recovery rates to be faster on the periphery of the photobleached region. Instead, we see homogeneous FRAP recovery rates throughout the photobleached region (fig. 4.2A). This indicates FRAP recovery to be dominated by the exchange of myosin molecules on each myosin clusters. Therefore, ROCK inhibition affects the reaction kinetics of myosin association/dissociation to myosin clusters.

On the other hand, we increased myosin phosphorylation by activating the GTPase RhoA with the Rho activator CN03. We see a dramatic difference in stress fiber morphology as more ventral stress fibers appeared (fig. 4.2A). Under RhoA activation, FRAP recovery kinetics became slower, with slightly longer recovery half times and smaller mobile fraction (fig. 4.2A-C). The effects may be minor because RLC phosphorylation levels are already high in the control cells. This suggests that myosin exchange is slower and fewer myosin is exchanging.

Both ROCK inhibition and RhoA activation changed not only myosin filament assembly but also the tension on stress fibers. Since recent literature suggested myosin turnover can be regulated by mechanical tension, we want to decouple the two factors. To this end, we reduced tension on stress fibers without directly affecting myosin filament assembly by treating cells with para-nitro-blebbistatin (pnBB), a photostable form of blebbistatin ([126]). pnBB was used at 5 µM, a sub-saturating concentration such that stress fibers don't completely disassemble (fig. 4.3A). We see FRAP recovery dynamics between control and pnBB-treated cells are similar (fig. 4.3A-C), with similar recovery half times and mobile fractions. This is consistent with recent reports that NMIIA turnover aren't be affected by mechanical tension due to its motor properties ([24, 58]). Since we didn't measure mechanical

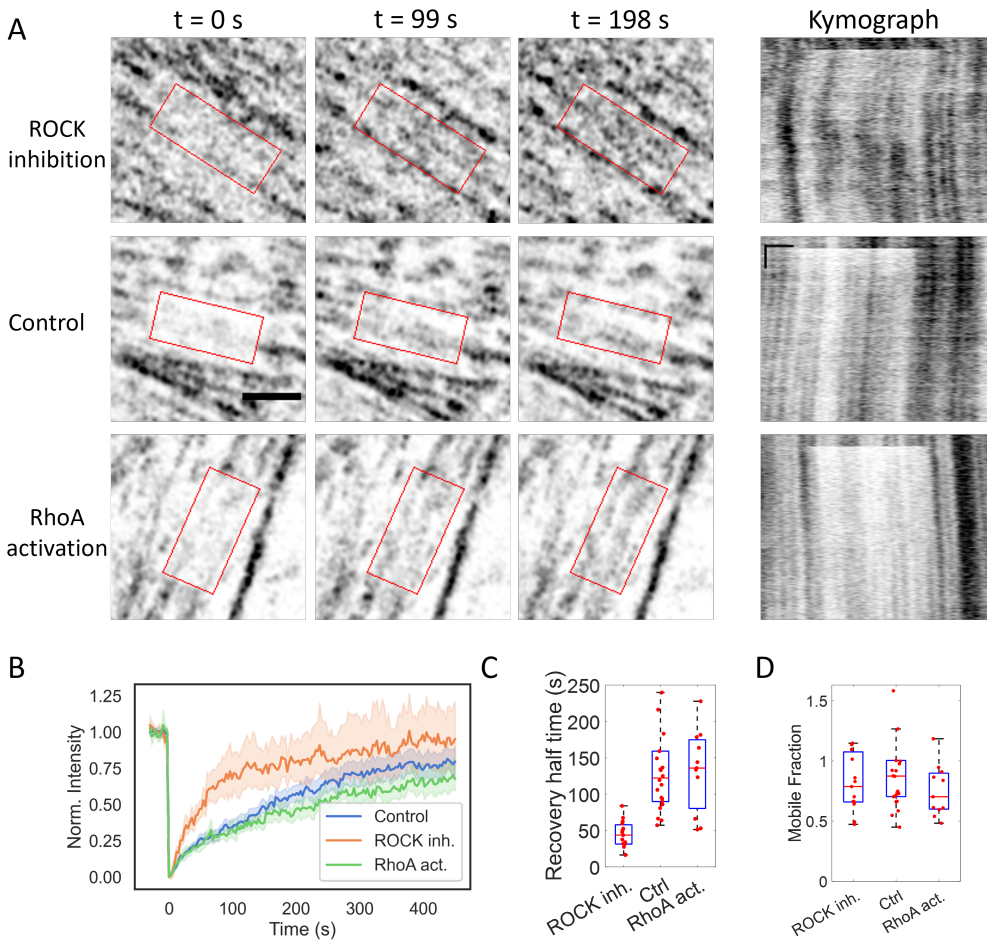

Figure 4.2: **Rho/ROCK controls myosin turnover.** (A) Snapshots of the FRAP experiment and kymograph along the photobleached region. Red box indicates the photobleached region. Time indicates seconds after photobleaching. Images are inverted. Scale bar is 10 µm. For the kymograph, the horizontal scale indicates 1 µm and vertical scale indicates 1 minute. (B) FRAP recovery curves of control, ROCK-inhibited and RhoA-activated cells. (C) Recovery half time extracted from each photobleached region. (D) Mobile fraction. Control conditions were calculated from 22 photobleached regions in 7 cells. ROCK inhibition conditions were calculated from 15 photobleached regions in 7 cells. RhoA activation conditions were calculated from 11 photobleached regions in 3 cells.

tension on stress fibers, we don't know for sure that tension is reduced at this concentration.

We need to make sure that tension is actually affected.

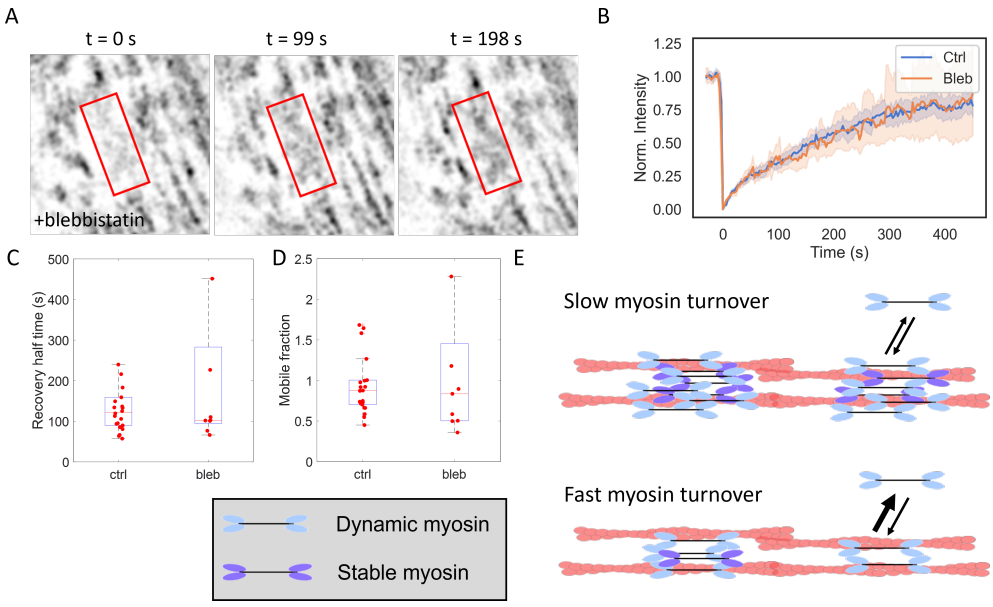

Figure 4.3: **Effects of mechanical tension on myosin turnover and myosin turnover schematics.** (A) Snapshots of the FRAP experiment. Red box indicates the photobleached region. Time indicates seconds after photobleaching. Images are inverted. (B) FRAP recovery curves of controland blebbistatin-treated cells. (C) Recovery half time extracted from each photobleached region. (D) Mobile fraction. Control conditions were calculated from 22 photobleached regions in 7 cells. Blebbistatin conditions were calculated from 9 photobleached regions in 3 cells. (E) Schematics of the proposed molecular picture of myosin turnover.

4.1.3 Discussion

Our results together provide preliminary evidence that points to a novel molecular picture of myosin cluster turnover. Firstly, myosin is turning over for every single cluster. Since myosin clusters contain multiple myosin filaments, the recovery half time may indicate the off rates (k_{off}) of single myosin molecules, myosin oligomers, or whole myosin filaments, as reaction-dominated FRAP kinetics directly corresponds to k_{off} [127, 128]. The smaller mobile fraction that comes with slower turnover may indicate that there is a larger stable core of myosin within myosin clusters that remains stably bound and not exchange. This stable core can be myosin motors within individual myosin filaments, or myosin filaments within a myosin cluster. One could imagine a follow-up experiment where single-molecule

characterization is possible to understand the exact molecular picture of myosin turnover. This would give great insight into how myosin can recycle myosin monomers or filaments to assemble new structures.

The molecular picture will also be crucial to interpreting how myosin turnover is regulated. Our research is consistent with previous research that found phosphorylation of the light chain controls myosin turnover. If single myosin molecules are turning over, then it is perhaps not surprising that myosin turnover rates are affected by RLC phosphorylation, since phosphorylation affects myosin filament assembly. If whole filaments are turning over, then RLC phosphorylation would instead tune the biochemical rates of myosin filament self-association, which is a subject that is largely unknown. Distinguishing between the two scenarios would further allow us to understand the regulation of myosin filaments and myosin clusters.

While some recent research suggested that myosin turnover is mechanosensitive, such that myosin turnover is slower on actomyosin structures under more tension (Kobb 2017), our results are more in line with recent study that NMIIA does not exhibit mechanosensitive turnover (Weissenbruch). Nonetheless, it is possible that these conflicting results can be reconciled. Since different myosin isoforms can co-polymerize into the same filament(Beach 2014), the turnover kinetics may be tuned dependent on the ratio between isoforms, such as NMIIA and NMIIB. The actomyosin structures imaged in Kobb's study may contain higher ratios of NMIIB to NMIIA. Future research will also need to take this into account.

4.2 F-actin regulation of NMIIA assembly

4.2.1 Introduction

In previous sections, I showed that myosin cluster sizes are determined by a limiting pool of myosin available for accretion. Since myosin filament assembly critically controls the pool

of myosin available for accretion, it is important to understand the regulation of myosin filament assembly. While most studies on NMII filament assembly have focused on the biochemical regulation, such as phosphorylation on the RLC by kinases and phosphatases, it is unclear whether these factors potentiate local NMII assembly in cells. There is so far no direct evidence that kinase activity in cells precede NMII assembly in cells. Rather, local myosin monomer concentration regulated by F-actin dynamics has been suggested to play a role [60]. This led us to investigate if F-actin plays a role in regulating NMII assembly.

NMII and F-actin are very coupled on actomyosin structures, so they may mutually regulate each other. This is perhaps best evidenced by the fact that F-actin gets perturbed while myosin is disrupted, or vise versa. For example, when myosin motor activity is perturbed by blebbistatin, the F-actin network also gets disrupted. The F-actin network architecture has been reported to be regulated by myosin-induced stress. For example, F-actin bundles can buckle and sever in the prescence of myosin [113, 129]. On the other hand, our work in Chapter 2 that myosin cluster size are affected when F-actin architecture is perturbed. Some studies have reported that myosin motor function can be regulated by F-actin. For example, myosin motor activity and myosin motility has been shown to depend on F-actin architecture [130, 131].

Myosin assembly has also been suggested to be regulated by F-actin. The best evidence so far is that purified NMII *in vitro* assembles faster in the presence of F-actin [62, 71, 72]. Mahajan et al. purified *Dictyostelium* myosin and used a fluorescence energy transfer assay to demonstrate that myosin assembly rates are faster in the presence of F-actin. While there is no direct evidence so far for human NMII assembly, my results in Chapter 2 support this idea. In section 2.5 and 2.7, myosin cluster sizes correlate positively with F-actin bundle intensity, suggesting that F-actin promotes the accumulation of myosin on F-actin bundles. In addition, when F-actin bundles are disrupted by α-actinin knockdown, myosin cluster sizes also decreased.

In this section, I aim to directly test if F-actin affects NMII assembly. I document preliminary investigation using two parallel approaches. One involves purifying NMII *in vitro* and using light scattering as an assay to measure NMII assembly in the presence and absence of F-actin. For the other approach, I induced *de novo* NMII assembly in cells treated with various pharmacological inhibitors against F-actin. My preliminary results suggests that F-actin does not affect NMII assembly *per se*, but formin or formin-mediated F-actin network may play a role.

4.2.2 Preliminary Results

First, we study NMII assembly with *in vitro* reconstituted NMIIA and F-actin. F-actin and NMIIA are purified with established protocols (fig. 4.4A). After purification, NMIIA is stored in a high salt buffer (500 µM KCl) so that it is in an assembly-incompetent state. To trigger NMIIA assembly, we made use of the ionic regulation of NMIIA and diluted the buffer until the KCl concentration reduced below a certain threshold (roughtly 150 µM, fig. 4.4B). To study whether NMIIA assembly is enhanced by F-actin, we will polymerize NMIIA in the prescence or absence of F-actin.

To quantify the extent and rate of NMIIA assembly, we designed an assay using light scattering, as conducted in the literature (Liu 2017, 2018). Briefly, we use a spectrofluorimeter to illuminate our sample at 365 nm and monitor side scattering signal at 365 nm (fig. 4.4C). At the same concentration, NMIIA filaments scatter more than NMIIA monomers, suggesting that higher scattering signal indicates NMIIA assembly (fig. 4.4D). Furthermore, the scattering signal increases with the concentration of both myosin monomers and myosin filaments. The scattering signal for myosin filaments increases faster than that of myosin monomers (fig. 4.4D). This demonstrates that the light scattering assay can be used to monitor myosin filament assembly.

To test the effect of F-actin, we polymerize NMIIA with or without F-actin and see if

the scattering signal changes. With the setup of our scattering assay, myosin scattering dominates and F-actin scattering can be largely ignored (fig. 4.4E, blue and red curves). We did not see a drastic difference between NMIIA scattering with or without F-actin (fig. 4.4E, red and green curves). To see if it is because we are not monitoring the optimal scattering wavelength, we scanned through the spectrum from 200 nm to 700 nm. While we see that there is also scattering response at different wavelengths, optimal scattering is indeed around 365 nm and we didn't see a significant difference in the trends for different conditions (fig. 4.4E). We also suspected that NMIIA polymerizing in the presence of F-actin can also contract F-actin into asters [74, 75, 76], which could complicate the interpretation of the scattering signal as the number and size of objects would change dramatically. Therefore, we added a small amount of capping protein to limit actin filament length, which prevents aster formation. Nonetheless, the scattering signal for NMIIA filaments remained similar with or without F-actin (fig. 4.4F). This suggested that NMIIA assembly wasn't affected by the presence of F-actin, at least in our *in vitro* assay.

In parallel, we want to see if myosin assembly in cells are affected by F-actin. To study myosin assembly in cells, we designed a similar assay as in section 2.2 to look at *de novo* myosin assembly. In this assay, we used the NIH 3T3 cell line because of their well-established role as a single-cell model. To trigger *de novo* myosin assembly, we first treated cells with 20µM Y-27 for 30 minutes to disassemble most myosin (fig. 4.5A). We see that most stress fiber structures are disassembled as well (fig. 4.5A). We then induced *de novo* myosin assembly by washing out Y-27 (fig. 4.5A). To visuliae the state of NMIIA assembly, we immunostained for NMIIA heavy chain and imaged with spinning disk confocal microscopy. We used the immunofluorescence intensity of NMIIA to quantify the state of NMIIA assembly. Briefly, we manually segmented cells and calculated intensity histograms. The intensity histogram boasts two characteristic peaks, one corresponding to background pixel intensities and one corresponding to NMIIA intensities (fig. 4.5B, C). The intensity histogram is then

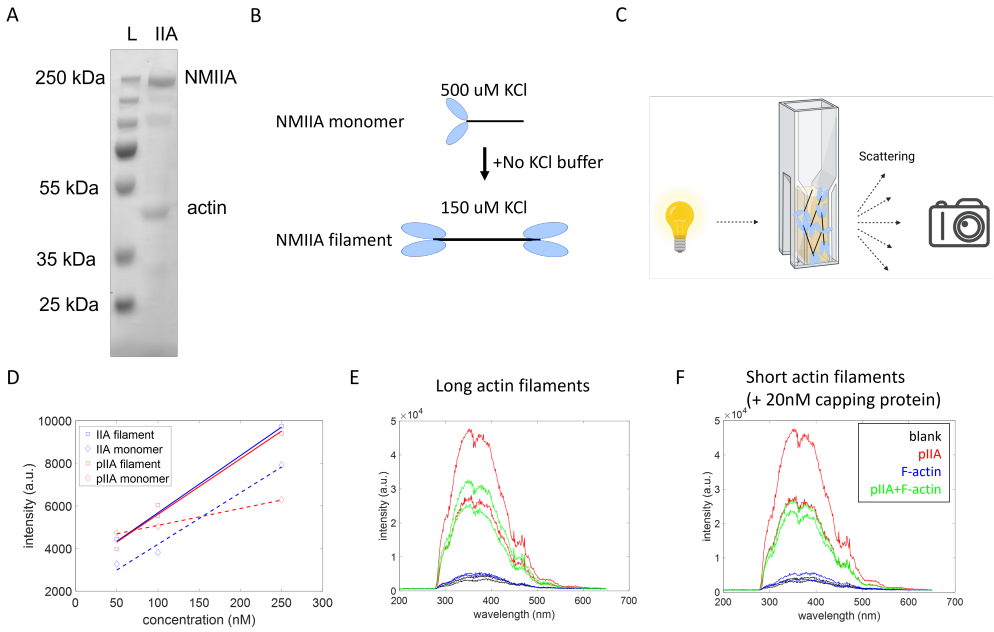

Figure 4.4: **NMIIA assembly are not affected by F-actin in *in vitro* scattering assays.** (A) SDS-PAGE results after NMIIA purification. (B) Schematics of triggering myosin assembly *in vitro*. (C) Schematics of the light scattering assay. Created with BioRender.com. (D) Light scattering signal for myosin monomers or filaments as a function of their concentration. (E) Scattering spectrum for myosin filaments with long actin filaments. (F) Scattering spectrum for myosin filaments with short actin filaments. Black curve represents buffer only, blue curve indicates F-actin only, red curve indicates phosphorylated NMIIA filaments, and green curve represents scattering from NMIIA assembled in the presence of F-actin.

fitted to a two-population Gaussian model to extract the intensities of the two peaks. To validate our approach, we saw that the NMIIA intensity goes down during Y-27 treatment and recovers once Y-27 is washed out, while the background signal remains the same.

To see what F-actin-related factors affect *de novo* NMIIA assembly in cells, we treated cells with various pharmacological inhibitors during the washout process. First, we disrupted the polymerization of F-actin by treating cells with 100nM Latrunculin A. While LatA disrupted the stress fiber network and remodeled F-actin and NMIIA into aster-like networks, NMIIA intensity remained similar (fig. 4.5D, E). Next, we selectively disrupted the Arp2/3-dependent F-actin meshwork with 100 µM CK-869. With Arp2/3 inhibition, the stress fiber network was largely unaffected, which is also reflected in the NMIIA intensity (fig. 4.5D, E).

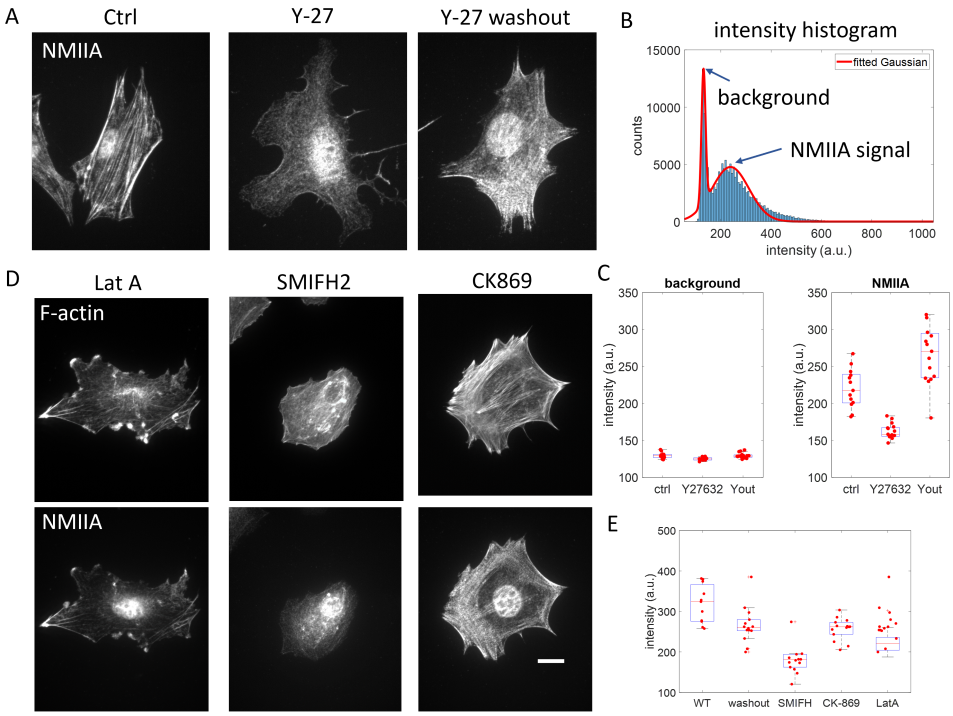

Figure 4.5: **Formins affect *de novo* NMIIA assembly in cells.** (A) Representative images of NMIIA in 3T3 cells. NMIIA are disassembled by Y-27 treatment and *de novo* assembly is triggered by washing out Y-27. (B) Example intensity histogram of the control cell in (A). The two peaks in the histogram is fitted to a two-population Gaussian to retrieve characteristic intensities of the background and NMIIA. (C) Background and NMIIA intensities of the three conditions in (A). (D) Representative images of F-actin and NMIIA in cells treated with 100 nM LatA, 15 µM SMIFH2, or 100 µM CK-869 during *de novo* NMIIA assembly. Scale bar 10 microm. (E) NMIIA intensities of the perturbation conditions in (D).

Lastly, when we selectively disrupt formin-dependent F-actin bundles with 15 µM SMIFH2, we see that both the stress fiber network and NMIIA are heavily disrupted (fig. 4.5D). The NMIIA intensity also decreased significantly (fig. 4.5E). This suggests that F-actin *per se* does not affect NMIIA assembly, but may depend either directly on formin or indirectly on formin-mediated F-actin bundles.

Since SMIFH2 is a pan-formin inhibitor that broadly inhibits the FH2 domains on all formins, we want to see if a specific formin impacts NMIIA assembly. We first identified that 3T3 cells express only a subset of about 8 types of formins (data not shown). We selectively targeted four of them that have been implicated to impact actomyosin structures in the

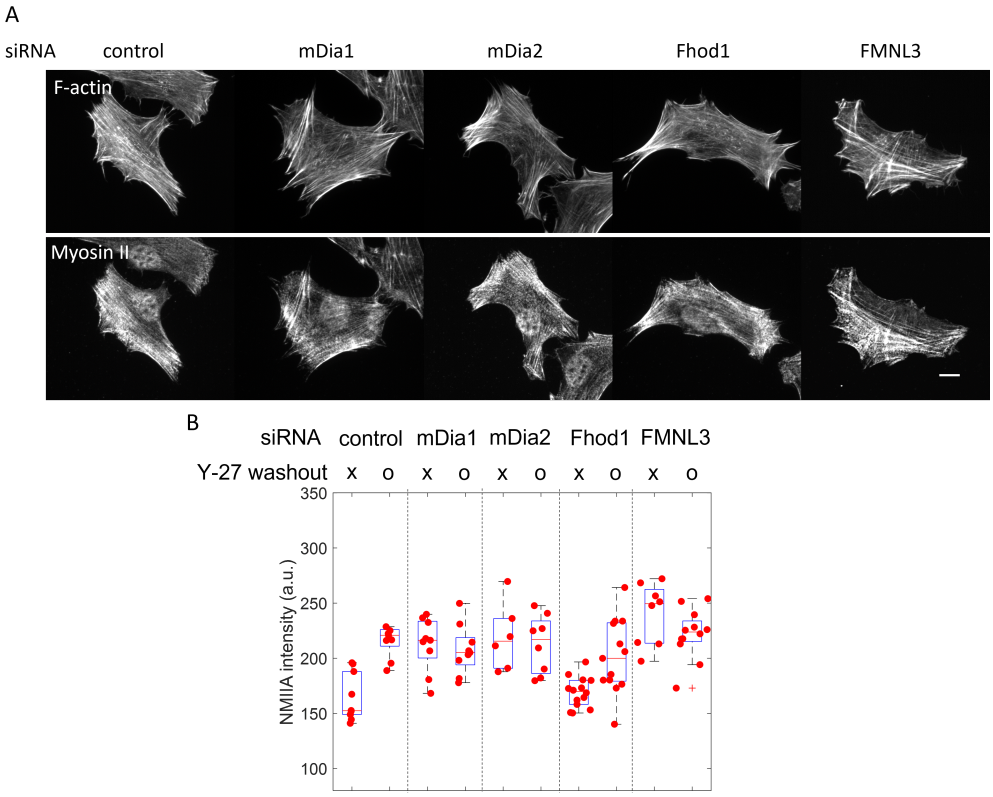

Figure 4.6: **Individual formins do not affect *de novo* NMIIA assembly in cells.** (A) Representative F-actin and NMIIA images of cells treated with various siRNA against specific formins. Scale bar 10 microm. (B) NMIIA intensities of formin knockdown cells. Conditions without Y-27 washout indicate NMIIA intensity before Y-27 treatment, and conditions with Y-27 washout indicate NMIIA intensity during *de novo* assembly.

literature: mDia1 [2, 37, 132], mDia2 [133, 134], Fhod1 [135], and FMNL3 [136]. To see if these formins affect NMIIA assembly, we performed the same *de novo* NMIIA assembly in 3T3 cells targeted with siRNA against the formins. While most F-actin networks in formin knockdown cells were disrupted, such as the reduction in dorsal stress fibers in mDia1 knockdown cells, NMIIA assembly is not affected (fig. 4.6A,B). This suggest that one specific formin may not affect NMIIA assembly, but rather the combined effect of formin-mediated F-actin network.

4.2.3 Discussion

The preliminary results suggests that the presence of F-actin *per se* doesn't enhance NMIIA filament assembly. Rather, formins or formin-mediated F-actin bundles may regulate NMIIA assembly. This presents an interesting potential pathway of myosin regulation. F-actin regulation and NMIIA regulation are often viewed as separate pathways. The formin-mediated regulation of myosin assembly may serve as an actin-dependent feedback to myosin assembly and therefore myosin-dependent contractility. This has been suggested in a recent study [137]. The origin of such regulation may be due to the effect of F-actin stabilizing assembled myosin. This is consistent with our views in section 2.5 and section 2.7, where we found that myosin accumulates more on F-actin bundles.

The preliminary investigation using the *in vitro* scattering assay of NMIIA assembly reveals that NMIIA assembly remains similar with or without F-actin. While much needs to be done to make sure both the purified proteins and the scattering assay behave as expected, the *in vitro* reconstitution approach remains a clean way of investigating myosin assembly. Without the complexity in cells, reconstituted systems provide a clean venue to decouple the effects of various intertwining factors that may exist in cells. This is exemplified by the rich knowledge on NMIIA assembly as a result of biochemical characterizations. Furthermore, reconstituted actomyosin systems with total internal reflection fluorescence microscopy (TIRF) have been used to dissect the interaction between myosin motors and F-actin networks. Combined together, these techniques may provide unequivocal evidence of whether F-actin or formin-mediated F-actin bundles promote NMIIA assembly.

We found that *de novo* NMIIA assembly is inhibited by the pan-formin inhibitior by SMIFH2, suggesting that formins play a role in NMIIA assembly. While it is possible that the phenotype is a result of the side-effect of SMIFH2 [138], we don't expect this to be the primary reason since we are using a concentration where NMIIA activity is minimally reduced. Since we fail to identify any myosin assembly phenotypes when we knocked down

specific formins, this points to a couple possibilities. One such possibility is that several formins have redundant functions in regulating NMIIA assembly. Alternatively, formins indirectly regulate NMIIA assembly through formin-mediated F-actin bundles. With the experimental setup and analysis techniques in Chapter 2, it is possible to gain more insight on the assembly status of individual myosin clusters.

4.3 Methods

4.3.1 Cell culture

For section 4.1, U2OS cells were cultured in McCoy's 5A Medium (Sigma-Aldrich) supplemented with 10% FBS (Corning) and 2 mM L-glutamine (Invitrogen). To visualize myosin, mScarlet was knocked in at the C-terminal locus and eGFP at the N-terminal locus of the MYH9 gene using CRISPR. For mScarlet, the target/Cas9 plasmid pSpCas9(BB)-2A-Puro (PX459) V2.0 (http://www.addgene.org/62988/) with target sequence AGGTAGATGGCAAAGCGGAT was engineered according to established protocols (Ran et al, 2013). To create a donor plasmid, pUC57 was digested with EcoRI and StuI and purified. A four-piece Gibson assembly was then performed. Three gBlocks (5' HDR, linker/mScarlet, and 3'HDR) were obtained from IDT with overlapping extensions to mediate Gibson assembly. The 5' HDR arm is 867 bp of genomic sequence terminating immediately prior to the endogenous STOP codon. Silent mutations (AaGTtGAcGGaAAAGCGGATGGt) were placed in the target sequence to prevent Cas9 binding and cleavage of the donor plasmid. The linker/mScarlet was placed in-frame with the coding sequence and consists of an 18 amino acid GS rich linker and mScarlet-I fluorophore. The 3' HDR arm is 684 bp immediately downstream of the MYH9 coding sequence. U2OS cells were transfected with both Cas9 and donor plasmids. After 1 week in culture, a polyclonal mScarlet positive population was obtained using fluorescent activated cell sorting (FACS). For eGFP, the following mod-

ifications were made for the CRISPR procedure. The target sequence for the guide RNA is AAACTTCATCAACAATCCGC. Donor plasmid was generated in pUCIDT-AmpR with internal mEGFP flanked by 5' and 3' HDR. The 5'HDR is 498 bp upstream of endogenous start and 3'HDR is 383 bp downstream of endogenous start. Cells were previously treated with BM cyclin (Roche) per manufacturer instructions to eliminate mycoplasma.

For section 4.2, NIH 3T3 cells were cultured in Dulbecco's Modified Eagle Medium (Sigma-Aldrich) supplemented with 10% FBS (Corning) and 2 mM L-glutamine (Invitrogen).

4.3.2 Drug Perturbations and Gene Knockdown

For section 4.1, cells were either treated with 5 µM Y-27632 (EMD Millipore), or 5 µM para-nitroblebbistatin (Cayman Chemical) for at least 30 minutes, or 1 $\mu g\,mL^{-1}$ CN03 (Cytoskeleton Inc.) for 2 hours.

For section 4.2, formins were knocked down with ON-TARGETplus SMARTpool siRNAs against mouse Dia1, Dia2, Fhod 1, and FMNL3 (Horizon Discovery). For siRNA control, ON-TARGETplus non-targeting siRNA is used (Horizon Discovery). siRNA transfection is conducted with Dharmafect 1 per manufacturer instructions (Horizon Discovery).

4.3.3 Immunofluorescence

Cells were first washed with warm PBS. Then cells were fixed and permeabilized with 4% paraformaldehyde (EMS) and 0.5% Triton X-100 (Fisher Scientific), diluted in 1.5% BSA (Fisher Scientific) and cytoskeletal buffer (0.01M MES, 0.003M MgCl2, 0.138M KCl, 0.002M EGTA, pH 6.8). To visualize F-actin, cells were then washed with PBS then incubated with Alexa-647 phalloidin (Invitrogen 1:1000), 0.5% Triton X-100, and 1.5% BSA diluted in cytoskeletal buffer. Cells were then washed with PBS and mounted onto a coverslip with ProLong gold antifade reagent (Invitrogen).

4.3.4 Microscopy and Live Cell Imaging

Cells were imaged on an inverted Nikon Ti-E (Nikon, Melville, NY) with a Yokogawa CSU-X confocal scanning head (Yokogawa Electric, Tokyo, Japan) and laser merge model with 491, 561, and 642nm laser lines (Spectral Applied Research, Ontario, Canada). Images were collected on a Zyla 4.2 sCMOS Camera (Andor, Belfast, UK). A 60x 1.2 Plan Apo water (Nikon) objective was used to collect images. MetaMorph Automation and Image Analysis Software (Molecular Devices, Sunnvyale,CA) controlled all hardware. For the analysis of NMIIA assembly, all imaging conditions are controlled to be the same in each set of experiments, including laser intensity and exposure time. For fluorescence recovery after photobleaching (FRAP) experiments, Airyscan imaging was performed on a Zeiss LSM 980 microscope equipped with the Airyscan 2 detector. Images were acquired using the MPLX SR-4X mode and processed by Zen Blue 3.0 software using the Airyscan processing feature with default settings. For live cell imaging, cells were mounted on an imaging chamber (Chamlide) and maintained at 37 °C. For live cell imaging, cell medium was replaced with Dulbecco's Modified Eagle Medium without phenol red (Corning) supplemented with 10% FBS, 2mM L-glutamine, 1% penicillin-streptomycin, 10mM HEPES and 30 µL/mL Oxyrase (Oxyrase Inc.).

4.3.5 Purification of Non-muscle Myosin IIA

Non-muscle myosin IIA is purified according to published protocols [139]. Briefly, expired human platelets were collected from the University of Chicago Hospital. Platelets were spun down and lysed through a Dounce homogenizer. Proteins were precipitated from the supernatant using ammonium sulfate. NMIIA was isolated through dialysis and column chromatography. Purified NMIIA were further phosphorylated with MLCK and calmodulin. Purified NMIIA were stored in a buffer with 500 µM KCl.

4.3.6 Light Scattering

Light scattering is conducted as in the literature [140, 141]. Briefly, NMIIA assembly is induced by reducing the KCl concentration in the buffer to 150 µM. A spectrofluorimeter is used to assess the scattering signal. Unless otherwise noted, side scattering is assessed at 365 nm with the slit width 1 nm.

4.3.7 Image Processing

To analyze FRAP experiments, both FRAP and control regions were identified. A double normalization scheme is used to normalize data and correct for photobleaching $I_{corr} = \frac{I_{roi}}{I_{ref}}\frac{I_{ctrl,pre}}{I_{roi,pre}}$. The FRAP curve is fitted to $FRAP(t) = C(1 - e^{-\alpha t})$ to extract the recovery half time $\tau_{1/2} = \frac{ln2}{\alpha}$ and the mobile fraction C. For NMIIA intensity analysis in section 4.2, cells are first manually segmented. Intensity histogram within the cell region is fitted to the two population Gaussian model $f(x) = a_1 e^{-(\frac{x-b_1}{c_1})^2} + a_2 e^{-(\frac{x-b_2}{c_2})^2}$. The smaller of the two Gaussian means is used to represent background intensity, while the larger of the two Gaussian means is used to represent NMIIA intensity.

CHAPTER 5

CONCLUSION

5.1 Summary

In summary, my Ph.D. work focused on understanding the dynamics and regulation of myosin clusters on stress fibers. My thesis work helped understand how cytoskeletal structures self-assemble and their regulation. Concretely, my thesis work explained how myosin cluster sizes are regulated on stress fibers and investigated the influence by the F-actin network. We extracted important material properties of the cellular actomyosin structure directly from experimentally-determined myosin cluster dynamics. Lastly, I investigated the nature and regulation of myosin cluster turnover.

We found that myosin clusters on stress fibers grow via accretion, where free myosin accumulate to existing clusters due to self-affinity of myosin filaments. Myosin accretion depends on ROCK activity, which increases the pool of assembled myosin filaments, and myosin motor activity, which stabilizes myosin filaments on bundles. Both factors effectively increases the pool of myosin available for accretion. We find that the pool of myosin critically determines myosin cluster sizes, suggesting that availbility of myosin is the limiting factor that determines myosin cluster sizes. As a result, myosin clusters on different F-actin architecture compete for the same limiting of myosin.

Through collaborative work, we constructed a generalized cross-correlatoin function between velocity fields and another field of interest. When applied to dynamics driven by actomyosin, we extracted the material response to myosin-induced strain. Specifically in subcellular actomyosin networks like stress fibers, we isolated various modes of deformation driven by actomyosin, from long-range retrograde flow that persist over minutes to local myosin-driven deformations that de-correlated over 10 seconds. Our method can distinguish different modes of contraction between transverse arcs and ventral stress fibers, and also pick

up on changes in local contraction when contractility is locally driven by optogenetic RhoA activation.

Finally, we presented preliminary investigation of myosin cluster turnover and F-actin-dependent NMII assembly. We found that each myosin cluster is turning over at a similar rate. RhoA/ROCK controls myosin cluster turnover not because of the changes in myosin monomer concentration but rather reflects changes in myosin exchange dynamics within individual clusters. This may be due to the phosphorylation dynamics, or due to effects of mechanical tension. The presence of F-actin doesn't affect NMII assembly *per se*, but formins or formin-dependent F-actin networks seem to affect NMII assembly.

5.2 Future directions

5.2.1 Myosin clusters

Myosin clusters can grow by accretion with a positive feedback. This suggests self-affinity between myosin filaments. It would be cool to understand the origin of this self-affinity. This could be unspecific molecular interaction between myosin filaments. This could also be due to specific interactions mediated by other proteins. Some potential candidates include myosin-18B and tropomyosin 3.1 (Tpm 3.1). Since my experiment in Chapter 2, section 2 reveals cluster growth, this would be an ideal assay to test these ideas.

Now that we can localize and calculate the size of myosin clusters, we can start to understand how local myosin cluster assembly is established. For years, we assume that it's the local ROCK activity that promotes local assembly, possibly preceded by RhoA activity. However, there is no direct evidence. Furthermore, recent studies suggest that local F-actin dynamics may play a role [60, 142]. With a good antibody against RhoA/ROCK activity, or against phosphorylated RLC, one could see if there is good correlation between RLC phosphorylation and myosin cluster assembly. If there is a biosensor for RhoA/ROCK

activity, one can further conduct spatiotemporal analysis to see if assembly/growth of myosin clusters coincide with RhoA/ROCK activity.

Myosin cluster analysis can also reveal new insights into stress fiber repair. Stress fibers constantly undergo damage, either by myosin-induced strain or external stretching. When stress fibers are partially damaged, actin filament bundle decrease and myosin is gone. During the repair, zyxin gets recruited to the strain site in a mechanosensitive manner [143, 144], which recruits repair factors like VASP and α-actinin [145, 146]. While the molecular pathway and mechanism of repair has been well-characterized, myosin is not in the picture. At what point myosin re-establish their organization, and the mechanism is unknown. By quantitative imaging of endogenous myosin at the site of stress fiber damage, the author expect that this missing piece can be solved.

On the technical side, we can improve our analysis to include more spatiotemporal details of myosin cluster dynamics. Our analysis is restricted by the caveat that we are using confocal imaging, so when myosin clusters get very dense they all become one big puncta. we can use super-resolution imaging, with the head-tail-head construct, to unambiguously identify each myosin cluster. The segmentation may require pattern-matching algorithms, or deep-learning based computer vision techniques. Furthermore, to fully dissect myosin cluster dynamics, tracking myosin clusters over time will be necessary. This way we can see how myosin intensity change over time, and identify assembly or disassembly events of these structures. To minimize error, we need myosin cluster segmentation with sufficiently good quality, and an algorithm to link trajectories of dense objects. Most existing algorithms rely solely on object position, which doesn't yield good enough results. Incorporating other features of the object, such as velocity and object feature, might improve tracking of dense moving objects.

5.2.2 Myosin turnover

The molecular picture of myosin cluster turnover is particularly interesting, as the turnover of myosin clusters indicates stability of myosin clusters. Combined with myosin cluster identification and turnover, one could start to look at myosin cluster turnover at the single cluster level. Conventional FRAP analysis usually computes the FRAP recovery of the whole photobleached region. With our technique, one could get turnover on a single cluster. This allows for better analysis and molecular-level detail about myosin turnover and its regulation. For example, with single-molecule level imaging, one can start to dissect the molecular picture of myosin cluster turnover: whether myosin molecules, oligomers, or myosin filaments are turning over. This single cluster level analysis also allows for detailed analysis of the regulation of myosin clusters. One could first see if myosin clusters on different location of the cell turns over differently, then ask if the variation arises from myosin cluster size, phosphorylation signaling, or F-actin architecture. Since intensity curves of single clusters have much more fluctuation over time, this might require a dataset that is big enough to have enough statistical power to make the conclusion. Alternatively, the fluctuations may reveal additional detail of myosin turnover and can be harnessed to evaluate the differences of individual myosin clusters.

5.2.3 Formin regulation

Our preliminary results suggest that formin affects NMII assembly. This result, if confirmed, reveals an interesting feedback not previously characterized. Normally actin-dependent regulation and myosin-dependent regulation are seemed as separate pathways. If true, this suggests a cross-over in the two pathways, potentially enabling feedback circuits. With feedback between actin and myosin, this adds another layer of complexity, but potentailly can explain the plasticity of the actomyosin network. This has been recently suggested by a study that showed such a crosstalk between myosin-generated cellular forces and formin activity

[137]. As a result, careful characterization of NMII assembly, or myosin cluster assembly, under formin knockdown cells will be insightful.

5.2.4 Response function

The results from the response function analysis is very promising and may hold the key to revealing how mechanochemical control is achieved in stress fibers. For example, it remains of great interest how stress fibers control their mechanical properties and how mechanical properties respond to external perturbations. Many models have been proposed based on the results from *in vitro* reconstituted systems. For example, F-actin network properties is proposed to determine contractility generated by the network, such as the rigidity, connectivity, architecture, and fluidity of the F-actin network. One could now precisely deplete F-actin in cells, or selectively perturb F-actin network architecture by knocking down different actin binding proteins, like filamin, fascin, or cofilin, and test how response of cellular actomyosin networks change.

To better interpret the results from the response function analysis, we need to be able to extract material properties directly from the material response. While we have shown that there is such a relation in the well-charaterized active nematics system, actomyosin networks in cells still present a challenge because of the multiple molecular components involves and the boundary effects born of the finite size of the cell. This makes it difficult to extract unambiguously how material response corresponds to material properties. With a realistic model if the cellular actomyosin network, however, one could theoretically or computationally extract such parameters.

5.3 Outlook

As mechanical forces are important, understanding myosin self-organization will help understand cellular force-generation, the assembly and maintenance of actomyosin structures, and

how actomyosin structures respond to perturbations. For example, myosin cluster analysis can be applied to understand how myosin clusters respond to mechanical perturbations such as stretching or varying substrate stiffness.

Response function analysis holds the promise to start understanding the material properties and response of cytoskeletal structures. This has been difficult because the actomyosin networks in cells are tightly coupled with one another. Global perturbations aimed at understanding the effect of one parameter often end up affecting more than one aspect of the actomyosin network. While local perturbations, like laser nanosurgery or optogenetics, can isolate the effects more, interpreting local mechanical properties is still difficult because the effect of the local perturbation is often coupled with the surrounding network. With response function analysis, we can separate out contributions from long-range isotropic flow and local myosin-induced response. We can start to unveil how cytoskeletal regulators affect material properties of subcellular actomyosin networks. This can be the beginning to dissect the mechanochemical feedback loops that exist in cells that allows the actomyosin network to be an adaptive material.

This thesis demonstrates that by utilizing quantitative methods, from careful experimental design, analysis, and modeling, we can extract physical principles that govern self-assembly of actomyosin structures. Cell biology in the past relies heavily on qualitative methods, making conclusions from only a population of cells. This misses out not only on the quantity, but also the spatiotemporal dynamics and regulation. Advances in technology have allowed scientists to develop new quantitative tools to circumvent the shortcomings. For example, advances in molecular biology allow us to precisely edit the genome by CRISPR. This enables precise genetic perturbations and fluorescent tagging of endogenous proteins. Advances in microscopy allow us to conduct multi-channel, high spatiotemporal resolution, imaging to visualize the spatiotemporal dynamics in live cells. Advances in computational analysis and modeling methods allow us to harness the big experimental datasets and ex-

tract information. Tools like machine learning and deep learning can further accelerate image analysis and modeling. With all these techniques, the time is ripe to understand how cells build and control subcellular structures over space and time. This thesis demonstates one such example on understanding how myosin cluster sizes are determined on stress fibers. The author expect that the application of the same quantitative mindset and technique will help unveil the biophysics of how organelles and subcellular structures are built.

REFERENCES

[1] Tony Y.-C. Tsai, Sean R. Collins, Caleb K. Chan, Amalia Hadjitheodorou, Pui-Ying Lam, Sunny S. Lou, Hee Won Yang, Julianne Jorgensen, Felix Ellett, Daniel Irimia, Michael W. Davidson, Robert S. Fischer, Anna Huttenlocher, Tobias Meyer, James E. Ferrell, and Julie A. Theriot. Efficient Front-Rear Coupling in Neutrophil Chemotaxis by Dynamic Myosin II Localization. *Developmental Cell*, 49(2):189–205.e6, April 2019. ISSN 15345807. doi:10.1016/j.devcel.2019.03.025. URL `https://linkinghub.elsevier.com/retrieve/pii/S1534580719302369`.

[2] Patrick W. Oakes, Yvonne Beckham, Jonathan Stricker, and Margaret L. Gardel. Tension is required but not sufficient for focal adhesion maturation without a stress fiber template. *The Journal of Cell Biology*, 196(3):363–374, February 2012. ISSN 0021-9525, 1540-8140. doi:10.1083/jcb.201107042. URL `http://www.jcb.org/lookup/doi/10.1083/jcb.201107042`.

[3] Jonathan Stricker, Yvonne Beckham, Michael W Davidson, and Margaret L Gardel. Myosin II-Mediated Focal Adhesion Maturation Is Tension Insensitive. *PLOS ONE*, 8 (7):e70652–e70652, 2013. doi:10.1371/journal.pone.0070652. URL `https://doi.org/10.1371/journal.pone.0070652`.

[4] Caroline Laplante, Julien Berro, Erdem Karatekin, Ariel Hernandez-Leyva, Rachel Lee, and Thomas D. Pollard. Three Myosins Contribute Uniquely to the Assembly and Constriction of the Fission Yeast Cytokinetic Contractile Ring. *Current Biology*, 25(15):1955–1965, August 2015. ISSN 09609822. doi:10.1016/j.cub.2015.06.018. URL `https://linkinghub.elsevier.com/retrieve/pii/S0960982215006831`.

[5] Sanjay Kumar and Valerie M. Weaver. Mechanics, malignancy, and metastasis: The force journey of a tumor cell. *Cancer and Metastasis Reviews*, 28(1-2):113–127, June 2009. ISSN 0167-7659, 1573-7233. doi:10.1007/s10555-008-9173-4. URL `http://link.springer.com/10.1007/s10555-008-9173-4`.

[6] Venkaiah Betapudi, Lucila S. Licate, and Thomas T. Egelhoff. Distinct Roles of Nonmuscle Myosin II Isoforms in the Regulation of MDA-MB-231 Breast Cancer Cell Spreading and Migration. *Cancer Research*, 66(9):4725–4733, May 2006. ISSN 0008-5472, 1538-7445. doi:10.1158/0008-5472.CAN-05-4236. URL `http://cancerres.aacrjournals.org/content/66/9/4725`.

[7] Robert C. Buck. Reorientation response of cells to repeated stretch and recoil of the substratum. *Experimental Cell Research*, 127(2):470–474, June 1980. ISSN 00144827. doi:10.1016/0014-4827(80)90456-5. URL `https://linkinghub.elsevier.com/retrieve/pii/0014482780904565`.

[8] Marc Hippler, Kai Weißenbruch, Kai Richler, Enrico D. Lemma, Masaki Nakahata, Benjamin Richter, Christopher Barner-Kowollik, Yoshinori Takashima, Akira

Harada, Eva Blasco, Martin Wegener, Motomu Tanaka, and Martin Bastmeyer. Mechanical stimulation of single cells by reversible host-guest interactions in 3D microscaffolds. *Science Advances*, 6(39):eabc2648, September 2020. ISSN 2375-2548. doi:10.1126/sciadv.abc2648. URL https://www.science.org/doi/10.1126/sciadv.abc2648.

[9] Michele M. Nava, Yekaterina A. Miroshnikova, Leah C. Biggs, Daniel B. Whitefield, Franziska Metge, Jorge Boucas, Helena Vihinen, Eija Jokitalo, Xinping Li, Juan Manuel García Arcos, Bernd Hoffmann, Rudolf Merkel, Carien M. Niessen, Kris Noel Dahl, and Sara A. Wickström. Heterochromatin-Driven Nuclear Softening Protects the Genome against Mechanical Stress-Induced Damage. *Cell*, 181 (4):800–817.e22, May 2020. ISSN 00928674. doi:10.1016/j.cell.2020.03.052. URL https://linkinghub.elsevier.com/retrieve/pii/S0092867420303457.

[10] Paul A. Janmey, Daniel A. Fletcher, and Cynthia A. Reinhart-King. Stiffness Sensing by Cells. *Physiological Reviews*, 100(2):695–724, April 2020. ISSN 0031-9333, 1522-1210. doi:10.1152/physrev.00013.2019. URL https://journals.physiology.org/doi/10.1152/physrev.00013.2019.

[11] Adam J. Engler, Shamik Sen, H. Lee Sweeney, and Dennis E. Discher. Matrix Elasticity Directs Stem Cell Lineage Specification. *Cell*, 126(4):677–689, August 2006. ISSN 00928674. doi:10.1016/j.cell.2006.06.044. URL https://linkinghub.elsevier.com/retrieve/pii/S0092867406009615.

[12] James R Sellers. Myosins: a diverse superfamily. *Biochimica et Biophysica Acta (BBA) - Molecular Cell Research*, 1496(1):3–22, March 2000. ISSN 01674889. doi:10.1016/S0167-4889(00)00005-7. URL http://linkinghub.elsevier.com/retrieve/pii/S0167488900000057.

[13] Miguel Vicente-Manzanares, Xuefei Ma, Robert S. Adelstein, and Alan Rick Horwitz. Non-muscle myosin II takes centre stage in cell adhesion and migration. *Nature Reviews Molecular Cell Biology*, 10(11):778–790, November 2009. ISSN 1471-0072, 1471-0080. doi:10.1038/nrm2786. URL http://www.nature.com/articles/nrm2786.

[14] Aidan M Fenix, Abigail C Neininger, Nilay Taneja, Karren Hyde, Mike R Visetsouk, Ryan J Garde, Baohong Liu, Benjamin R Nixon, Annabelle E Manalo, Jason R Becker, Scott W Crawley, David M Bader, Matthew J Tyska, Qi Liu, Jennifer H Gutzman, and Dylan T Burnette. Muscle-specific stress fibers give rise to sarcomeres in cardiomyocytes. *eLife*, 7:e42144, December 2018. ISSN 2050-084X. doi:10.7554/eLife.42144. URL https://doi.org/10.7554/eLife.42144.

[15] Jie Sun, Yan-Ning Qiao, Tao Tao, Wei Zhao, Li-Sha Wei, Ye-Qiong Li, Wei Wang, Ye Wang, Yu-Wei Zhou, Yan-Yan Zheng, Xin Chen, Hong-Chun Pan, Xue-Na Zhang, and Min-Sheng Zhu. Distinct Roles of Smooth Muscle and Non-muscle Myosin Light Chain-Mediated Smooth Muscle Contraction. *Frontiers in Physiology*, 11:

593966, December 2020. ISSN 1664-042X. doi:10.3389/fphys.2020.593966. URL https://www.frontiersin.org/articles/10.3389/fphys.2020.593966/full.

[16] Luca Melli, Neil Billington, Sara A. Sun, Jonathan E. Bird, Attila Nagy, Thomas B. Friedman, Yasuharu Takagi, and James R. Sellers. Bipolar filaments of human nonmuscle myosin 2-A and 2-B have distinct motile and mechanical properties. *eLife*, February 2018. doi:10.7554/eLife.32871. URL https://elifesciences.org/articles/32871.

[17] M. Kovacs, K. Thirumurugan, P. J. Knight, and J. R. Sellers. Load-dependent mechanism of nonmuscle myosin 2. *Proceedings of the National Academy of Sciences*, 104 (24):9994–9999, June 2007. ISSN 0027-8424, 1091-6490. doi:10.1073/pnas.0701181104. URL http://www.pnas.org/cgi/doi/10.1073/pnas.0701181104.

[18] Kai Weißenbruch, Justin Grewe, Marc Hippler, Magdalena Fladung, Moritz Tremmel, Kathrin Stricker, Ulrich Sebastian Schwarz, and Martin Bastmeyer. Distinct roles of nonmuscle myosin II isoforms for establishing tension and elasticity during cell morphodynamics. *eLife*, 10:e71888, August 2021. ISSN 2050-084X. doi:10.7554/eLife.71888. URL https://elifesciences.org/articles/71888.

[19] Neil Billington, Aibing Wang, Jian Mao, Robert S. Adelstein, and James R. Sellers. Characterization of Three Full-length Human Nonmuscle Myosin II Paralogs. *Journal of Biological Chemistry*, 288(46):33398–33410, November 2013. ISSN 0021-9258, 1083-351X. doi:10.1074/jbc.M113.499848. URL http://www.jbc.org/lookup/doi/10.1074/jbc.M113.499848.

[20] Attila Nagy, Yasuharu Takagi, Neil Billington, Sara A. Sun, Davin K.T. Hong, Earl Homsher, Aibing Wang, and James R. Sellers. Kinetic Characterization of Nonmuscle Myosin IIB at the Single Molecule Level. *Journal of Biological Chemistry*, 288(1): 709–722, January 2013. ISSN 00219258. doi:10.1074/jbc.M112.424671. URL https://linkinghub.elsevier.com/retrieve/pii/S0021925820653765.

[21] Takashi Nakasawa, Masayuki Takahashi, Fumiko Matsuzawa, Seiichi Aikawa, Yuki Togashi, Takayuki Saitoh, Akihiko Yamagishi, and Michio Yazawa. Critical Regions for Assembly of Vertebrate Nonmuscle Myosin II. *Biochemistry*, 44(1):174–183, January 2005. ISSN 0006-2960, 1520-4995. doi:10.1021/bi048807h. URL http://pubs.acs.org/doi/abs/10.1021/bi048807h.

[22] Tom L. Kaufmann and Ulrich S. Schwarz. Electrostatic and bending energies predict staggering and splaying in nonmuscle myosin II minifilaments. *PLOS Computational Biology*, 16(7):e1007801, July 2020. ISSN 1553-7358. doi:10.1371/journal.pcbi.1007801. URL https://dx.plos.org/10.1371/journal.pcbi.1007801.

[23] D. Ricketson, C. A. Johnston, and K. E. Prehoda. Multiple tail domain interactions stabilize nonmuscle myosin II bipolar filaments. *Proceedings of the National Academy of Sciences*, 107(49):20964–20969, December 2010. ISSN 0027-8424, 1091-6490. doi:10.1073/pnas.1007025107. URL http://www.pnas.org/cgi/doi/10.1073/pnas.1007025107.

[24] Justin Grewe and Ulrich S. Schwarz. Mechanosensitive self-assembly of myosin II minifilaments. *Physical Review E*, 101(2), February 2020. ISSN 2470-0045, 2470-0053. doi:10.1103/PhysRevE.101.022402. URL https://link.aps.org/doi/10.1103/PhysRevE.101.022402.

[25] K. A. Newell-Litwa, R. Horwitz, and M. L. Lamers. Non-muscle myosin II in disease: mechanisms and therapeutic opportunities. *Disease Models & Mechanisms*, 8(12): 1495–1515, December 2015. ISSN 1754-8403, 1754-8411. doi:10.1242/dmm.022103. URL http://dmm.biologists.org/cgi/doi/10.1242/dmm.022103.

[26] Natalya G Dulyaninova and Anne R Bresnick. The heavy chain has its day: Regulation of myosin-II assembly. *BioArchitecture*, 3(4):77–85, July 2013. ISSN 1949-0992, 1949-100X. doi:10.4161/bioa.26133. URL http://www.tandfonline.com/doi/abs/10.4161/bioa.26133.

[27] Tianzhi Luo, Krithika Mohan, Vasudha Srivastava, Yixin Ren, Pablo A. Iglesias, and Douglas N. Robinson. Understanding the Cooperative Interaction between Myosin II and Actin Cross-Linkers Mediated by Actin Filaments during Mechanosensation. *Biophysical Journal*, 102(2):238–247, January 2012. ISSN 00063495. doi:10.1016/j.bpj.2011.12.020. URL http://linkinghub.elsevier.com/retrieve/pii/S0006349511054221.

[28] Jordan R. Beach, Lin Shao, Kirsten Remmert, Dong Li, Eric Betzig, and John A. Hammer. Nonmuscle Myosin II Isoforms Coassemble in Living Cells. *Current Biology*, 24(10):1160–1166, May 2014. ISSN 09609822. doi:10.1016/j.cub.2014.03.071. URL http://linkinghub.elsevier.com/retrieve/pii/S0960982214003935.

[29] Somanna Kollimada, Fabrice Senger, Timothée Vignaud, Manuel Théry, Laurent Blanchoin, and Laëtitia Kurzawa. The biochemical composition of the actomyosin network sets the magnitude of cellular traction forces. *Molecular Biology of the Cell*, 32(18): 1737–1748, August 2021. ISSN 1059-1524, 1939-4586. doi:10.1091/mbc.E21-03-0109. URL https://www.molbiolcell.org/doi/10.1091/mbc.E21-03-0109.

[30] Michael Murrell, Patrick W Oakes, Martin Lenz, and Margaret L Gardel. Forcing cells into shape: the mechanics of actomyosin contractility. *Nature Reviews: Molecular Cell Biology*, 16(8):486–498, 2015. ISSN 1471-0072. doi:10.1038/nrm4012. URL http://dx.doi.org/10.1038/nrm4012.

[31] Laetitia Kurzawa, Benoit Vianay, Fabrice Senger, Timothée Vignaud, Laurent Blanchoin, and Manuel Théry. Dissipation of contractile forces: the missing piece in cell mechanics. *Molecular Biology of the Cell*, 28(14):1825–1832, July 2017. ISSN 1059-1524, 1939-4586. doi:10.1091/mbc.e16-09-0672. URL https://www.molbiolcell.org/doi/10.1091/mbc.e16-09-0672.

[32] Mridula Balakrishnan, Shannon F. Yu, Samantha M. Chin, David B. Soffar, Stefanie E. Windner, Bruce L. Goode, and Mary K. Baylies. Cofilin Loss in Drosophila

Muscles Contributes to Muscle Weakness through Defective Sarcomerogenesis during Muscle Growth. *Cell Reports*, 32(3):107893, July 2020. ISSN 22111247. doi:10.1016/j.celrep.2020.107893. URL https://linkinghub.elsevier.com/retrieve/pii/S2211124720308743.

[33] Frank Li, Danielle Buck, Josine De Winter, Justin Kolb, Hui Meng, Camille Birch, Rebecca Slater, Yael Natelie Escobar, John E. Smith, Lin Yang, John Konhilas, Michael W. Lawlor, Coen Ottenheijm, and Henk L. Granzier. Nebulin deficiency in adult muscle causes sarcomere defects and muscle-type-dependent changes in trophicity: novel insights in nemaline myopathy. *Human Molecular Genetics*, 24(18):5219–5233, September 2015. ISSN 0964-6906, 1460-2083. doi:10.1093/hmg/ddv243. URL https://academic.oup.com/hmg/article-lookup/doi/10.1093/hmg/ddv243.

[34] Barbara Joureau, Josine Marieke De Winter, Stefan Conijn, Sylvia J. P. Bogaards, Igor Kovacevic, Albert Kalganov, Malin Persson, Johan Lindqvist, Ger J. M. Stienen, Thomas C. Irving, Weikang Ma, Michaela Yuen, Nigel F. Clarke, Dilson E. Rassier, Edoardo Malfatti, Norma B. Romero, Alan H. Beggs, and Coen A. C. Ottenheijm. Dysfunctional sarcomere contractility contributes to muscle weakness in *ACTA1* -related nemaline myopathy (NEM3): *ACTA1* -Related Myopathy. *Annals of Neurology*, 83(2):269–282, February 2018. ISSN 03645134. doi:10.1002/ana.25144. URL https://onlinelibrary.wiley.com/doi/10.1002/ana.25144.

[35] S. Tojkander, G. Gateva, and P. Lappalainen. Actin stress fibers - assembly, dynamics and biological roles. *Journal of Cell Science*, 125(8):1855–1864, April 2012. ISSN 0021-9533, 1477-9137. doi:10.1242/jcs.098087. URL http://jcs.biologists.org/cgi/doi/10.1242/jcs.098087.

[36] Elena Kassianidou and Sanjay Kumar. A biomechanical perspective on stress fiber structure and function. *Biochimica et Biophysica Acta (BBA) - Molecular Cell Research*, 1853(11):3065–3074, November 2015. ISSN 01674889. doi:10.1016/j.bbamcr.2015.04.006. URL https://linkinghub.elsevier.com/retrieve/pii/S0167488915001251.

[37] Pirta Hotulainen and Pekka Lappalainen. Stress fibers are generated by two distinct actin assembly mechanisms in motile cells. *Journal of Cell Biology*, 173(3):383–394, May 2006. ISSN 0021-9525. doi:10.1083/jcb.200511093. URL https://doi.org/10.1083/jcb.200511093.

[38] Shiqiong Hu, Kinjal Dasbiswas, Zhenhuan Guo, Yee-Han Tee, Visalatchi Thiagarajan, Pascal Hersen, Teng-Leong Chew, Samuel A. Safran, Ronen Zaidel-Bar, and Alexander D. Bershadsky. Long-range self-organization of cytoskeletal myosin II filament stacks. *Nature Cell Biology*, 19(2):133–141, January 2017. ISSN 1465-7392, 1476-4679. doi:10.1038/ncb3466. URL http://www.nature.com/doifinder/10.1038/ncb3466.

[39] Shiqiong Hu, Hanna Grobe, Zhenhuan Guo, Yu-Hsiu Wang, Bryant L. Doss, Meng Pan, Benoit Ladoux, Alexander D. Bershadsky, and Ronen Zaidel-Bar. Recipro-

cal regulation of actomyosin organization and contractility in non-muscle cells by tropomyosins and alpha-actinins. *Molecular Biology of the Cell*, pages mbc.E19–02–0082, June 2019. ISSN 1059-1524, 1939-4586. doi:10.1091/mbc.E19-02-0082. URL https://www.molbiolcell.org/doi/10.1091/mbc.E19-02-0082.

[40] Go Totsukawa, Yoshihiko Yamakita, Shigeko Yamashiro, David J. Hartshorne, Yasuharu Sasaki, and Fumio Matsumura. Distinct Roles of Rock (Rho-Kinase) and Mlck in Spatial Regulation of Mlc Phosphorylation for Assembly of Stress Fibers and Focal Adhesions in 3t3 Fibroblasts. *The Journal of Cell Biology*, 150(4):797–806, August 2000. ISSN 0021-9525, 1540-8140. doi:10.1083/jcb.150.4.797. URL http://www.jcb.org/lookup/doi/10.1083/jcb.150.4.797.

[41] Kazuo Katoh, Yumiko Kano, Mutsuki Amano, Kozo Kaibuchi, and Keigi Fujiwara. Stress fiber organization regulated by MLCK and Rho-kinase in cultured human fibroblasts. *American Journal of Physiology-Cell Physiology*, 280(6):C1669–C1679, June 2001. ISSN 0363-6143, 1522-1563. doi:10.1152/ajpcell.2001.280.6.C1669. URL http://www.physiology.org/doi/10.1152/ajpcell.2001.280.6.C1669.

[42] Yvonne Aratyn-Schaus, Patrick W. Oakes, and Margaret L. Gardel. Dynamic and structural signatures of lamellar actomyosin force generation. *Molecular Biology of the Cell*, 22(8):1330–1339, April 2011. ISSN 1059-1524, 1939-4586. doi:10.1091/mbc.e10-11-0891. URL http://www.molbiolcell.org/doi/10.1091/mbc.e10-11-0891.

[43] Tatyana M. Svitkina. Platinum replica electron microscopy: Imaging the cytoskeleton globally and locally. *The International Journal of Biochemistry & Cell Biology*, 86: 37–41, May 2017. ISSN 13572725. doi:10.1016/j.biocel.2017.03.009. URL https://linkinghub.elsevier.com/retrieve/pii/S1357272517300614.

[44] Alexander B. Verkhovsky, Tatyana M. Svitkina, and Gary G. Borisy. Myosin II filament assemblies in the active lamella of fibroblasts: their morphogenesis and role in the formation of actin filament bundles. *The Journal of Cell Biology*, 131(4):989–1002, November 1995. ISSN 0021-9525, 1540-8140. doi:10.1083/jcb.131.4.989. URL http://www.jcb.org/cgi/doi/10.1083/jcb.131.4.989.

[45] Tatyana M. Svitkina, Alexander B. Verkhovsky, Kyle M. McQuade, and Gary G. Borisy. Analysis of the Actin–Myosin II System in Fish Epidermal Keratocytes: Mechanism of Cell Body Translocation. *Journal of Cell Biology*, 139(2):397–415, October 1997. ISSN 0021-9525, 1540-8140. doi:10.1083/jcb.139.2.397. URL https://rupress.org/jcb/article/139/2/397/47814/Analysis-of-the-ActinMyosin-II-System-in-Fish.

[46] Aidan M. Fenix, Nilay Taneja, Carmen A. Buttler, John Lewis, Schuyler B. Van Engelenburg, Ryoma Ohi, and Dylan T. Burnette. Expansion and concatenation of nonmuscle myosin IIA filaments drive cellular contractile system formation during interphase

and mitosis. *Molecular Biology of the Cell*, 27(9):1465–1478, May 2016. ISSN 1059-1524, 1939-4586. doi:10.1091/mbc.e15-10-0725. URL http://www.molbiolcell.org/doi/10.1091/mbc.e15-10-0725.

[47] Jordan R. Beach, Kyle S. Bruun, Lin Shao, Dong Li, Zac Swider, Kirsten Remmert, Yingfan Zhang, Mary A. Conti, Robert S. Adelstein, Nasser M. Rusan, Eric Betzig, and John A. Hammer. Actin dynamics and competition for myosin monomer govern the sequential amplification of myosin filaments. *Nature Cell Biology*, 19(2):85–93, January 2017. ISSN 1465-7392, 1476-4679. doi:10.1038/ncb3463. URL http://www.nature.com/doifinder/10.1038/ncb3463.

[48] Wen-hung Chou, Mehdi Molaei, Huini Wu, Patrick W. Oakes, Jordan R. Beach, and Margaret L. Gardel. Limiting Pool and Actin Architecture Controls Myosin Cluster Sizes in Adherent Cells. preprint, Biophysics, June 2023. URL http://biorxiv.org/lookup/doi/10.1101/2023.06.07.544121.

[49] Stacey Lee and Sanjay Kumar. Actomyosin stress fiber mechanosensing in 2D and 3D. *F1000Research*, 5:2261, September 2016. ISSN 2046-1402. doi:10.12688/f1000research.8800.1. URL https://f1000research.com/articles/5-2261/v1.

[50] Thomas D. Pollard. Regulation of Actin Filament Assembly by Arp2/3 Complex and Formins. *Annual Review of Biophysics and Biomolecular Structure*, 36(1):451–477, 2007. doi:10.1146/annurev.biophys.35.040405.101936. URL https://doi.org/10.1146/annurev.biophys.35.040405.101936.

[51] Rachel S. Kadzik, Kaitlin E. Homa, and David R. Kovar. F-Actin Cytoskeleton Network Self-Organization Through Competition and Cooperation. *Annual Review of Cell and Developmental Biology*, 36(1):35–60, October 2020. ISSN 1081-0706, 1530-8995. doi:10.1146/annurev-cellbio-032320-094706. URL https://www.annualreviews.org/doi/10.1146/annurev-cellbio-032320-094706.

[52] Melissa A. Quintanilla, John A. Hammer, and Jordan R. Beach. Non-muscle myosin 2 at a glance. *Journal of Cell Science*, 136(5):jcs260890, March 2023. ISSN 0021-9533, 1477-9137. doi:10.1242/jcs.260890. URL https://journals.biologists.com/jcs/article/136/5/jcs260890/297120/Non-muscle-myosin-2-at-a-glance.

[53] J. M. Scholey, K. A. Taylor, and J. Kendrick-Jones. Regulation of non-muscle myosin assembly by calmodulin-dependent light chain kinase. *Nature*, 287:233, September 1980. URL http://dx.doi.org/10.1038/287233a0.

[54] Maria Shutova, Changsong Yang, Jury M. Vasiliev, and Tatyana Svitkina. Functions of Nonmuscle Myosin II in Assembly of the Cellular Contractile System. *PLoS ONE*, 7(7):e40814, July 2012. ISSN 1932-6203. doi:10.1371/journal.pone.0040814. URL https://dx.plos.org/10.1371/journal.pone.0040814.

[55] Maria S. Shutova, Waldo A. Spessott, Claudio G. Giraudo, and Tatyana Svitkina. Endogenous Species of Mammalian Nonmuscle Myosin IIA and IIB Include Activated Monomers and Heteropolymers. *Current Biology*, 24(17):1958–1968, September 2014. ISSN 09609822. doi:10.1016/j.cub.2014.07.070. URL https://linkinghub.elsevier.com/retrieve/pii/S0960982214009671.

[56] Ching-Wei Chang and Sanjay Kumar. Differential Contributions of Nonmuscle Myosin II Isoforms and Functional Domains to Stress Fiber Mechanics. *Scientific Reports*, 5 (1), November 2015. ISSN 2045-2322. doi:10.1038/srep13736. URL http://www.nature.com/articles/srep13736.

[57] Mark T. Breckenridge, Natalya G. Dulyaninova, and Thomas T. Egelhoff. Multiple Regulatory Steps Control Mammalian Nonmuscle Myosin II Assembly in Live Cells. *Molecular Biology of the Cell*, 20(1):338–347, January 2009. ISSN 1059-1524, 1939-4586. doi:10.1091/mbc.e08-04-0372. URL https://www.molbiolcell.org/doi/10.1091/mbc.e08-04-0372.

[58] Kai Weißenbruch, Magdalena Fladung, Justin Grewe, Laurent Baulesch, Ulrich S. Schwarz, and Martin Bastmeyer. Nonmuscle myosin IIA dynamically guides regulatory light chain phosphorylation and assembly of nonmuscle myosin IIB. *European Journal of Cell Biology*, 101(2):151213, April 2022. ISSN 01719335. doi:10.1016/j.ejcb.2022.151213. URL https://linkinghub.elsevier.com/retrieve/pii/S0171933522000164.

[59] John C. Crocker and David G. Grier. Methods of Digital Video Microscopy for Colloidal Studies. *Journal of Colloid and Interface Science*, 179(1):298–310, April 1996. ISSN 00219797. doi:10.1006/jcis.1996.0217. URL https://linkinghub.elsevier.com/retrieve/pii/S0021979796902179.

[60] Melissa A. Quintanilla, Hiral Patel, Huini Wu, Kem A. Sochacki, Matthew Akamatsu, Jeremy D. Rotty, Farida Korobova, James E. Bear, Justin W. Taraska, Patrick W. Oakes, and Jordan R. Beach. Local Monomer Levels and Established Filaments Potentiate Non-Muscle Myosin 2 Assembly. preprint, Cell Biology, April 2023. URL http://biorxiv.org/lookup/doi/10.1101/2023.04.26.538303.

[61] Mihály Kovács, Judit Tóth, Csaba Hetényi, András Málnási-Csizmadia, and James R. Sellers. Mechanism of Blebbistatin Inhibition of Myosin II. *Journal of Biological Chemistry*, 279(34):35557–35563, August 2004. ISSN 00219258. doi:10.1074/jbc.M405319200. URL https://linkinghub.elsevier.com/retrieve/pii/S0021925820731376.

[62] R. K. Mahajan, K. T. Vaughan, J. A. Johns, and J. D. Pardee. Actin filaments mediate Dictyostelium myosin assembly in vitro. *Proceedings of the National Academy of Sciences*, 86(16):6161–6165, August 1989. ISSN 0027-8424, 1091-6490. doi:10.1073/pnas.86.16.6161. URL http://www.pnas.org/cgi/doi/10.1073/pnas.86.16.6161.

[63] Yunfeng Feng, Hai Ngu, Shannon K. Alford, Michael Ward, Frank Yin, and Gregory D. Longmore. α-Actinin1 and 4 tyrosine phosphorylation is critical for stress fiber establishment, maintenance and focal adhesion maturation. *Experimental Cell Research*, 319(8):1124–1135, May 2013. ISSN 00144827. doi:10.1016/j.yexcr.2013.02.009. URL https://linkinghub.elsevier.com/retrieve/pii/S0014482713000657.

[64] Nathan W. Goehring and Anthony A. Hyman. Organelle Growth Control through Limiting Pools of Cytoplasmic Components. *Current Biology*, 22(9):R330–R339, May 2012. ISSN 09609822. doi:10.1016/j.cub.2012.03.046. URL https://linkinghub.elsevier.com/retrieve/pii/S0960982212003338.

[65] Cristian Suarez and David R Kovar. Internetwork competition for monomers governs actin cytoskeleton organization. *Nature Reviews Molecular Cell Biology*, 17:799–799, September 2016. URL http://dx.doi.org/10.1038/nrm.2016.106.

[66] Shixin Yang, Prince Tiwari, Kyoung Hwan Lee, Osamu Sato, Mitsuo Ikebe, Raúl Padrón, and Roger Craig. Cryo-EM structure of the inhibited (10S) form of myosin II. *Nature*, 588(7838):521–525, December 2020. ISSN 0028-0836, 1476-4687. doi:10.1038/s41586-020-3007-0. URL https://www.nature.com/articles/s41586-020-3007-0.

[67] Yaming Jiu, Reena Kumari, Aidan M. Fenix, Niccole Schaible, Xiaonan Liu, Markku Varjosalo, Ramaswamy Krishnan, Dylan T. Burnette, and Pekka Lappalainen. Myosin-18B Promotes the Assembly of Myosin II Stacks for Maturation of Contractile Actomyosin Bundles. *Current Biology*, 29(1):81–92.e5, January 2019. ISSN 09609822. doi:10.1016/j.cub.2018.11.045. URL https://linkinghub.elsevier.com/retrieve/pii/S0960982218315446.

[68] Joyce C. M. Meiring, Nicole S. Bryce, Maria Lastra Cagigas, Aleš Benda, Renee M. Whan, Nicholas Ariotti, Robert G. Parton, Jeffrey H. Stear, Edna C. Hardeman, and Peter W. Gunning. Colocation of Tpm3.1 and myosin IIa heads defines a discrete subdomain in stress fibres. *Journal of Cell Science*, page jcs.228916, January 2019. ISSN 1477-9137, 0021-9533. doi:10.1242/jcs.228916. URL https://journals.biologists.com/jcs/article/doi/10.1242/jcs.228916/266047/Colocation-of-Tpm3-1-and-myosin-IIa-heads-defines.

[69] Claudia Veigel, Justin E. Molloy, Stephan Schmitz, and John Kendrick-Jones. Load-dependent kinetics of force production by smooth muscle myosin measured with optical tweezers. *Nature Cell Biology*, 5(11):980–986, November 2003. ISSN 1465-7392, 1476-4679. doi:10.1038/ncb1060. URL http://www.nature.com/articles/ncb1060.

[70] Todd Thoresen, Martin Lenz, and Margaret L. Gardel. Reconstitution of Contractile Actomyosin Bundles. *Biophysical Journal*, 100(11):2698–2705, 2011. doi:10.1016/j.bpj.2011.04.031. URL http://www.sciencedirect.com/science/article/pii/S0006349511004760.

[71] D. Applegate and J. D. Pardee. Actin-facilitated assembly of smooth muscle myosin induces formation of actomyosin fibrils. *The Journal of Cell Biology*, 117(6):1223–1230, June 1992. ISSN 0021-9525, 1540-8140. doi:10.1083/jcb.117.6.1223. URL http://www.jcb.org/cgi/doi/10.1083/jcb.117.6.1223.

[72] Rohit K. Mahajan and Joel D. Pardee. Assembly Mechanism of Dictyostelium Myosin II: Regulation by K+, Mg2+, and Actin Filaments. *Biochemistry*, 35(48):15504–15514, January 1996. ISSN 0006-2960, 1520-4995. doi:10.1021/bi9618981. URL http://pubs.acs.org/doi/abs/10.1021/bi9618981.

[73] Bipasha Barua, Attila Nagy, James R. Sellers, and Sarah E. Hitchcock-DeGregori. Regulation of Nonmuscle Myosin II by Tropomyosin. *Biochemistry*, 53(24):4015–4024, June 2014. ISSN 0006-2960, 1520-4995. doi:10.1021/bi500162z. URL http://pubs.acs.org/doi/10.1021/bi500162z.

[74] Marina Soares E Silva, Martin Depken, Björn Stuhrmann, Marijn Korsten, Fred C. MacKintosh, and Gijsje H. Koenderink. Active multistage coarsening of actin networks driven by myosin motors. *Proceedings of the National Academy of Sciences*, 108(23):9408–9413, June 2011. ISSN 0027-8424, 1091-6490. doi:10.1073/pnas.1016616108. URL https://pnas.org/doi/full/10.1073/pnas.1016616108.

[75] Darius Vasco Köster, Kabir Husain, Elda Iljazi, Abrar Bhat, Peter Bieling, R. Dyche Mullins, Madan Rao, and Satyajit Mayor. Actomyosin dynamics drive local membrane component organization in an in vitro active composite layer. *Proceedings of the National Academy of Sciences*, 113(12), March 2016. ISSN 0027-8424, 1091-6490. doi:10.1073/pnas.1514030113. URL https://pnas.org/doi/full/10.1073/pnas.1514030113.

[76] Samantha Stam, Simon L. Freedman, Shiladitya Banerjee, Kimberly L. Weirich, Aaron R. Dinner, and Margaret L. Gardel. Filament rigidity and connectivity tune the deformation modes of active biopolymer networks. *Proceedings of the National Academy of Sciences*, 114(47):E10037–E10045, November 2017. ISSN 0027-8424, 1091-6490. doi:10.1073/pnas.1708625114. URL http://www.pnas.org/lookup/doi/10.1073/pnas.1708625114.

[77] Wallace F Marshall. Cell Geometry: How Cells Count and Measure Size. *Annual Review of Biophysics*, 45(1):49–64, July 2016. ISSN 1936-122X, 1936-1238. doi:10.1146/annurev-biophys-062215-010905. URL http://www.annualreviews.org/doi/10.1146/annurev-biophys-062215-010905.

[78] Pan Chen and Daniel L. Levy. Regulation of organelle size and organization during development. *Seminars in Cell & Developmental Biology*, 133:53–64, February 2022. ISSN 10849521. doi:10.1016/j.semcdb.2022.02.002. URL https://linkinghub.elsevier.com/retrieve/pii/S1084952122000301.

[79] Kiandokht Panjtan Amiri, Asa Kalish, and Shankar Mukherji. Robustness and Universality in Organelle Size Control. *Physical Review Letters*, 130(1):018401, January 2023. ISSN 0031-9007, 1079-7114. doi:10.1103/PhysRevLett.130.018401. URL https://link.aps.org/doi/10.1103/PhysRevLett.130.018401.

[80] William B. Ludington, Linda Z. Shi, Qingyuan Zhu, Michael W. Berns, and Wallace F. Marshall. Organelle Size Equalization by a Constitutive Process. *Current Biology*, 22 (22):2173–2179, November 2012. ISSN 09609822. doi:10.1016/j.cub.2012.09.040. URL https://linkinghub.elsevier.com/retrieve/pii/S0960982212011426.

[81] Markus Decker, Steffen Jaensch, Andrei Pozniakovsky, Andrea Zinke, Kevin F. O'Connell, Wolfgang Zachariae, Eugene Myers, and Anthony A. Hyman. Limiting Amounts of Centrosome Material Set Centrosome Size in C. elegans Embryos. *Current Biology*, 21(15):1259–1267, August 2011. ISSN 09609822. doi:10.1016/j.cub.2011.06.002. URL https://linkinghub.elsevier.com/retrieve/pii/S0960982211006476.

[82] Timothy J. Mitchison, Keisuke Ishihara, Phuong Nguyen, and Martin Wühr. Size Scaling of Microtubule Assemblies in Early *Xenopus* Embryos. *Cold Spring Harbor Perspectives in Biology*, 7(10):a019182, October 2015. ISSN 1943-0264. doi:10.1101/cshperspect.a019182. URL http://cshperspectives.cshlp.org/lookup/doi/10.1101/cshperspect.a019182.

[83] Fereshteh R. Najafabadi, Mark Leaver, and Stephan W. Grill. Orchestrating Nonmuscle myosin II filament assembly at the onset of cytokinesis. *Molecular Biology of the Cell*, pages mbc.E21–12–0599, May 2022. ISSN 1059-1524, 1939-4586. doi:10.1091/mbc.E21-12-0599. URL https://www.molbiolcell.org/doi/10.1091/mbc.E21-12-0599.

[84] Alexander Krull, Tim-Oliver Buchholz, and Florian Jug. Noise2Void - Learning Denoising From Single Noisy Images. In *2019 IEEE/CVF Conference on Computer Vision and Pattern Recognition (CVPR)*, pages 2124–2132, Long Beach, CA, USA, June 2019. IEEE. ISBN 978-1-72813-293-8. doi:10.1109/CVPR.2019.00223. URL https://ieeexplore.ieee.org/document/8954066/.

[85] Mehdi Molaei, Steven A. Redford, Wen-hung Chou, Danielle Scheff, Juan J. de Pablo, Patrick W. Oakes, and Margaret L. Gardel. Measuring response functions of active materials from data, March 2023. URL http://arxiv.org/abs/2303.17785. arXiv:2303.17785 [cond-mat, q-bio].

[86] Andrea Cavagna and Irene Giardina. Bird Flocks as Condensed Matter. *Annual Review of Condensed Matter Physics*, 5(1):183–207, March 2014. ISSN 1947-5454, 1947-5462. doi:10.1146/annurev-conmatphys-031113-133834. URL https://www.annualreviews.org/doi/10.1146/annurev-conmatphys-031113-133834.

[87] M. C. Marchetti, J. F. Joanny, S. Ramaswamy, T. B. Liverpool, J. Prost, Madan Rao, and R. Aditi Simha. Hydrodynamics of soft active matter. *Reviews of Modern Physics*, 85(3):1143–1189, July 2013. ISSN 0034-6861, 1539-0756. doi:10.1103/RevModPhys.85.1143. URL https://link.aps.org/doi/10.1103/RevModPhys.85.1143.

[88] Christopher Dombrowski, Luis Cisneros, Sunita Chatkaew, Raymond E. Goldstein, and John O. Kessler. Self-Concentration and Large-Scale Coherence in Bacterial Dynamics. *Physical Review Letters*, 93(9):098103, August 2004. doi:10.1103/PhysRevLett.93.098103. URL https://link.aps.org/doi/10.1103/PhysRevLett.93.098103.

[89] Henricus H. Wensink, Jörn Dunkel, Sebastian Heidenreich, Knut Drescher, Raymond E. Goldstein, Hartmut Löwen, and Julia M. Yeomans. Meso-scale turbulence in living fluids. *Proceedings of the National Academy of Sciences*, 109(36):14308–14313, September 2012. ISSN 0027-8424, 1091-6490. doi:10.1073/pnas.1202032109. URL https://pnas.org/doi/full/10.1073/pnas.1202032109.

[90] Daniel Needleman and Zvonimir Dogic. Active matter at the interface between materials science and cell biology. *Nature Reviews Materials*, 2(9):17048, July 2017. ISSN 2058-8437. doi:10.1038/natrevmats.2017.48. URL https://www.nature.com/articles/natrevmats201748.

[91] Sriram Ramaswamy. The Mechanics and Statistics of Active Matter. *Annual Review of Condensed Matter Physics*, 1(1):323–345, August 2010. ISSN 1947-5454, 1947-5462. doi:10.1146/annurev-conmatphys-070909-104101. URL http://arxiv.org/abs/1004.1933.

[92] Luca Giomi. Geometry and Topology of Turbulence in Active Nematics. *Physical Review X*, 5(3):031003, July 2015. doi:10.1103/PhysRevX.5.031003. URL https://link.aps.org/doi/10.1103/PhysRevX.5.031003.

[93] Tong Gao, Robert Blackwell, Matthew A. Glaser, M. D. Betterton, and Michael J. Shelley. Multiscale Polar Theory of Microtubule and Motor-Protein Assemblies. *Physical Review Letters*, 114(4):048101, January 2015. doi:10.1103/PhysRevLett.114.048101. URL https://link.aps.org/doi/10.1103/PhysRevLett.114.048101.

[94] John C. Crocker, M. T. Valentine, Eric R. Weeks, T. Gisler, P. D. Kaplan, A. G. Yodh, and D. A. Weitz. Two-Point Microrheology of Inhomogeneous Soft Materials. *Physical Review Letters*, 85(4):888–891, July 2000. doi:10.1103/PhysRevLett.85.888. URL https://link.aps.org/doi/10.1103/PhysRevLett.85.888.

[95] Roberto Cerbino and Veronique Trappe. Differential Dynamic Microscopy: Probing Wave Vector Dependent Dynamics with a Microscope. *Physical Review Letters*, 100(18):188102, May 2008. ISSN 0031-9007, 1079-7114. doi:10.1103/PhysRevLett.100.188102. URL https://link.aps.org/doi/10.1103/PhysRevLett.100.188102.

[96] Leo P Kadanoff and Paul C Martin. Hydrodynamic equations and correlation functions. *Annals of Physics*, 24:419–469, October 1963. ISSN 0003-4916. doi:10.1016/0003-4916(63)90078-2. URL https://www.sciencedirect.com/science/article/pii/0003491663900782.

[97] Roseanna N Zia. Active and Passive Microrheology: Theory and Simulation. *Annual Review of Fluid Mechanics*, 50:371–405, 2018.

[98] T. G. Mason and D. A. Weitz. Linear Viscoelasticity of Colloidal Hard Sphere Suspensions near the Glass Transition. *Physical Review Letters*, 75(14):2770–2773, October 1995. ISSN 0031-9007, 1079-7114. doi:10.1103/PhysRevLett.75.2770. URL https://link.aps.org/doi/10.1103/PhysRevLett.75.2770.

[99] F. Gittes, B. Schnurr, P. D. Olmsted, F. C. MacKintosh, and C. F. Schmidt. Microscopic Viscoelasticity: Shear Moduli of Soft Materials Determined from Thermal Fluctuations. *Physical Review Letters*, 79(17):3286–3289, October 1997. ISSN 0031-9007, 1079-7114. doi:10.1103/PhysRevLett.79.3286. URL https://link.aps.org/doi/10.1103/PhysRevLett.79.3286.

[100] Mehdi Molaei, Nicholas G. Chisholm, Jiayi Deng, John C. Crocker, and Kathleen J. Stebe. Interfacial Flow around Brownian Colloids. *Physical Review Letters*, 126(22): 228003, June 2021. doi:10.1103/PhysRevLett.126.228003. URL https://link.aps.org/doi/10.1103/PhysRevLett.126.228003.

[101] Alex J. Levine and F. C. MacKintosh. Dynamics of viscoelastic membranes. *Physical Review E*, 66(6):061606, December 2002. doi:10.1103/PhysRevE.66.061606. URL https://link.aps.org/doi/10.1103/PhysRevE.66.061606.

[102] Nicholas G. Chisholm and Kathleen J. Stebe. Driven and active colloids at fluid interfaces. *Journal of Fluid Mechanics*, 914:A29, May 2021. ISSN 0022-1120, 1469-7645. doi:10.1017/jfm.2020.708. URL https://www.cambridge.org/core/journals/journal-of-fluid-mechanics/article/driven-and-active-colloids-at-fluid-interfaces/33AAD708E7F252F276C3DB090FA036BE.

[103] Berta Martínez-Prat, Ricard Alert, Fanlong Meng, Jordi Ignés-Mullol, Jean-François Joanny, Jaume Casademunt, Ramin Golestanian, and Francesc Sagués. Scaling Regimes of Active Turbulence with External Dissipation. *Physical Review X*, 11(3): 031065, September 2021. ISSN 2160-3308. doi:10.1103/PhysRevX.11.031065. URL https://link.aps.org/doi/10.1103/PhysRevX.11.031065.

[104] Ricard Alert, Jaume Casademunt, and Jean-François Joanny. Active Turbulence. *Annual Review of Condensed Matter Physics*, 13:143–170, March 2022. doi:10.1146/annurev-conmatphys-082321-035957.

[105] Rui Zhang, Nitin Kumar, Jennifer L. Ross, Margaret L. Gardel, and Juan J. de Pablo. Interplay of structure, elasticity, and dynamics in actin-based nematic materials.

Proceedings of the National Academy of Sciences, 115(2):E124–E133, January 2018. doi:10.1073/pnas.1713832115. URL https://www.pnas.org/doi/abs/10.1073/pnas.1713832115.

[106] Nitin Kumar, Rui Zhang, Juan J. de Pablo, and Margaret L. Gardel. Tunable structure and dynamics of active liquid crystals. *Science Advances*, 4(10):eaat7779, October 2018. doi:10.1126/sciadv.aat7779. URL https://www.science.org/doi/full/10.1126/sciadv.aat7779.

[107] Rui Zhang, Steven A. Redford, Paul V. Ruijgrok, Nitin Kumar, Ali Mozaffari, Sasha Zemsky, Aaron R. Dinner, Vincenzo Vitelli, Zev Bryant, Margaret L. Gardel, and Juan J. de Pablo. Spatiotemporal control of liquid crystal structure and dynamics through activity patterning. *Nature Materials*, 20(6):875–882, June 2021. ISSN 1476-4660. doi:10.1038/s41563-020-00901-4. URL https://www.nature.com/articles/s41563-020-00901-4.

[108] Linnea M. Lemma, Stephen J. DeCamp, Zhihong You, Luca Giomi, and Zvonimir Dogic. Statistical properties of autonomous flows in 2D active nematics. *Soft Matter*, 15 (15):3264–3272, April 2019. ISSN 1744-6848. doi:10.1039/C8SM01877D. URL https://pubs.rsc.org/en/content/articlelanding/2019/sm/c8sm01877d.

[109] P. Guillamat, J. Ignés-Mullol, and F. Sagués. Taming active turbulence with patterned soft interfaces. *Nature Communications*, 8(1):564, September 2017. ISSN 2041-1723. doi:10.1038/s41467-017-00617-1. URL https://www.nature.com/articles/s41467-017-00617-1.

[110] G. K. Batchelor. *An Introduction to Fluid Dynamics*. Cambridge Mathematical Library. Cambridge University Press, Cambridge, 2000. ISBN 978-0-521-66396-0. doi:10.1017/CBO9780511800955. URL https://www.cambridge.org/core/books/an-introduction-to-fluid-dynamics/18AA1576B9C579CE25621E80F9266993.

[111] Ricard Alert, Jean-François Joanny, and Jaume Casademunt. Universal scaling of active nematic turbulence. *Nature Physics*, 16(6):682–688, June 2020. ISSN 1745-2473, 1745-2481. doi:10.1038/s41567-020-0854-4. URL http://www.nature.com/articles/s41567-020-0854-4.

[112] Colin-Marius Koch and Michael Wilczek. Role of Advective Inertia in Active Nematic Turbulence. *Physical Review Letters*, 127(26):268005, December 2021. doi:10.1103/PhysRevLett.127.268005. URL https://link.aps.org/doi/10.1103/PhysRevLett.127.268005.

[113] Michael P. Murrell and Margaret L. Gardel. F-actin buckling coordinates contractility and severing in a biomimetic actomyosin cortex. *Proceedings of the National Academy of Sciences*, 109(51):20820–20825, December 2012. doi:10.1073/pnas.1214753109. URL http://www.pnas.org/doi/abs/10.1073/pnas.1214753109.

[114] Daniel S. Seara, Vikrant Yadav, Ian Linsmeier, A. Pasha Tabatabai, Patrick W. Oakes, S. M. Ali Tabei, Shiladitya Banerjee, and Michael P. Murrell. Entropy production rate is maximized in non-contractile actomyosin. *Nature Communications*, 9(1):4948, December 2018. ISSN 2041-1723. doi:10.1038/s41467-018-07413-5. URL http://www.nature.com/articles/s41467-018-07413-5.

[115] Luca Cipelletti, S. Manley, R. C. Ball, and D. A. Weitz. Universal Aging Features in the Restructuring of Fractal Colloidal Gels. *Physical Review Letters*, 84(10):2275–2278, March 2000. doi:10.1103/PhysRevLett.84.2275. URL https://link.aps.org/doi/10.1103/PhysRevLett.84.2275.

[116] Gloria Lee, Gregor Leech, Michael J. Rust, Moumita Das, Ryan J. McGorty, Jennifer L. Ross, and Rae M. Robertson-Anderson. Myosin-driven actin-microtubule networks exhibit self-organized contractile dynamics. *Science Advances*, 7(6):eabe4334, February 2021. ISSN 2375-2548. doi:10.1126/sciadv.abe4334. URL https://www.science.org/doi/10.1126/sciadv.abe4334.

[117] Mathias Reufer, Vincent A. Martinez, Peter Schurtenberger, and Wilson C. K. Poon. Differential Dynamic Microscopy for Anisotropic Colloidal Dynamics. *Langmuir*, 28 (10):4618–4624, March 2012. ISSN 0743-7463, 1520-5827. doi:10.1021/la204904a. URL https://pubs.acs.org/doi/10.1021/la204904a.

[118] Patrick W. Oakes, Elizabeth Wagner, Christoph A. Brand, Dimitri Probst, Marco Linke, Ulrich S. Schwarz, Michael Glotzer, and Margaret L. Gardel. Optogenetic control of RhoA reveals zyxin-mediated elasticity of stress fibres. *Nature Communications*, 8(1):15817, August 2017. ISSN 2041-1723. doi:10.1038/ncomms15817. URL http://www.nature.com/articles/ncomms15817.

[119] Tony D. Schindler, Lu Chen, Paul Lebel, Muneaki Nakamura, and Zev Bryant. Engineering myosins for long-range transport on actin filaments. *Nature Nanotechnology*, 9(1):33–38, January 2014. ISSN 1748-3395. doi:10.1038/nnano.2013.229. URL https://www.nature.com/articles/nnano.2013.229.

[120] Deqing Sun, Stefan Roth, and Michael J. Black. Secrets of optical flow estimation and their principles. In *2010 IEEE Computer Society Conference on Computer Vision and Pattern Recognition*, pages 2432–2439, San Francisco, CA, USA, June 2010. IEEE. ISBN 978-1-4244-6984-0. doi:10.1109/CVPR.2010.5539939. URL http://ieeexplore.ieee.org/document/5539939/.

[121] L. Ji and G. Danuser. Tracking quasi-stationary flow of weak fluorescent signals by adaptive multi-frame correlation. *Journal of Microscopy*, 220(3):150–167, December 2005. ISSN 0022-2720, 1365-2818. doi:10.1111/j.1365-2818.2005.01522.x. URL http://doi.wiley.com/10.1111/j.1365-2818.2005.01522.x.

[122] Gaudenz Danuser and Clare M. Waterman-Storer. Quantitative Fluorescent Speckle Microscopy of Cytoskeleton Dynamics. *Annual Review of Biophysics and Biomolecular*

Structure, 35(1):361–387, 2006. doi:10.1146/annurev.biophys.35.040405.102114. URL https://doi.org/10.1146/annurev.biophys.35.040405.102114.

[123] Joshua C. Sandquist and Anthony R. Means. The C-Terminal Tail Region of Nonmuscle Myosin II Directs Isoform-specific Distribution in Migrating Cells. *Molecular Biology of the Cell*, 19(12):5156–5167, December 2008. ISSN 1059-1524, 1939-4586. doi:10.1091/mbc.e08-05-0533. URL https://www.molbiolcell.org/doi/10.1091/mbc.e08-05-0533.

[124] Miguel Vicente-Manzanares, Margaret A. Koach, Leanna Whitmore, Marcelo L. Lamers, and Alan F. Horwitz. Segregation and activation of myosin IIB creates a rear in migrating cells. *The Journal of Cell Biology*, 183(3):543–554, November 2008. ISSN 0021-9525, 1540-8140. doi:10.1083/jcb.200806030. URL http://www.jcb.org/lookup/doi/10.1083/jcb.200806030.

[125] Anna B. Kobb, Teresa Zulueta-Coarasa, and Rodrigo Fernandez-Gonzalez. Tension regulates myosin dynamics during Drosophila embryonic wound repair. *Journal of Cell Science*, 130(4):689–696, February 2017. ISSN 0021-9533, 1477-9137. doi:10.1242/jcs.196139. URL http://jcs.biologists.org/lookup/doi/10.1242/jcs.196139.

[126] Miklós Képiró, Boglárka H. Várkuti, László Végner, Gergely Vörös, György Hegyi, Máté Varga, and András Málnási-Csizmadia. para-Nitroblebbistatin, the Non-Cytotoxic and Photostable Myosin II Inhibitor. *Angewandte Chemie International Edition*, 53(31):8211–8215, 2014. doi:https://doi.org/10.1002/anie.201403540. URL https://onlinelibrary.wiley.com/doi/abs/10.1002/anie.201403540. _eprint: https://onlinelibrary.wiley.com/doi/pdf/10.1002/anie.201403540.

[127] Brian L. Sprague, Robert L. Pego, Diana A. Stavreva, and James G. McNally. Analysis of Binding Reactions by Fluorescence Recovery after Photobleaching. *Biophysical Journal*, 86(6):3473–3495, June 2004. ISSN 00063495. doi:10.1529/biophysj.103.026765. URL https://linkinghub.elsevier.com/retrieve/pii/S0006349504743921.

[128] J. Chloë Bulinski, David J. Odde, Bonnie J. Howell, Ted D. Salmon, and Clare M. Waterman-Storer. In vivo dynamics of E-MAP115 (ensconsin). *Journal of Cell Science*, 114(21):3885–3897, July 2001.

[129] Sven K Vogel, Zdenek Petrasek, Fabian Heinemann, and Petra Schwille. Myosin motors fragment and compact membrane-bound actin filaments. *eLife*, 2:e00116, January 2013. ISSN 2050-084X. doi:10.7554/eLife.00116. URL https://elifesciences.org/articles/00116.

[130] S. Nagy, B. L. Ricca, M. F. Norstrom, D. S. Courson, C. M. Brawley, P. A. Smithback, and R. S. Rock. A myosin motor that selects bundled actin for motility. *Proceedings of the National Academy of Sciences*, 105(28):9616–9620, July 2008. ISSN 0027-8424, 1091-6490. doi:10.1073/pnas.0802592105. URL http://www.pnas.org/cgi/doi/10.1073/pnas.0802592105.

[131] Anne-Cécile Reymann, Rajaa Boujemaa-Paterski, Jean-Louis Martiel, Christophe Guérin, Wenxiang Cao, Harvey F Chin, Enrique M De La Cruz, Manuel Théry, and Laurent Blanchoin. Actin Network Architecture Can Determine Myosin Motor Activity. *Science*, 336(6086):1310 LP–1314, June 2012. URL http://science.sciencemag.org/content/336/6086/1310.abstract.

[132] Jun Peng, Bradley J. Wallar, Akiko Flanders, Pamela J. Swiatek, and Arthur S. Alberts. Disruption of the Diaphanous-Related Formin Drf1 Gene Encoding mDia1 Reveals a Role for Drf3 as an Effector for Cdc42. *Current Biology*, 13(7):534–545, April 2003. ISSN 09609822. doi:10.1016/S0960-9822(03)00170-2. URL https://linkinghub.elsevier.com/retrieve/pii/S0960982203001702.

[133] Sari Tojkander, Gergana Gateva, Galina Schevzov, Pirta Hotulainen, Perttu Naumanen, Claire Martin, Peter W. Gunning, and Pekka Lappalainen. A Molecular Pathway for Myosin II Recruitment to Stress Fibers. *Current Biology*, 21(7):539–550, April 2011. ISSN 09609822. doi:10.1016/j.cub.2011.03.007. URL http://linkinghub.elsevier.com/retrieve/pii/S096098221100279X.

[134] Sadanori Watanabe, Yoshikazu Ando, Shingo Yasuda, Hiroshi Hosoya, Naoki Watanabe, Toshimasa Ishizaki, and Shuh Narumiya. mDia2 Induces the Actin Scaffold for the Contractile Ring and Stabilizes Its Position during Cytokinesis in NIH 3T3 Cells. *Molecular Biology of the Cell*, 19(5):2328–2338, May 2008. ISSN 1059-1524, 1939-4586. doi:10.1091/mbc.e07-10-1086. URL http://www.molbiolcell.org/doi/10.1091/mbc.e07-10-1086.

[135] Judith E. Gasteier, Ricardo Madrid, Ellen Krautkrämer, Sebastian Schröder, Walter Muranyi, Serge Benichou, and Oliver T. Fackler. Activation of the Rac-binding Partner FHOD1 Induces Actin Stress Fibers via a ROCK-dependent Mechanism. *Journal of Biological Chemistry*, 278(40):38902–38912, October 2003. ISSN 0021-9258, 1083-351X. doi:10.1074/jbc.M306229200. URL http://www.jbc.org/lookup/doi/10.1074/jbc.M306229200.

[136] Timothy J. Gauvin, Lorna E. Young, and Henry N. Higgs. The formin FMNL3 assembles plasma membrane protrusions that participate in cell–cell adhesion. *Molecular Biology of the Cell*, 26(3):467–477, February 2015. ISSN 1059-1524, 1939-4586. doi:10.1091/mbc.E14-07-1247. URL https://www.molbiolcell.org/doi/10.1091/mbc.E14-07-1247.

[137] Yukako Nishimura, Shidong Shi, Qingsen Li, Alexander D. Bershadsky, and Virgile Viasnoff. Crosstalk between myosin II and formin functions in the regulation of force generation and actomyosin dynamics in stress fibers. *Cells & Development*, 168:203736, December 2021. ISSN 26672901. doi:10.1016/j.cdev.2021.203736. URL https://linkinghub.elsevier.com/retrieve/pii/S266729012100070X.

[138] Yukako Nishimura, Shidong Shi, Fang Zhang, Rong Liu, Yasuharu Takagi, Alexander D. Bershadsky, Virgile Viasnoff, and James R. Sellers. The formin inhibitor

SMIFH2 inhibits members of the myosin superfamily. *Journal of Cell Science*, 134 (8):jcs253708, April 2021. ISSN 0021-9533, 1477-9137. doi:10.1242/jcs.253708. URL https://journals.biologists.com/jcs/article/134/8/jcs253708/237818/The-formin-inhibitor-SMIFH2-inhibits-members-of.

[139] James L. Daniel and James R. Sellers. Purification and characterization of platelet myosin. In *Methods in Enzymology*, volume 215, pages 78–88. Academic Press, January 1992. ISBN 0076-6879. doi:10.1016/0076-6879(92)15054-G. URL http://www.sciencedirect.com/science/article/pii/007668799215054G.

[140] Xiong Liu, Neil Billington, Shi Shu, Shu-Hua Yu, Grzegorz Piszczek, James R. Sellers, and Edward D. Korn. Effect of ATP and regulatory light-chain phosphorylation on the polymerization of mammalian nonmuscle myosin II. *Proceedings of the National Academy of Sciences*, 114(32):E6516–E6525, August 2017. ISSN 0027-8424, 1091-6490. doi:10.1073/pnas.1702375114. URL http://www.pnas.org/lookup/doi/10.1073/pnas.1702375114.

[141] Xiong Liu, Shi Shu, and Edward D. Korn. Polymerization pathway of mammalian nonmuscle myosin 2s. *Proceedings of the National Academy of Sciences*, 115(30):E7101–E7108, July 2018. ISSN 0027-8424, 1091-6490. doi:10.1073/pnas.1808800115. URL http://www.pnas.org/lookup/doi/10.1073/pnas.1808800115.

[142] Jaakko I Lehtimäki, Eeva Kaisa Rajakylä, Sari Tojkander, and Pekka Lappalainen. Generation of stress fibers through myosin-driven reorganization of the actin cortex. *eLife*, 10:e60710, January 2021. ISSN 2050-084X. doi:10.7554/eLife.60710. URL https://elifesciences.org/articles/60710.

[143] Xiaoyu Sun, Donovan Y.Z. Phua, Lucas Axiotakis, Mark A. Smith, Elizabeth Blankman, Rui Gong, Robert C. Cail, Santiago Espinosa de los Reyes, Mary C. Beckerle, Clare M. Waterman, and Gregory M. Alushin. Mechanosensing through Direct Binding of Tensed F-Actin by LIM Domains. *Developmental Cell*, 55(4): 468–482.e7, November 2020. ISSN 15345807. doi:10.1016/j.devcel.2020.09.022. URL https://linkinghub.elsevier.com/retrieve/pii/S1534580720307541.

[144] Jonathan D. Winkelman, Caitlin A. Anderson, Cristian Suarez, David R. Kovar, and Margaret L. Gardel. Evolutionarily diverse LIM domain-containing proteins bind stressed actin filaments through a conserved mechanism. *Proceedings of the National Academy of Sciences*, 117(41):25532–25542, October 2020. ISSN 0027-8424, 1091-6490. doi:10.1073/pnas.2004656117. URL http://www.pnas.org/lookup/doi/10.1073/pnas.2004656117.

[145] Mark A Smith, Elizabeth Blankman, Margaret L Gardel, Laura Luettjohann, Clare M Waterman, and Mary C Beckerle. A Zyxin-Mediated Mechanism for Actin Stress Fiber Maintenance and Repair. *Developmental Cell*, 19(3):365–376, February 2010. doi:10.1016/j.devcel.2010.08.008. URL http://dx.doi.org/10.1016/j.devcel.2010.08.008.

[146] M A Smith, L M Hoffman, and M C Beckerle. LIM proteins in actin cytoskeleton mechanoresponse. *Trends in Cell Biology*, 24(10):575–583, February 2014. doi:10.1016/j.tcb.2014.04.009. URL http://dx.doi.org/10.1016/j.tcb.2014.04.009.

[147] Elena Kassianidou, Jasmine H. Hughes, and Sanjay Kumar. Activation of ROCK and MLCK tunes regional stress fiber formation and mechanics via preferential myosin light chain phosphorylation. *Molecular Biology of the Cell*, 28(26):3832–3843, December 2017. ISSN 1059-1524, 1939-4586. doi:10.1091/mbc.e17-06-0401. URL http://www.molbiolcell.org/doi/10.1091/mbc.e17-06-0401.

[148] Elena Kassianidou, Christoph A. Brand, Ulrich S. Schwarz, and Sanjay Kumar. Geometry and network connectivity govern the mechanics of stress fibers. *Proceedings of the National Academy of Sciences*, 114(10):2622–2627, March 2017. ISSN 0027-8424, 1091-6490. doi:10.1073/pnas.1606649114. URL http://www.pnas.org/lookup/doi/10.1073/pnas.1606649114.

[149] Patrick M. McCall, Frederick C. MacKintosh, David R. Kovar, and Margaret L. Gardel. Cofilin drives rapid turnover and fluidization of entangled F-actin. *Proceedings of the National Academy of Sciences*, 116(26):12629–12637, June 2019. ISSN 0027-8424, 1091-6490. doi:10.1073/pnas.1818808116. URL http://www.pnas.org/lookup/doi/10.1073/pnas.1818808116.

[150] Stacey Lee, Elena Kassianidou, and Sanjay Kumar. Actomyosin stress fiber subtypes have unique viscoelastic properties and roles in tension generation. *Molecular Biology of the Cell*, 29(16):1992–2004, August 2018. ISSN 1059-1524, 1939-4586. doi:10.1091/mbc.E18-02-0106. URL https://www.molbiolcell.org/doi/10.1091/mbc.E18-02-0106.

[151] Jonathan Colen, Ming Han, Rui Zhang, Steven A. Redford, Linnea M. Lemma, Link Morgan, Paul V. Ruijgrok, Raymond Adkins, Zev Bryant, Zvonimir Dogic, Margaret L. Gardel, Juan J. de Pablo, and Vincenzo Vitelli. Machine learning active-nematic hydrodynamics. *Proceedings of the National Academy of Sciences*, 118(10):e2016708118, March 2021. ISSN 0027-8424, 1091-6490. doi:10.1073/pnas.2016708118. URL https://pnas.org/doi/full/10.1073/pnas.2016708118.

[152] A. Ponti, M. Machacek, S. L. Gupton, C. M. Waterman-Storer, and G. Danuser. Two Distinct Actin Networks Drive the Protrusion of Migrating Cells. *Science*, 305(5691):1782–1786, September 2004. ISSN 0036-8075, 1095-9203. doi:10.1126/science.1100533. URL https://www.science.org/doi/10.1126/science.1100533.

[153] C H Lin, E M Espreafico, M S Mooseker, and P Forscher. Myosin Drives Retrograde F-Actin Flow in Neuronal Growth Cones. *Neuron*, 16:769–782, April 1996.

[154] Margaret L. Gardel, Benedikt Sabass, Lin Ji, Gaudenz Danuser, Ulrich S. Schwarz, and Clare M. Waterman. Traction stress in focal adhesions correlates biphasically with

actin retrograde flow speed. *Journal of Cell Biology*, 183(6):999–1005, December 2008. ISSN 1540-8140, 0021-9525. doi:10.1083/jcb.200810060. URL https://rupress.org/jcb/article/183/6/999/35390/Traction-stress-in-focal-adhesions-correlates.

[155] Ewan J. Hemingway, Prashant Mishra, M. Cristina Marchetti, and Suzanne M. Fielding. Correlation lengths in hydrodynamic models of active nematics. *Soft Matter*, 12 (38):7943–7952, 2016. doi:10.1039/C6SM00812G. URL https://pubs.rsc.org/en/content/articlelanding/2016/sm/c6sm00812g.

[156] Dieter Forster. *Hydrodynamic Fluctuations, Broken Symmetry, and Correlation Functions*. CRC Press, 1 edition, March 2018. ISBN 978-0-429-49368-3. doi:10.1201/9780429493683. URL https://www.taylorfrancis.com/books/9780429962233.

[157] Tamás Vicsek and Anna Zafeiris. Collective motion. *Physics Reports*, 517(3):71–140, August 2012. ISSN 0370-1573. doi:10.1016/j.physrep.2012.03.004. URL https://www.sciencedirect.com/science/article/pii/S0370157312000968.

[158] Sumesh P. Thampi, Ramin Golestanian, and Julia M. Yeomans. Velocity Correlations in an Active Nematic. *Physical Review Letters*, 111(11):118101, September 2013. doi:10.1103/PhysRevLett.111.118101. URL https://link.aps.org/doi/10.1103/PhysRevLett.111.118101.

[159] Sumesh P. Thampi, Ramin Golestanian, and Julia M. Yeomans. Vorticity, defects and correlations in active turbulence. *Philosophical Transactions of the Royal Society A: Mathematical, Physical and Engineering Sciences*, 372(2029):20130366, November 2014. doi:10.1098/rsta.2013.0366. URL https://royalsocietypublishing.org/doi/full/10.1098/rsta.2013.0366.

[160] Sumesh P. Thampi, Ramin Golestanian, and Julia M. Yeomans. Active nematic materials with substrate friction. *Physical Review E*, 90(6):062307, December 2014. doi:10.1103/PhysRevE.90.062307. URL https://link.aps.org/doi/10.1103/PhysRevE.90.062307.

[161] Berta Martínez-Prat, Jordi Ignés-Mullol, Jaume Casademunt, and Francesc Sagués. Selection mechanism at the onset of active turbulence. *Nature Physics*, 15(4):362–366, April 2019. ISSN 1745-2481. doi:10.1038/s41567-018-0411-6. URL https://www.nature.com/articles/s41567-018-0411-6.

[162] D. J. G. Pearce, J. Nambisan, P. W. Ellis, A. Fernandez-Nieves, and L. Giomi. Orientational Correlations in Active and Passive Nematic Defects. *Physical Review Letters*, 127(19):197801, November 2021. doi:10.1103/PhysRevLett.127.197801. URL https://link.aps.org/doi/10.1103/PhysRevLett.127.197801.

[163] Debarghya Banerjee, Anton Souslov, and Vincenzo Vitelli. Hydrodynamic correlation functions of chiral active fluids. *Physical Review Fluids*, 7(4):043301, April 2022.

doi:10.1103/PhysRevFluids.7.043301. URL https://link.aps.org/doi/10.1103/PhysRevFluids.7.043301.

[164] Nitin Kumar, Rui Zhang, Steven A. Redford, Juan J. de Pablo, and Margaret L. Gardel. Catapulting of topological defects through elasticity bands in active nematics. *Soft Matter*, 18(28):5271–5281, 2022. doi:10.1039/D2SM00414C. URL https://pubs.rsc.org/en/content/articlelanding/2022/sm/d2sm00414c.

[165] Romain Mueller, Julia M. Yeomans, and Amin Doostmohammadi. Emergence of Active Nematic Behavior in Monolayers of Isotropic Cells. *Physical Review Letters*, 122(4):048004, February 2019. ISSN 0031-9007, 1079-7114. doi:10.1103/PhysRevLett.122.048004. URL https://link.aps.org/doi/10.1103/PhysRevLett.122.048004.

[166] Tim Sanchez, Daniel T. N. Chen, Stephen J. DeCamp, Michael Heymann, and Zvonimir Dogic. Spontaneous motion in hierarchically assembled active matter. *Nature*, 491 (7424):431–434, November 2012. ISSN 0028-0836, 1476-4687. doi:10.1038/nature11591. URL http://www.nature.com/articles/nature11591.

[167] P. G. de Gennes and J. Prost. *The Physics of Liquid Crystals*. Clarendon Press, 1993. ISBN 978-0-19-851785-6.

[168] Amin Doostmohammadi, Jordi Ignés-Mullol, Julia M. Yeomans, and Francesc Sagués. Active nematics. *Nature Communications*, 9(1):3246, August 2018. ISSN 2041-1723. doi:10.1038/s41467-018-05666-8. URL http://www.nature.com/articles/s41467-018-05666-8.

[169] M. L. Gardel, J. H. Shin, F. C. MacKintosh, L. Mahadevan, P. Matsudaira, and D. A. Weitz. Elastic Behavior of Cross-Linked and Bundled Actin Networks. *Science*, 304 (5675):1301–1305, May 2004. doi:10.1126/science.1095087. URL https://www.science.org/doi/full/10.1126/science.1095087.

[170] Martin Lenz, Todd Thoresen, Margaret L. Gardel, and Aaron R. Dinner. Contractile Units in Disordered Actomyosin Bundles Arise from F-Actin Buckling. *Physical Review Letters*, 108(23):238107, June 2012. ISSN 0031-9007, 1079-7114. doi:10.1103/PhysRevLett.108.238107. URL https://link.aps.org/doi/10.1103/PhysRevLett.108.238107.

[171] Deqing Sun, Stefan Roth, and Michael J. Black. A Quantitative Analysis of Current Practices in Optical Flow Estimation and the Principles Behind Them. *International Journal of Computer Vision*, 106(2):115–137, January 2014. ISSN 1573-1405. doi:10.1007/s11263-013-0644-x. URL https://doi.org/10.1007/s11263-013-0644-x.

[172] Shiladitya Banerjee, Margaret L. Gardel, and Ulrich S. Schwarz. The Actin Cytoskeleton as an Active Adaptive Material. *Annual review of condensed matter physics*, 11

(1):421–439, March 2020. ISSN 1947-5454. doi:10.1146/annurev-conmatphys-031218-013231. URL https://www.ncbi.nlm.nih.gov/pmc/articles/PMC7748259/.

[173] Luca Giomi, Mark J Bowick, Prashant Mishra, Rastko Sknepnek, and M Cristina Marchetti. Defect dynamics in active nematics. *Philosophical Transactions of the Royal Society A: Mathematical, Physical and Engineering Sciences*, 372(2029): 20130365, November 2014. ISSN 1364-503X, 1471-2962. doi:10.1098/rsta.2013.0365. URL https://royalsocietypublishing.org/doi/10.1098/rsta.2013.0365.